ROYAL SOCIETY OF CHEMISTRY

REVIEW

Check for updates

Advances in designs and mechanisms of semiconducting metal oxide nanostructures for high-precision gas sensors operated at room temperature

Zhijie Li, [a] Hao Li, [a] Zhonglin Wu, [a] Mingkui Wang, [b] Jingting Luo, [c] Hamdi Torun, [d] PingAn Hu, [e] Chang Yang, [f] Marius Grundmann, [f] Xiaoteng Liu[d] and YongQing Fu *[da]

High-precision gas sensors operated at room temperature are attractive for various real-time gas monitoring applications, with advantages including low energy consumption, cost effectiveness and device miniaturization/flexibility. Studies on sensing materials, which play a key role in good gas sensing performance, are currently focused extensively on semiconducting metal oxide nanostructures (SMONs) used in the conventional resistance type gas sensors. This topical review highlights the designs and mechanisms of different SMONs with various patterns (*e.g.* nanoparticles, nanowires, nanosheets, nanorods, nanotubes, nanofilms, *etc.*) for gas sensors to detect various hazardous gases at room temperature. The key topics include (1) single phase SMONs including both n-type and p-type ones; (2) noble metal nanoparticle and metal ion modified SMONs; (3) composite oxides of SMONs; (4) composites of SMONs with carbon nanomaterials. Enhancement of the sensing performance of SMONs at room temperature can also be realized using a photo-activation effect such as ultraviolet light. SMON based mechanically flexible and wearable room temperature gas sensors are also discussed. Various mechanisms have been discussed for the enhanced sensing performance, which include redox reactions, heterojunction generation, formation of metal sulfides and the spillover effect. Finally, major challenges and prospects for the SMON based room temperature gas sensors are highlighted.

1. Introduction

Various types of hazardous gases, such as H_2S, CO, NO_2, NH_3, H_2, CH_4, toluene, acetone, ethanol, methanol and benzene, are routinely and daily released from industrial and agriculture processes, or emitted as vehicle exhaust emissions. Some of them, such as H_2 and CH_4, are explosive when exposed to air, whereas the others, such as NO_2 and toluene, are harmful for human health and the environment, when their concentrations are above a critical threshold, sometimes as low as at parts-per-million

(ppm) levels. Therefore, development of high-precision gas sensors with high sensitivity, fast response, good selectivity, low limit of detection (LOD), as well as *in situ* and real-time monitoring capabilities is paramount.[1,2] For this purpose, various types of gas sensors have been developed, mainly including resistive,[3-5] optical,[6-9] ultrasonic and acoustic wave,[10-12] thermoelectric[13,14] and electrochemical[15-17] ones.

Among these gas sensors, the resistive gas sensor is one of the most popular types, and is simple and easy to fabricate using cost effective processes. The transduction mechanism of resistive gas sensors is based on the change in resistance of a sensing layer upon adsorption and reaction with the target gas molecules. The sensing layer usually determines the sensitivity and selectivity. Therefore, the sensing materials and the structures of the sensing layer are highly critical to their sensing performance. The sensing materials used in these resistive gas sensors are mainly semiconducting metal oxide nanostructures (SMONs),[18-21] carbon materials[22-26] and organic semiconductors.[27-30] Compared to the carbon materials and organic semiconductors, SMONs generally have higher sensitivity, faster response/recovery speed, better reversibility and stability, and they are cost-effective with simple

[a] *School of Physics, University of Electronic Science and Technology of China, Chengdu, 610054, P. R. China*

[b] *Wuhan National Laboratory for Optoelectronics, Huazhong University of Science and Technology, Luoyu Road 1037, Wuhan 430074, P. R. China*

[c] *Shenzhen Key Laboratory of Advanced Thin Films and Applications, College of Physics and Energy, Shenzhen University, 518060 Shenzhen, China*

[d] *Faculty of Engineering and Environment, Northumbria University, Newcastle Upon Tyne, NE1 8ST, UK. E-mail: richard.fu@northumbria.ac.uk*

[e] *Key Laboratory of Micro-systems and Micro-structures Manufacturing of Ministry of Education, Harbin Institute of Technology, Harbin 150080, P. R. China*

[f] *Felix-Bloch-Institut für Festkörperphysik, Universität Leipzig, Linnéstr. 5, 04103 Leipzig, Germany*

This journal is © The Royal Society of Chemistry 2019

fabrication processes.[18–20] SMONs have large specific surface areas with numerous active sites, which facilitate fast adsorption and reaction of target gases, thus enhancing their sensing performance. They have been used to detect various hazardous gases for different applications as shown in Fig. 1. These SMON sensing materials mainly include ZnO,[31,32] CuO,[33–36] SnO$_2$,[37–39] TiO$_2$,[40,41] Fe$_2$O$_3$,[42,43] In$_2$O$_3$,[44–47] Co$_3$O$_4$[48–50] and WO$_3$.[18,51] For further improvement of sensing performance, they have been modified using noble metals,[52–55] metal ions,[56–60] and carbon materials.[61–64] Composites of multi-phase SMONs[65–67] have also been frequently reported.

SMON-based sensors are usually heated to a higher temperature (between 100 °C to 400 °C) for performance enhancement at the expense of structural complications.[42–47] Operation at elevated temperature levels significantly increases the energy consumption, overall device size and cost of gas sensors. Heating up to a high temperature could lead to changes in the microstructure of the sensing nanomaterials, which can result in degradation of sensing performance. In addition, high-temperature sensing has its practical limitations. Particularly, heating is very dangerous for the detection of flammable and explosive gases, with a risk of explosion. Therefore, sensors operated at room temperature (RT) are desirable for minimizing energy consumption and cost, increasing security and stability, realizing device miniaturization and suitability for handheld operations.[68,69] For these reasons, RT gas sensors based on the SMONs have received extensive attention in recent years. Different configurations of SMONs employing nanostructures have been demonstrated with desirable performance enhancements,[70] regarding sensitivity, response/recovery time, selectivity, reversibility, reproducibility and long-term stability. Various SMONs have been designed and synthesized, such as nanorods,[71–75] nanoparticles,[76–81] nanowires,[82–89] nanospheres,[90] nanosheets,[91–94] nanotubes,[95–98] and mesoporous nanostructures.[99–103]

Fig. 1 Schematic diagram of resistance-type gas sensors based on semiconducting metal oxide nanostructures for detection of various hazardous gases.

The literature on SMON-based RT gas sensing is rich and the application area is very critical. New devices have been regularly introduced. Although the merits of the SMON based RT gas sensors have already been demonstrated, currently there are still some key challenges:

(1) The sensing performance of these SMON based gas sensors is limited, when operated at RT. For example, many of these sensors exhibit insufficient sensitivities.[104–108]

(2) The response/recovery times of many RT gas sensors, which are crucial for rapid detection of target dangerous gases to timely trigger an alarm, are generally quite long, sometimes, up to tens of minutes.[109–111]

(3) Poor reversibility has been reported for some of these sensors operated at RT.[101]

Zhijie Li

Dr Zhijie Li is an associate professor at the University of Electronic Science and Technology of China. He obtained his PhD degree in physical chemistry from the Institute of Coal Chemistry, Chinese Academy of Sciences in 2005. His research work has been focused on nanomaterials, gas sensors, photocatalysis, supercapacitors and surface acoustic wave devices. He has published over 70 SCI-indexed refereed journal papers and his H-index is 20.

YongQing Fu

Professor Richard YongQing Fu has extensive experience in smart thin film/materials, biomedical microdevices, lab-on-chip, micromechanics, MEMS, nanotechnology, sensors and microfluidics. His research work has been focused on shape memory films, piezoelectric thin films, nanostructured composites, and smart materials and smart microsystems for applications in MEMS, sensing and energy applications. Up to 2018, he has published over 350 science citation index (SCI) journal papers (with an SCI H-index of 43), two books and over 120 conference papers. He is an associate editor/editorial board member for seven international journals, has co-organized 12 international conferences worldwide and co-edited six special issues for journals.

(4) Poor selectivity is another key limitation for the RT gas sensors. Selectivity of many SMON based RT gas sensors needs to be improved to avoid interference and cross-talks.[112]

The aim of this topical review is to critically evaluate the design and structure of SMON-based gas sensors that may help guide the design of new devices. The performance of these SMON based gas sensors operated at RT could be improved significantly by modifying the SMONs using noble metal nanoparticles,[113–116] metal ions,[117–119] composites of multiple SMONs[120–123] and carbon nanomaterials.[124–126] In addition, not only the quantity of chemisorbed oxygen species,[127] defects[128] and element compositions[129,130] on the surface of SMONs, but also the structural properties, *i.e.*, porosity,[131] heterojunction properties[132–134] and conductivity[135,136] can affect the RT gas sensing performance. Therefore, understanding the relationship between the sensing properties and structures of SMONs is crucial to design gas sensing materials with good sensing performance operated at RT.

Several review papers have been published on gas sensors based on different SMON sensing materials, including n-type oxide semiconductors such as ZnO,[20,137] Fe_2O_3,[138] SnO_2,[39,139,140] p-type oxide semiconductors,[141] metal oxide-based heterojunctions,[142] noble metal/metal oxide semiconductors[143,144] and graphene–metal oxide nanohybrids.[145] However, these review papers discuss the sensing properties of the sensors which are generally operated at higher working temperatures above RT.[146–150] Others about the RT gas sensors are focused more on certain types of SMONs based on RT sensors, such as nanostructured ZnO based RT gas sensors.[151] However, there is no comprehensive review which is focused on the recent progress in various SMONs for high-precision gas sensors operated at RT. Therefore, this review will comprehensively summarize and discuss the recent developments of the RT gas sensors based on single phase SMONs, noble metal and metal ion modified SMONs, composites of SMONs with other metal oxides, and composites of SMONs with carbon nanomaterials, as shown in Fig. 2. In addition, we will discuss the effect of UV light stimulation on enhancing the performance of SMON based RT gas sensors, and mechanically flexible RT gas sensors based on SMONs.

2. Room temperature gas sensors based on single phase semiconducting metal oxide nanostructures

2.1 N-type semiconducting metal oxide nanostructures and gas sensors

N-type SMONs are the most reported sensing materials for RT resistive gas sensors, and they include ZnO,[152–156] SnO_2,[157–160] In_2O_3,[161] WO_3,[162] TiO_2,[163–166] Fe_2O_3,[167–169] MoO_3,[170] VO_2[171] and CeO_2.[172] Various forms of nanostructures including nanoparticles, nanorods, nanowires, nanoflowers, nanosheets, nanofilms, nanotubes, porous structures and hierarchical nanostructures have been employed to detect various types of gases including H_2S,[99,101] NO_2,[157] H_2,[173] NH_3,[174] acetone,[175] alcohol,[106] HCHO,[176]
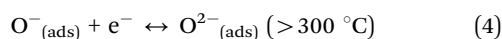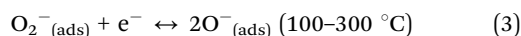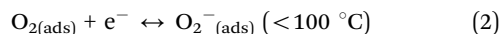

Fig. 2 Schematic diagram of various semiconducting metal oxide nanostructures used for RT gas sensors presented in this review.

liquefied petroleum gas (LPG), *etc.* Table 1 summarizes some of the reported RT sensors using the n-type SMONs.

2.1.1 Gas sensing mechanisms. The gas sensing mechanism of semiconductor oxide based resistive sensors is mostly based on the changes of resistance after they are exposed to the target gases due to the chemical interactions between target gas molecules and the adsorbed oxygen ions on the surface of SMONs.[153,154] Conductance of n-type SMONs relies on electron carriers. When the n-type SMONs are surrounded by air, the oxygen molecules are absorbed on their surfaces. The absorbed oxygen molecules extract electrons from the conduction band of the surface layer, which results in the formation of negatively charged chemisorbed oxygen ions including O_2^-, O^- and O^{2-} at different operating temperatures. Due to the decrease in the electron density, an electron depletion layer is formed on the surface of SMONs and a potential barrier is generated.[42,43] Therefore, the conductivity of the SMONs decreases, thus resulting in an increased resistance.

The operation temperature of gas sensors determines the types of chemisorbed oxygen ions. For example, they are mainly O_2^- when the temperature is below 100 °C. When the working temperature is increased between 100 °C and 300 °C, the O_2^- ions will capture electrons and then transform into O^- ions. The O^- can be converted into O^{2-} ions at a higher working temperature above 300 °C. The formation process of oxygen ions can be summarized using the following equations:[42,43]

$$O_{2(gas)} \leftrightarrow O_{2(ads)} \tag{1}$$

$$O_{2(ads)} + e^- \leftrightarrow O_2^-{}_{(ads)} \, (<100 \,^\circ C) \tag{2}$$

$$O_2^-{}_{(ads)} + e^- \leftrightarrow 2O^-{}_{(ads)} \, (100–300 \,^\circ C) \tag{3}$$

$$O^-{}_{(ads)} + e^- \leftrightarrow O^{2-}{}_{(ads)} \, (>300 \,^\circ C) \tag{4}$$

Therefore, at RT, the oxygen ions on the surface of n-type SMONs are mainly O_2^- ions. When the sensor is exposed to

Table 1 Summary of room temperature sensing properties of n-type semiconducting metal oxide nanostructures

Material	Structure	Synthesis method	Target gas	C (ppm)	Response	t_{res}/t_{rec}	LOD	Ref.
ZnO	Combs	CVD	H_2S	4	6	22/540 s	100 ppb	152
ZnO	Dendritic	Vapor-phase transport	H_2S	500	26.4	20/50 s	10 ppm	153
ZnO	Nanorods	Hydrothermal	H_2S	1	$\sim$35	$\sim$20/— min	0.05 ppm	109
ZnO	Quantum dots	Colloidal process	H_2S	50	113.5	16/820 s	10 ppm	177
ZnO	Nanorods	Vapor-phase transport	H_2S	1	296	320/3592 s	0.5 ppm	71
ZnO	Thin films	Thermal evaporation	Ethanol	100	3	—	—	178
ZnO	Tetrapod network	Thermal oxidation	Ethanol	1000	$\sim$4.5	300/— s	$\sim$10 ppm	179
ZnO	Nanorods	Laser ablation	Ethanol	250	14	—	$\sim$1 ppm	154
ZnO	Nanorods	Electrospinning	Ethanol	100	23	26/43 s	$\sim$1 ppm	180
ZnO	Nanowires	Electrospinning	Ethanol	100	78	9/12 s	$\sim$1 ppm	82
ZnO	Nanorods	Wet chemical route	NH_3	200	24.1	239/398 s	$\sim$50 ppm	181
ZnO	Nanowires	AAO template	NH_3	50	68^b	28/29 s	$\sim$10 ppm	83
ZnO	Thin films	Spray pyrolysis	NH_3	25	233	20/25 s	5 ppm	182
ZnO	Thin films	Magnetron sputtering	NH_3	100	304	92/113 s	5 ppm	112
ZnO	Nanowalls	Solution	NO_2	50	$\sim$6.2	23/11 s	$\sim$5 ppm	91
ZnO	Nanowires	Drop-cast	NO_2	20	32	72/69 s	$\sim$5 ppm	183
ZnO	Nanorods	Wet chemical route	NO_2	1	100^b	$\sim$5/$\sim$20 min	$\sim$1 ppm	110
ZnO	Nanowires	CVD	NO	10	46^b	—	1.5 ppm	184
ZnO	Nanocombs	CVD	CO	250	7.22	200/50 s	—	185
ZnO	Nanorod arrays	Microwave hydrolysis	CO	100	81.1^b	—/2.5 min	10 ppm	72
ZnO	Nanorods	Chemical deposition	H_2	150	$\sim$2^b	50–80/— s	—	186
ZnO	Nanorods	Hydrothermal	H_2	200	$\sim$4^b	30 s/50–90 s	$\sim$1 ppm	187
ZnO	Nanowires	CVD	H_2	121	8^b	29/— s	—	108
ZnO	Nanotubes	Aqueous chemical	H_2	500	29.6^b	—	—	188
ZnO	Thin films	Spray pyrolysis	H_2	150	63	320/200 s	—	189
ZnO	Nanorods	RF magnetron sputtering	H_2	1000	91^b	18.8/$\sim$130 s	0.2 ppm	173
ZnO	Nanorod arrays	Atomic layer deposition	H_2	500	162	30/— s	5 ppm	190
ZnO	Nanorod arrays	Chemical deposition	H_2	1000	500^b	176/116 s	—	191
MoO$_3$	Nanoribbons	Hydrothermal	H_2	1000	90^b	14.1/— s	0.5 ppm	192
SnO$_2$	Nano-films	Sol–gel	H_2	1000	2570^b	192/95 s	—	193
SnO$_2$	Nanotubes	Electrospinning	NO_x	9.7	89.2^b	6/218 s	9.7 ppb	95
SnO$_2$	Nanocrystals	Chemical precipitation	NO_2	11	33^a	100/250 s	$\sim$3 ppm	76
SnO$_2$	Thin films	Pulsed laser deposition	NO_2	4	7730	3/176 s	$\sim$4 ppm	157
SnO$_2$	Thin films	Sol–gel	Ozone	0.5	3.1	15/12 min	—	194
SnO$_2$	Nanorods	Microwave	O_2	10	$\sim$16.5^a	$\sim$200/$\sim$50 s	$\sim$1 ppm	73
SnO$_2$	Nanoporous	Hydrothermal	Acetone	100	14.64^a	30/20 s	$\sim$10 ppm	99
SnO$_2$	Nanocrystals	Sol–gel	NH_3	50	694.4^b	175/210 s	—	158
SnO$_2$	Nanowires	Precipitation	Ethanol	6000	8000	—	—	88
In$_2$O$_3$	Nanowires	CVD	H_2S	20	2	48/56 s	1 ppm	84
In$_2$O$_3$	Whiskers	Carbothermal	H_2S	10	30^b	4/120 min	200 ppb	104
In$_2$O$_3$	Nanotubes	Electrospinning	H_2S	20	167	287/636 s	$\sim$1 ppm	161
In$_2$O$_3$	Nanotubes	Electrospinning	H_2S	50	320.14	45/127 s	200 ppb	100
In$_2$O$_3$	Porous thin films	Template	H_2S	50	240 000	140/— s	1 ppm	101
In$_2$O$_3$	Microcrystallites	Thermal oxidation	NH_3	1000	92^b	100/60 s	$\sim$250 ppm	195
In$_2$O$_3$	Nanotubes	Precipitation	NH_3	20	2500	<20/20 s	$\sim$5 ppm	111
In$_2$O$_3$	Octahedra	Sol–gel	NO_2	200	$\sim$70	$\sim$500/$\sim$500 s	0.1 ppm	196
In$_2$O$_3$	Mesoporous nanocrystals	Hydrothermal	NO_x	97	158.7^a	96/— s	970 ppb	102
In$_2$O$_3$	Cubic crystals	Hydrothermal	Ethanol	100	1.4	5/3 s	$\sim$10 ppm	105
WO$_{3-x}$	Quantum dots	Solvothermal	HCHO	100	1.6	2/3 min	1.5 ppm	77
WO$_3$	Nanocolumns	Hydrothermal	Isopropanol	200	6.7	53/274 s	1 ppm	162
WO$_3$	Nano-films	Thermal evaporation	Ethanol	30	35^b	$\sim$300/300 min	$\sim$10 ppm	106
TiO$_2$	Thin films	Anodic oxidation	NH_3	100	0.32^a	<2/2 min	$\sim$50 ppm	107
TiO$_2$	Quantum dots	Hydrolysis method	NH_3	0.2	2.13	88/23 s	0.2 ppm	164
TiO$_2$	Nano-films	Sol–gel	NH_3	50	35^b	4/6 min	$\sim$10 ppm	163
TiO$_2$	Nano-films	Magnetron sputtering	NH_3	100	7857	34/90 s	5 ppm	174
TiO$_2$	Nanoparticles	Sol–gel	NH_3	100	10080.8	35.5/59 s	$\sim$1 ppm	78
TiO$_2$	Nanotubes	Electrochemical anodization	$CHCl_3$	20 000	$\sim$0.76	$\sim$3/— min	1000 ppm	167
TiO$_2$	Nanorods	Acid vapor oxidation	O_2	40 000	1.68	40/75 s	1000 ppm	74
TiO$_2$	Thin films	Magnetron sputtering	CH_3NH_2	10	11.3^b	200/260 s	$\sim$2 ppm	197
TiO$_2$	Nanodots	Nano-oxidation	NO	10	31^b	91/184 s	$\sim$5 ppm	165
TiO$_2$	Nanotube arrays	Electrochemical anodization	HCHO	50	$\sim$37^b	3/— min	0.04 ppm	176
TiO$_2$	Nanotubes	Electrochemical anodization	Methanol	1000	60^b	34/130 s	10 ppm	96
TiO$_2$	Nanotubes	Electrochemical	Acetone	100	70.18^b	19/14 s	$\sim$10 ppm	97
TiO$_2$	Nanoparticles	Hydrothermal	NO_2	40	1093	48/52 s	0.02 ppm	79
TiO$_2$	Nanorods	Hydrothermal	CH_4	60	6028	—	5 ppm	166
Fe$_2$O$_3$	Nanoparticles	Hydrothermal	H_2S	100	38.4	$\sim$180/$\sim$3700 s	50 ppb	80
Fe$_2$O$_3$	Nanonails	Screen printing	LPG	20 000	51	120/150 s	5000 ppm	168
MoO$_3$	Thin films	Magnetron sputtering	NO	200	92^b	30/1500 s	5 ppm	170
VO$_2$	Nanorods	CVD	NO_2	5	2.42	59/86 s	$\sim$1 ppm	171

Table 1 (*continued*)

Material	Structure	Synthesis method	Target gas	C (ppm)	Response	t_{res}/t_{rec}	LOD	Ref.
VO_2	Nanorods	Thermal evaporation	CH_4	500	35^a	75/158 s	~100 ppm	75
V_2O_5	Nanoneedles	Vapor deposition	Acetone	1.7	1.025	73/— s	941 ppb	175
CeO_2	Nanowires	Hydrothermal	H_2S	0.05	1.11	24/15 s	50 ppb	86

C = concentration; t_{res}/t_{rec} = response time/recovery time; LOD = limit of detection; response is defined as R_a/R_g (for reducing gases) or R_g/R_a (for oxidizing gases), R_a: resistance of the sensor exposed to the reference, R_g: resistance of the sensor exposed to the target. ^{a} Here the response is defined as $\Delta R/R_g$ (for reducing gases) or $\Delta R/R_a$ (for oxidizing gases), ΔR: the change in resistance. ^{b} Here the response is defined as $(\Delta R/R_g) \times 100\%$ (for reducing gases) or $(\Delta R/R_a) \times 100\%$ (for oxidizing gases).

the target gases, the gas molecules are absorbed on the surface of SMONs, and then react with these chemisorbed oxygen ions.

If the target gases are reducing gases, such as H_2S, H_2, NH_3, HCHO, or C_2H_5OH, the chemical reaction releases electrons, which are reinjected back to the electron depletion layer (see Fig. 3, the schematic diagram for H_2S gas sensing mechanism). This results in the reduction of the electron depletion layer and reduces the potential barrier energy ($\Delta\phi$). As a result, the surface resistance of SMONs is decreased. In contrast, if the target gases are oxidizing gases, such as NO, NO_2, Cl_2 and O_3, the reaction with the chemisorbed oxygen ions will capture the electrons, which will widen the electron depletion layer, resulting in an increase of the potential barrier energy ($\Delta\phi$). Accordingly, the surface resistance of the SMONs is increased.
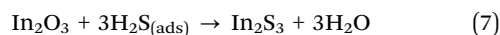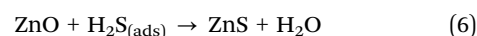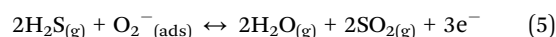
There are generally three definitions for the response values of n-type SMON based gas sensors, which are R_a/R_g, $(R_a - R_g)/R_g$ and $((R_a - R_g)/R_g) \times 100\%$ for the target reducing gases, respectively (where R_g and R_a are the resistance of sensors in the target gas and air, respectively). However, for the oxidizing gases, R_a and R_g need to be inter-changed in the above three definitions.[196] The time from the injection of the target gas to the time of reaching 90% of the final response is defined as the response time, and the time from the extraction of the gas to the time of reaching 10% of the final response is defined as the recovery time.

Generally, formation of chemisorbed oxygen ions determines the sensing performance. However, the gas sensing mechanism is sometimes attributed to the formation of new compounds as a result of reactions between the target gas and the surface of the SMONs. For example, H_2S gas molecules can react with ZnO

to form ZnS at RT.[71,109] Formation of such type of conductive metal sulfide significantly decreases the resistance of the SMON-based sensors, which accounts for high sensitivities of n-type SMON-based sensors for H_2S.

Chemical and electronic sensitization of the SMONs can be realized by adding noble metals on their surface and thus can remarkably enhance their sensing properties. Surface modifications and introduction of defects on the surfaces and interfaces such as introduction of heterojunctions[134] and vacancies[117] influence the sensing performance of SMON sensing materials. Addition of carbon nanomaterials on the surface of SMONs can also significantly improve their conductivity and enhance their sensitivities at RT.[135] In addition, an alkaline center[129] and hydroxide radicals[198] on the surfaces of SMONs have also been reported to affect the sensing properties, which will be discussed further.

2.1.2 Room temperature hydrogen sulfide sensors. N-type SMONs based on ZnO,[152] In_2O_3,[199] CeO_2[86] and Fe_2O_3[80] have frequently been reported for H_2S gas sensing at RT. Among these, ZnO and In_2O_3 are wide band-gap semiconductors, with band gaps of 3.3 eV and 3.6 eV, respectively. They are very effective for H_2S sensing because H_2S molecules can be easily decomposed and can react with the chemisorbed oxygen species on the surface of these sensing materials due to the small bond energy of H–S–H. On the surface of ZnO or In_2O_3, the H_2S molecules not only react with the oxide ions of O_2^- to form SO_2 and H_2O, but also react with ZnO or In_2O_3 to form ZnS or In_2S_3, based on the following reactions:[71,101,109]

$$2H_2S_{(g)} + O_2^-{}_{(ads)} \leftrightarrow 2H_2O_{(g)} + 2SO_{2(g)} + 3e^- \quad (5)$$

$$ZnO + H_2S_{(ads)} \rightarrow ZnS + H_2O \quad (6)$$

$$In_2O_3 + 3H_2S_{(ads)} \rightarrow In_2S_3 + 3H_2O \quad (7)$$

The reactions with the oxide ions increase electron concentrations on the surface of ZnO or In_2O_3, which leads to a significant decrease in resistance. Because ZnS and In_2S_3 are metallic conductors, the formation of ZnS or In_2S_3 also decreases the resistance of sensors, thus the responses to the gases are enhanced significantly at RT. Formation of ZnS or In_2S_3 is an exothermic process and spontaneously occurs at RT, so the sensors based on ZnO or In_2O_3 nanostructures are very suitable to detect H_2S at RT. Due to the formation of these metal sulfides, which are not reactive to most of the other gases, such as NH_3, H_2, NO_2, CO, CH_4, C_2H_5OH, and HCHO, the selectivity of RT sensors made of the nanostructured ZnO or

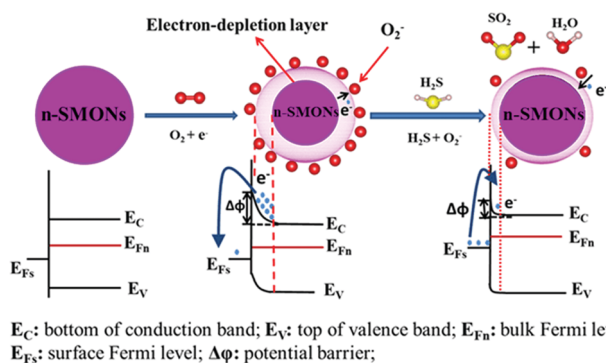**Fig. 3** Schematic diagram of the sensing mechanism of n-type semiconducting metal oxide nanostructures for reducing gas of H_2S.

E_C: bottom of conduction band; E_V: top of valence band; E_{Fn}: bulk Fermi level; E_{Fs}: surface Fermi level; $\Delta\phi$: potential barrier;

In_2O_3 to H_2S is excellent. Therefore, the ZnO and In_2O_3 nanostructured gas sensors generally have a high response and excellent selectivity for H_2S gas sensing.

The reaction of metal sulfides in the sensing process and the transformation of metal sulfides back to metal oxides in the recovery process are sometimes very slow at RT. Therefore, for the RT H_2S gas sensors, the response time and especially the recovery time are often relatively long, sometimes as long as several hours.[71,109] Furthermore, the sensors may not fully recover at RT.[101] The sensor should often be heated to a relatively higher temperature (*e.g.* 200 °C to 300 °C) in the recovery process for a complete recovery or shortening of the recovery time down to minute-scales.[109]

Hosseinia *et al.*[71] prepared vertically aligned ZnO rods with a diameter of 300–500 nm and a length of 1–9.5 μm using a vapor phase transport method. The nanorods are grown along the *c*-axis or (0002) planes perpendicularly to the substrate surface as shown in Fig. 4a. The porous network of vertically aligned ZnO rods forms directional channels, which facilitates the mobility of gas molecules. As shown in Fig. 4b, the sensor based on the vertically aligned ZnO rods shows a much higher response to H_2S at 26 °C than that at 250 °C, and its response value for H_2S at RT is almost 600 times larger than those for other gases, such as CH_4, CO, H_2S, methanol, ethanol, acetone, H_2 and He. However, at 250 °C, it is less than twice the original value. The response and recovery times of this sensor are very long, which are 320 s and 3592 s for 1 ppm H_2S as shown in Fig. 4c. ZnO nanorods were also grown using a hydrothermal method with diameters of 70–110 nm and lengths of 0.2–1.3 μm and then used for H_2S sensing.[109] These sensors exhibit a high response (about 35 to 1 ppm H_2S) and a very low LOD (50 ppb). However, its response time is longer than 20 min, and the

sensor is difficult to recover at RT. Response and recovery rates of RT H_2S gas sensors can be improved using dendritic ZnO nanostructures prepared using a vapor-phase transport method with Cu as the catalyst at 930 °C.[153] The multilevel branches of ZnO have well-oriented nanorods with diameters of 60 to 800 nm. The response/recovery times are 20/50 s, which make this sensor the fastest SMON-based H_2S sensor at RT reported so far. The sensor exhibits a high response of 26.4 to 500 ppm H_2S and good selectivity against various gases including H_2S, NH_3, H_2 and NO_2 in dry air at RT. The large degree modulation of the contact energy barriers due to the H_2S gas in ZnO dendrites is the key reason for their excellent sensing performance at RT.

Nanostructured In_2O_3 is another widely studied material for H_2S sensing. Apart from reactions of H_2S gas with oxygen ions on the surface of In_2O_3, the formation of In_2S_3 is another key factor for the sensor's high response at RT. Remarkably, the response value of the In_2O_3 nanostructure can reach 240 000 for 50 ppm of H_2S at RT[101] as shown in Fig. 4d. The micro/nanostructured porous In_2O_3 film was synthesized onto an Al_2O_3 ceramic tube using a self-assembly method,[101] which has an ordered porous structure with a thickness of 200 nm. Although the sensor does not fully recover to its baseline at RT, it can be rapidly and completely recovered at 300 °C. Using a conventional electrospinning process, Duan *et al.*[100] prepared In_2O_3 thick walled toruloid nanotubes. Owing to their larger surface areas, the nanotubes have more active sites among them, which results in enhanced responses to H_2S gas. The sensors based on the In_2O_3 nanotubes exhibit high response values of 320.14 to 50 ppm H_2S and fast response/recovery times of 45/127 s at the RT. In addition, good selectivity and a very low LOD with a value of 100 ppb have been demonstrated.[100] Porous In_2O_3 nanotubes with a cubic phase have been prepared using the electrospinning method,[161] and a high response value of 166.6 to 20 ppm H_2S has been demonstrated. However, the response/recovery times are quite long (287/636 s).

Other n-type SMONs such as α-Fe_2O_3[80] and CeO_2[86] have also been reported as good sensing materials for H_2S sensing at RT. For example, porous α-Fe_2O_3 nanoparticles with a diameter of 34 nm and pore sizes from 2 nm to 10 nm were obtained after annealing a FeOOH nanoparticle precursor.[80] The sensor based on these porous α-Fe_2O_3 nanoparticles exhibits a high sensitivity (38.4 for 100 ppm H_2S) with a low LOD (50 ppb). In addition, it has good selectivity to H_2S against the other gases (*e.g.*, C_2H_5OH, CO, H_2 and NH_3) and shows good reproducibility. The response time is fast with a value of 180 s. However, the recovery time is very long with a value of 3750 s for 100 ppm H_2S. CeO_2 nanowires[86] were also synthesized using a facile hydrothermal process and they show fast response/recovery times with values of 24/15 s for 50 ppb H_2S.

For the α-Fe_2O_3 and CeO_2 nanostructure-based H_2S gas sensors, the main sensing mechanism is the interactions of the H_2S molecules with the oxygen ions on their surface. Accordingly, the sensing is much faster than those sensors based on ZnO and In_2O_3, although their response to H_2S is much lower.[80,86]

2.1.3 Room temperature nitrogen dioxide sensors. Various SMON based gas sensors have demonstrated excellent sensing
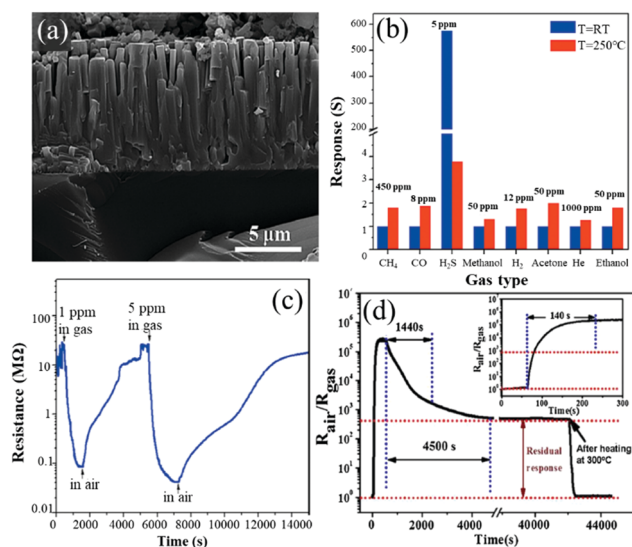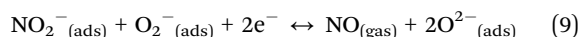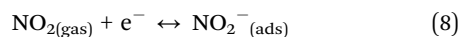

Fig. 4 (a) Cross-section SEM image of vertically aligned ZnO rods; (b) selectivity of the sensor at 25 °C and 250 °C; (c) response/recovery curves to 1 and 5 ppm H_2S at room temperature.[71] Copyright 2015, Elsevier. (d) The response/recovery curve at 50 ppm H_2S gas at room temperature.[101] Copyright 2017, Elsevier.

performance at RT for NO_2 gas sensing, using different materials such as ZnO,[110,200,201] SnO_2,[76] In_2O_3,[196] WO_3,[202–206] Sb_2O_5,[207] Bi_2O_3,[208] etc. The sensing mechanism of SMONs to NO_2 is based on the formation of NO_2^- by capturing electrons and the reaction between NO_2 gas molecules and O_2^- ions on the surface of the SMONs. All these reactions extract electrons from the surface of the SMONs, thus resulting in an increase in the resistance of these sensors, based on the following reactions:[209]

$$NO_{2(gas)} + e^- \leftrightarrow NO_2^-{}_{(ads)} \qquad (8)$$

$$NO_2^-{}_{(ads)} + O_2^-{}_{(ads)} + 2e^- \leftrightarrow NO_{(gas)} + 2O^{2-}{}_{(ads)} \qquad (9)$$

One of the outstanding features of SMON-based RT NO_2 gas sensors is their fast response speeds due to the strong oxidation of NO_2 molecules. Kodu et al.[157] reported NO_2 sensors based on granular SnO_2 thin films with a thickness of $\sim$90 nm deposited using a pulsed laser deposition method. The sensor exhibits not only a remarkably high response value of 7730 to 4 ppm NO_2, but also a very fast response time of 3 s at RT. Wei et al.[76] prepared SnO_2 nanocrystals by annealing $Sn(OH)_4$ precursor powders at 550 °C in both vacuum and ambient air environments, respectively. The vacuum-annealed SnO_2 and air-annealed SnO_2 nanocrystals have different particle diameters of 7.2 nm and 10.3 nm as shown in Fig. 5a. The response value of the vacuum-annealed SnO_2 sensor at RT is $\sim$2.4 to 5 ppm of NO_2, which is higher than that of air-annealed SnO_2 ($\sim$0.35). This is mainly because the increased oxygen vacancies on the surface of the vacuum-annealed SnO_2 are much more than those on the air-annealed SnO_2 nanocrystals, which can be identified by X-ray photoelectron spectroscopy (XPS) analysis as shown in Fig. 5b and c.

Yu et al.[91] prepared ZnO nanowalls with uniformly distributed and cross-linked nanowalls of $\sim$20 nm using a solution method. The cross-linked nanowalls have a porous structure with pore sizes from 200 nm to 500 nm. The sensor exhibits a high response value (6.4) and fast response/recovery times (23/11 s) towards 50 ppm NO_2 at RT with good repeatability. Based on the analysis from fluorescence emission spectrum, it was identified that the key factors for effective NO_2 sensing are (1) the presence of oxygen vacancies in the ZnO nanowall nanostructures, and (2) a delicate balance between oxygen vacancy defects and porosity.

TiO_2 and In_2O_3 are two other frequently reported nanomaterials for NO_2 sensing. Tshabalala et al.[79] prepared TiO_2 nanoparticles with an average particle size of 6.5 nm using a hydrothermal method. The fluffy and porous TiO_2 layer has a pore volume of 0.4170 cm^3 g^{-1} and a large surface area of 80.3 m^2 g^{-1}.[79] The porous nanostructures, high concentration of oxygen vacancies and the interstitial defect states on the surface are crucial for the efficient adsorption and desorption of NO_2 gas molecules. Therefore, the sensor made of these nanostructures exhibits a high response (1093 to 40 ppm NO_2), fast response/recovery times of 48/52 s and a low LOD of 0.02 ppm at RT. However, the selectivity of this sensor is poor with its relatively high responses to many other gases such as H_2, NH_3 and CH_4. In_2O_3 octahedra have also been prepared using the sol–gel technique for NO_2 sensing,[102] and the sensor using these In_2O_3 octahedra has a response value of 63 to 200 ppm NO_2 at RT, with good selectivity to NO_2 against CO, H_2 and NH_3.

2.1.4 Room temperature ammonia sensors. The sensing mechanism of SMON-based ammonia gas sensors operated at RT is also based on the reactions between NH_3 gas molecules and adsorbed O_2^- ions on the surfaces of the SMONs as shown in the following reactions:[92,183]

$$NH_{3(gas)} \rightarrow NH_{3(ads)} \qquad (10)$$

$$4NH_{3(ads)} + 3O_2^- \rightarrow 2N_2 + 6H_2O + 3e^- \qquad (11)$$
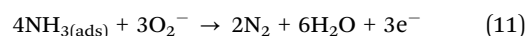
The majority of the single phase n-type SMONs without modifications by other elements can be used for NH_3 gas sensors, including ZnO,[210–212] In_2O_3,[111] SnO_2,[213] SnS_2,[214] MoO_3,[215] WO_3[216] and TiO_2.[217] They have good RT performance for NH_3 sensing with high responses and fast response/recovery. Among these, the sensors based on In_2O_3 and TiO_2 exhibit ultra-high responses and response/recovery times. For example, a RT sensor based on TiO_2 nanoparticles has an ultra-high response of 10080.8 to 100 ppm of NH_3 and fast response/recovery times of 35.5/59 s.[78]

Du et al.[111] reported a RT NH_3 gas sensor using porous In_2O_3 nanotubes. This gas sensor exhibits an ultra-high response

Fig. 5   (a) Response of vacuum-annealed SnO_2 compared to air-annealed SnO_2 nanocrystals to different concentrations of NO_2 at room temperature; the inset shows the TEM images of two types of nanocrystals; (b) and (c) deconvolution of the O 1s peaks of X-ray photoelectron spectra (XPS) for vacuum−SnO_2 and air−SnO_2 (the peaks with red color belong to adsorbed O ions).[76] Copyright 2016, Elsevier.

value of 2500 and good reproducibility with response and recovery times less than 20 s, both of which are better than those of the sensors made of In_2O_3 nanowires or nanoparticles. The performance enhancement is attributed to the porous structure and ultra-high surface-to-volume ratio of the porous In_2O_3 nanotubes, which can adsorb more oxygen molecules. Another gas sensor made of TiO_2 films prepared using a reactive magnetron sputter method also exhibits an excellent response with a value of 7857 to 100 ppm of NH_3, fast response/recovery times of 34/90 s and a low LOD of ~5 ppm.[174] Kumar et al.[83] used an anodic aluminum oxide template route to prepare highly ordered ZnO nanowire arrays as the sensing layer for detection of NH_3. The diameters of these nanowires are in the range of 60 to 70 nm and their length is about 11 μm as shown in Fig. 6a. At RT, the sensor exhibits 68% of response value (defined as $(\Delta R/R_g) \times 100\%$) to 50 ppm NH_3 and fast response/recovery times (28/29 s) (see Fig. 6b).[83] Another NH_3 sensor made of nanostructured ZnO thin films[112] synthesized using a magnetron sputtering technique shows a high response with a value of 304 to 100 ppm NH_3 with response/recovery times of 92/113 s.

Mani et al.[182] reported a sensor made of a nanostructured ZnO thin film (shown in Fig. 6c) using a spray pyrolysis technique. As shown in Fig. 6d, the sensor using this thin film exhibits a high response with a value of 233 to 25 ppm of NH_3 at RT, and fast response and recovery times of 20/25 s. It has good selectivity to ammonia gas against other VOC gases (i.e. ethanol, methanol, benzyl alcohol, 2-propanol and acetone). Moreover, the sensor is insensitive to relative humidity. However, the sensor becomes saturated when the concentration of NH_3 is above 20 ppm, indicating that the LOD is about from 5 ppm to 25 ppm. In brief, high responses, fast response/recovery, and superior LOD have been achieved for the n-type SMON-based RT NH_3 gas sensors.
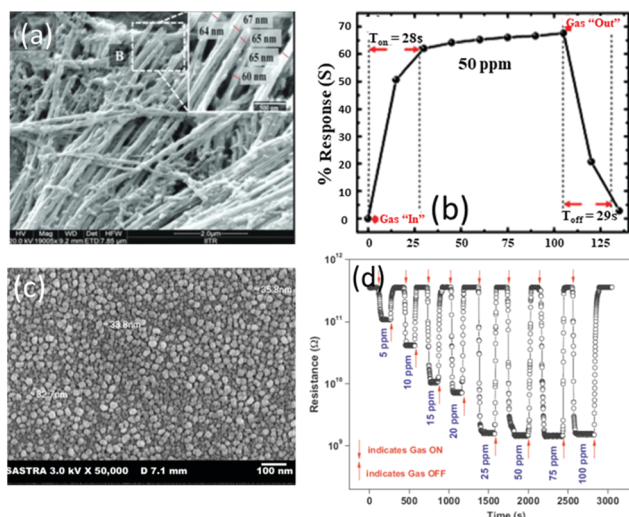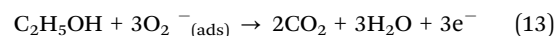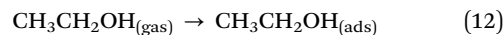

Fig. 6 (a) SEM images of the ZnO nanowire array; (b) response/recovery curves of the ZnO nanowire array for 50 ppm NH_3.[83] Copyright 2014, Royal Society of Chemistry. (c) SEM image of nanostructured ZnO thin films on glass substrates; (d) response/recovery curves of the nanostructured ZnO thin film-based sensor for NH_3.[182] Copyright 2013, Elsevier.

2.1.5 Room temperature ethanol sensors. Most n-type SMONs made of ZnO,[218–220] Fe_2O_3,[221] SnO_2,[222] In_2O_3,[105] TeO_2[85] and WO_3[106] can be used for ethanol sensing. The sensing mechanism of n-type SMON-based ethanol gas sensors is based on the interaction of ethanol gas molecules with chemisorbed O_2^- ions on the surfaces of the SMONs. The ethanol molecules react with the adsorbed oxygen ions to form CO_2 and H_2O. Subsequently, electrons are released thus resulting in an increase in electron density and a decrease in potential barrier energy. These can be expressed using the following reactions:[180]

$$CH_3CH_2OH_{(gas)} \rightarrow CH_3CH_2OH_{(ads)} \qquad (12)$$

$$C_2H_5OH + 3O_2^-{}_{(ads)} \rightarrow 2CO_2 + 3H_2O + 3e^- \qquad (13)$$

The RT ethanol gas sensors based on the n-type SMONs usually exhibit rapid response and recovery. For example, a sensor based on In_2O_3 cubic crystals[105] prepared using a hydrothermal method exhibits very fast response/recovery (3/5 s). However, the response is poor with a value of only 1.4 to 100 ppm ethanol vapors. Fast response/recovery times together with high responses have been reported for a sensor made of ZnO nanowires.[82,180] Shankar et al.[82] reported an ethanol sensor made of ZnO nanowires (see Fig. 7a) prepared using electrospinning. Self-assembled ZnO nanowires with two different molecular weights of poly(vinyl alcohol) (PVA), e.g., 14 000 and 140 000 g mol^{-1}, were prepared using an electrospinning technique, and then heat-treated to transform them into ZnO nanospheres and nanowires at a temperature of 600 °C. These nanostructures have good selectivity to ethanol compared to other VOCs including ethanol, methanol, acetaldehyde, and acetone when operated at RT. The nanowire based sensors have a higher ethanol response (78 to 100 ppm) than those based on the nanoparticles (about 48 to 100 ppm).[76] The nanowire-based ones also show fast response/recovery times of 9/12 s. Furthermore, the nanowire-based sensor has excellent repeatability.

Fig. 7b shows a schematic diagram of the ethanol sensing mechanism for the ZnO-based sensor.[82] The chemisorption of oxygen molecules on the sensor surface results in the formation of a space charge region on the surface of ZnO, which can act as a barrier for electron transport in the ZnO sensing layer.[82] Due to the formation of double-spaced charge layers from the intergranular contacts of nanoparticles, the potential barrier energy is increased, which results in the broadening of the percolation path and hinders the electron transport. This further influences the adsorption–desorption rate and the sensing properties towards ethanol. However, the intergranular contact resistance will be reduced in the ZnO nanowires, which decreases the potential barrier energy, thus enhancing the sensing performance.

Similarly, TiO_2 nanotubes[96] prepared using an electrochemical anodization method and TeO_2 nanowires[85] prepared using thermal evaporation also show good responses to ethanol.[85,96] However, the selectivity is poor as they are also sensitive to methanol and propanol.

2.1.6 Room temperature hydrogen sensors. Hydrogen gas is one of the extremely flammable and explosive gases. Therefore, detection of traces of hydrogen gas using RT gas sensors is
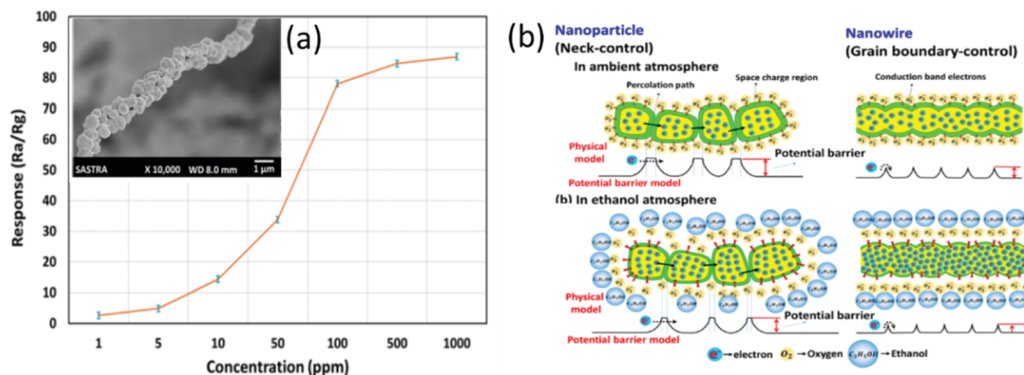
Fig. 7 (a) Responses of the ZnO nanowire sensor to different concentrations of ethanol at room temperature; the inset shows the SEM image of ZnO nanowires; (b) the schematic diagram of the ethanol sensing mechanism.[82] Copyright 2017, American Chemical Society.

critical to avoid the dangers of explosion. For this application, the sensors must be fast, highly sensitive and selective. In particular, the fast response is paramount for a timely detection of a possible hydrogen leakage. As summarized in Table 1, the SMONs made of ZnO,[188,189] MoO$_3$[192] and SnO$_2$[193] have been demonstrated for hydrogen sensing at RT using various nano-structures including nanofilms,[189] nanowires,[108] nanotubes[188] and nanorods.[190,191] The sensing mechanism is based on the reaction of H$_2$ molecules with chemisorbed O$_2^-$ ions on the surface of the SMONs, as shown in the following chemical equation:[189]

$$2H_2 + O_2^-{}_{(ads)} \rightarrow 2H_2O + e^- \tag{14}$$
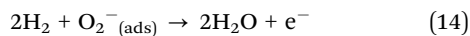
From the literature, sensors made from ZnO films[189] and ZnO nanorods[191] show high responses to H$_2$, but long response/recovery times (see Fig. 8).

Fig. 8 (a) AFM image of the ZnO films and (b) response/recovery curves of a ZnO film-based gas sensor to different concentrations of H$_2$.[189] Copyright 2014, Springer Nature. (c) Cross section SEM image of the ZnO nanorods and (d) response/recovery curves of a ZnO nanorod-based gas sensor to different concentrations of H$_2$.[191] Copyright 2013, Elsevier.
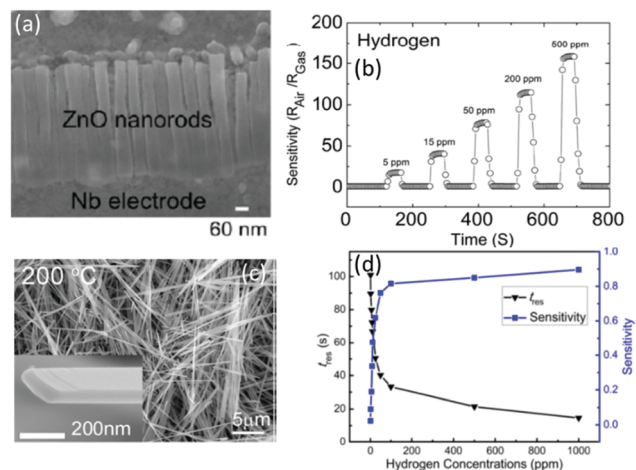

Fig. 9 (a) TEM image of vertical ZnO nanorods; (b) response/recovery curves of a vertical ZnO nanorod-based gas sensor *versus* different concentrations of H$_2$.[190] Copyright 2012, Elsevier. (c) SEM images of α-MoO$_3$ nanoribbons; (d) response values and times of an α-MoO$_3$ nanoribbon-based gas sensor *versus* different concentrations of H$_2$.[192] Copyright 2015, American Chemical Society.

Using anodized aluminum oxides as nano-templates, Lim *et al.*[190] synthesized vertical ZnO nanorods (see Fig. 9a) using atomic layer deposition, and a highly sensitive and fast response/recovery H$_2$ gas sensor was fabricated using these vertical ZnO nanorods. A response value of 162 for 500 ppm H$_2$ and a response time of 30 s were demonstrated (see Fig. 9b).[190] A faster response H$_2$ gas sensor was also reported using [001]-oriented α-MoO$_3$ nanoribbons (see Fig. 9c)[192] with a response time of 14.1 s for 1000 ppm of H$_2$ and a low LOD of 500 ppb (see Fig. 9d).[192] It has good reproducibility and high selectivity against ethanol, CO and acetone.

In brief, RT gas sensors based on n-type SMONs can detect most of the hazardous gases, with advantages such as easy preparation, low cost, simple post-treatment and good stability of structure. Various morphologies of nanostructures for n-type SMONs have been synthesized and used in gas sensors operated at the RT. These sensors have been widely used to detect various gases and some good sensing properties have been achieved.

However, it should be addressed that for most of these n-type SMON-based RT gas sensors, their sensitivity at RT is much lower than that at a higher working temperatures. Their responses and recovery times are quite long, and sometimes these sensors cannot be fully recovered at RT. In addition, at RT, the sensing performance is seriously affected by various environmental factors, such as humidity and external light source. To enhance their sensing properties at RT, modification of these n-type SMONs should be adopted, which will be discussed in Section 3.

2.2 P-type semiconducting metal oxide nanostructures and gas sensors

Up to now, the major p-type SMONs used in RT gas sensing have been CuO,[223–225] Co_3O_4[92,103] and NiO,[94,226] and the main target gases include NH_3,[98,103] H_2S[224,225] and NO_2,[226] as listed in Table 2. Apart from the sensing mechanism which is based on the reaction of target gases with the oxygen ions on the surface of SMONs, the formation of metal sulfides is another key reason for H_2S sensing, especially for CuO nanostructures.[93,225]

2.2.1 Gas sensing mechanisms. Generally, the sensing mechanism of p-type SMONs is based on the changes of surface resistance as a result of the changes in the concentrations of hole carriers due to their redox reaction with the target gases. When exposed to air at RT, the oxygen ions of O_2^- are formed from the adsorbed oxygen molecules on the surface of p-type semiconductors and they capture electrons from the conduction band of the SMONs. The density of hole carriers is increased, thus resulting in a decrease in the surface layer's Fermi level.

Due to an accumulated hole layer formed on the surface of p-type SMONs, the conductivity will be increased and the resistance of the sensors is decreased. This is opposite to the sensing mechanism for the n-type SMON sensors discussed in the last section.

The sensing mechanism of the p-type SMONs to the reducing gas of NH_3 is schematically shown in Fig. 10. When the reducing gas molecules (such as NH_3) are adsorbed on the surface of SMONs, the reaction between the NH_3 and O_2^- ions will release electrons, which will combine with the holes, resulting in an increase in the Fermi level and reduction of the hole accumulation layer. Consequently, the conductivity of the SMON layer is decreased. However, for the oxidizing gases, more free electrons are captured from the surface of the p-type SMONs. For example, the NO_2 molecules adsorbed on the sensor surface can capture electrons from the p-type SMONs to form NO_2^- as listed in the reaction eqn (8). This significantly increases the concentrations of hole carriers, thus resulting in the increase in conductivity of the p-type SMON-based gas sensors. In summary, the resistance of p-type SMON based sensors will be increased in the presence of the reducing gases, whereas their resistance will be decreased in the presence of the oxidizing gases.

2.2.2 Room temperature hydrogen sulfide sensors. At present, the dominant p-type SMON for RT H_2S gas sensors is CuO, which exhibits excellent sensing performance when operated at RT, especially with high sensitivity and fast response and recovery. Different from the sensing mechanisms discussed above which are based on the reactions between the target gases with the

Table 2 Summary of room temperature sensing properties of p-type semiconducting metal oxide nanostructures

Material	Structure	Synthesis method	Target gas	C (ppm)	Response	t_{res}/t_{rec}	LOD	Ref.
CuO	Nanosheets	Hydrothermal	H_2S	0.01	1.25	234/76 s	10 ppb	93
CuO	Flowers	Hydrothermal	H_2S	1	2.1	240/1341 s	0.1 ppm	225
CuO	Nanofibers	Electrospinning	H_2S	100	2.23	4.3/— s	1 ppm	227
CuO	Tubes	Biotemplate	H_2S	5	~41	29/41 s	2 ppb	98
CuO	Thin films	Thermal evaporation	H_2S	5	~250[b]	60/90 s	100 ppb	224
CuO	Nanorectangles	Hydrothermal	NH_3	5	~0.25[a]	90/120 s	5 ppm	223
CuO	Nanoparticles	Sol–gel-combustion	NH_3	100	0.99[a]	30/— s	—	228
CuO	Nanoparticles	Sol–gel-combustion	NH_3	100	9.83[a]	~150/~500 s	—	81
CuO	Microspheres	Reflux method	NO_x	97	64.93[b]	5.33/— s	0.97 ppm	90
Cu_xO	Virus-like	Chemical solution	NO_2	4	28.1	22/42 s	1 ppm	229
CuO	Nanoplatelets	Sonochemical method	NO_2	40	53 737	—	—	230
CuO	Nanowires	Thermal oxidation	Ethanol	100	202	0.19/0.19 s	~10 ppm	36
CuO	Nanoribbons	Wet chemical	Ethanol	100	210[b]	8/25 s	20 ppm	231
NiO	Nanosheets	Microwave synthesis	NO_2	10	0.56	—	—	232
NiO	Nanosheets	Hydrothermal	NO_2	60	3.05[a]	~200/~300 s	~5 ppm	94
NiO	Nanosheets	Hydrothermal	NO_2	60	1.8[a]	~250/~250 s	~7 ppm	226
NiO	Dendritic-like	Electrolytic	NH_3	30	19[b]	40/1500 s	—	233
Co_3O_4	Nanosheets	Hydrothermal	NH_3	100	9.5	9/134 s	0.2 ppm	92
Co_3O_4	Porous structure	Template	NH_3	100	146[b]	2/— s	0.5 ppm	103
Co_3O_4	Nanosheets	Hydrothermal	CO	50	—	15/20 s	—	234
Co_3O_4	Nanoparticles	Thermal treatment	NO_x	100	52.1[b]	—	100 ppb	235
Cr_2O_3	Nanospheres	Hydrothermal	Ethanol	40	9[a]	—	5 ppm	236
Cr_2O_3	Mesoporous	Impregnation	Ethanol	1000	13.0	—	10 ppm	237
$\alpha-MnO_2$	Nanospheres	Self-assembly	NH_3	20 000	0.2	—	—	238
MnO_2	Nanofibers	Chemical solution	NH_3	100	20[b]	—	1 ppm	239
$\beta-MnO_2$	Thin films	Spray pyrolysis	CH_3COH	10	89[b]	60/11 s	10 ppm	240

C = concentration; t_{res}/t_{rec} = response time/recovery time; LOD = limit of detection; response is defined as R_a/R_g (for reducing gases) or R_g/R_a (for oxidizing gases), R_a: resistance of the sensor exposed to the reference, R_g: resistance of the sensor exposed to the target. [a] Here the response is defined as $\Delta R/R_g$ (for reducing gases) or $\Delta R/R_a$ (for oxidizing gases), ΔR: the change in resistance. [b] Here the response is defined as $(\Delta R/R_g) \times 100\%$ (for reducing gases) or $(\Delta R/R_a) \times 100\%$ (for oxidizing gases).

Fig. 10 Schematic diagram of the sensing mechanism for p-type semiconducting metal oxide nanostructures to reducing gas of NH_3.
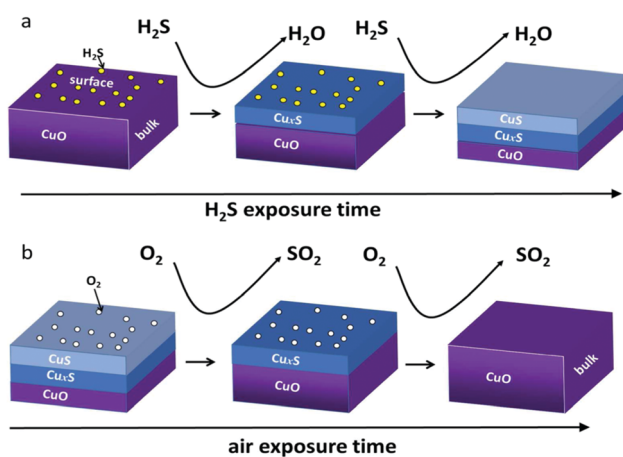

Fig. 11 Schematic diagrams of the sensing mechanism of CuO: (a) response process in H_2S and (b) recovery process in air.[93] Copyright 2016, American Chemical Society.

oxygen ions, the formation of CuS is highly responsible for the sensing response to H_2S at RT.

Fig. 11 shows schematic diagrams of the sensing mechanism for CuO-based H_2S sensors. H_2S molecules can react with CuO to form CuS on the surface at RT, based on the following reactions:[93,225]
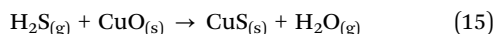
$$H_2S_{(g)} + CuO_{(s)} \rightarrow CuS_{(s)} + H_2O_{(g)} \qquad (15)$$

$$CuS_{(s)} + O_{2(g)} \rightarrow CuO_{(s)} + SO_{2(g)} \qquad (16)$$

CuS is a metallic-like conductor. Formation of CuS on the SMON's surface will dramatically decrease the resistance of the sensor. Consequently, although H_2S is a reducing gas, the response of the sensors exhibits a decrease in resistance. The RT H_2S gas sensors are highly selective owing to this unique interaction between H_2S and CuO. However, their recovery times are relatively long at RT due to the requirement for the transformation from CuS to CuO.

This H_2S sensing mechanism has been proved from different studies. For example, Li et al.[93] reported a H_2S sensor based on porous CuO nanosheets with a thickness of about 60 nm on alumina tubes, prepared using a hydrothermal method. The sensor based on these porous CuO nanosheets has excellent selectivity to H_2S. It exhibits high response values to H_2S, but no apparent responses to NH_3, CO, NO, NO_2, H_2, and C_2H_5OH.[93] The sensor has a superior LOD as low as 10 ppb and good reproducibility at RT. The sensing mechanism based on the transformation from CuO into CuS on the surface of nanosheets has been verified using XPS analysis. As seen from the XPS spectra in Fig. 12, after the CuO is exposed to H_2S gas, a new peak of the Cu $2p_{3/2}$ state at 930.8 eV appears which is attributed to CuS, and the S $2p_{3/2}$ and S $2p_{1/2}$ states at 162.3 and 163.4 eV can be identified. Similarly, nanostructures of hierarchical flower-like CuO nanostructures[225] have been prepared, and the sensors made of these nanostructured CuO exhibit high sensitivity, good reproducibility and high sensing selectivity to H_2S at RT. Zhang et al.[98] prepared tube-like CuO nanostructures using pomelo flesh as a bio-template. The unique tube-like CuO nanostructures enhance the diffusion of H_2S molecules and promote the rapid formation of CuS. The H_2S sensor based on the tube-like CuO nanostructures has good selectivity to H_2S, compared to gases such as gasoline, formaldehyde, CH_4, H_2, acetone, CO, toluene, and ethanol. The response/recovery times are lower than 60 s for the H_2S in a wide range of 10 ppb–10 ppm. In addition, the sensor demonstrates a stable detection performance at RT over 3 months.

2.2.3 Room temperature ammonia sensors. The CuO nanostructures are also suitable for NH_3 sensing at RT. Sakthivel et al.[223] fabricated a flexible NH_3 sensor on a polyethylene terephthalate substrate using CuO nano-rectangles, which were synthesized using a surfactant-free hydrothermal method. The flexible RT sensor made of the CuO nano-rectangles is effective

Fig. 12 (a) Cu $2p_{3/2}$ and (b) S 2p XPS spectra of porous CuO nanosheets before and after exposure to H_2S.[93] Copyright 2016, American Chemical Society.

Fig. 13 (a) SEM image of network Co_3O_4 nano-sheet arrays; (b) response/recovery curves of the network Co_3O_4 nano-sheet array based sensor to different concentrations of H_2S at room temperature (the inset shows the response value).[92] Copyright 2016, Elsevier.

for sensing ammonia even under different bending conditions as it exhibits identical response and response/recovery times. Furthermore, this flexible NH_3 sensor exhibits both good stability and reproducibility in a three-month testing period.[223]

Co_3O_4 nanostructures[92] have also been found to be effective for NH_3 detection with fast response speeds at RT. Fig. 13a shows an image of a Co_3O_4 nano-sheet array network deposited on an alumina tube prepared using a hydrothermal method. The average sheet thickness of the Co_3O_4 nano-sheet is 39.5 nm. NH_3 molecules react with the surface chemisorbed O_2^- ions and form N_2 and H_2O. As shown in Fig. 13b, the response time for the gas sensor is as short as 9 s for 0.2 ppm NH_3 at RT. The sensor responds linearly to the concentrations of NH_3 within a range between 1–100 ppm. It also exhibits good performance in terms of reproducibility, stability and selectivity to NH_3 (compared to H_2, CO, H_2S and C_2H_5OH). 3D hierarchical porous Co_3O_4 nanostructures[103] were synthesized by Wu *et al.* using polystyrene spheres as the template. The average particle size is 20 nm and the specific surface area is 58.75 $m^2 g^{-1}$. The structures have macro-size pores, mesopores and plenty of irregular structural defects. The sensor made of these porous Co_3O_4 nanostructures exhibits a sensitivity of 146% (defined as $(\Delta R/R_g) \times 100\%$) to 100 ppm NH_3, and has a fast response time of 2 s. However, the recovery time is very long, *e.g.*, longer than 1000 s.[103]

Apart from CuO and Co_3O_4 nanostructures, NiO[233,238] and MnO_2[239] were also used to make RT NH_3 gas sensors, although the response was found to be very slow. Applying special nano-structures can improve the responses of the sensors. For example, the hierarchical hollow nanospheres of α-MnO_2 composed of densely aligned nanowires were reported to exhibit an improved NH_3 gas sensing sensitivity, and faster response and recovery compared with the standard α-MnO_2 nanowires.[238] Doping with metal ions such as Al doped NiO was also reported as an effective route for improving the sensitivity and responses of the sensor operated at RT.[233]

2.2.4 Room temperature nitrogen dioxide sensors. P-type nanostructures have also been reported as good RT NO_2 sensing materials. When they are exposed to the oxidizing gases, such as NO_x, the NO_x molecules are absorbed on the surface and form NO_x^- and holes, and the reactions of NO_x with the chemisorbed oxygen ions also increase the concentration of holes on the surface,

which can be revealed from the reaction eqn (17)–(19).[235] These reactions will widen the width of the accumulated hole layer on the surface of p-type SMONs, and cause the increase in conductivity of the sensors.

$$NO_{x(gas)} \leftrightarrow NO_x^-{}_{(ads)} + h^+ \qquad (17)$$

$$NO_{(gas)} + O_2^-{}_{(ads)} \leftrightarrow NO_2^-{}_{(ads)} + O^-{}_{(ads)} + h^+ \qquad (18)$$

$$NO_{2(ads)} + O_2^-{}_{(ads)} \leftrightarrow NO_3^-{}_{(ads)} + 2O^-{}_{(ads)} + h^+ \qquad (19)$$

Self-assembled mesoporous Cu_xO virus-like microspheres[229] exhibited a high response of 28.4 and response/recovery times of 22/42 s to 4 ppm NO_2 gas measured at RT. The good sensing performance of this special microstructure is attributed to the formation of hierarchical 3D nanostructures, micropores and large surface area for effective gas diffusion, the abundant surface oxygen vacancies and the heterojunctions at the inter-faces between CuO and Cu_2O. The RT NO_2 gas sensors were also made using unique chain Co_3O_4 structures[235] and self-assembled polycrystalline hexagonal NiO nanosheets.[226] Because of the reduced grain boundaries, which minimizes the carriers' scattering at the interfaces during the chemisorption of NO_2, these special Co_3O_4 nanostructures showed much better responses to NO_2 than those made of the Co_3O_4 and NiO nanoparticles.

Apart from detecting H_2S, NH_3 and NO_2, the RT sensors based on the p-type SMONs have also been used for detecting other types of gases. For example, a sensor made of MnO_2 shows good sensing performance for acetaldehyde vapor,[240] and at ambient temperature, β-MnO_2 thin films were reported to have good sensing responses and fast response/recovery. The sensitivity was found to be 89% for sensing 10 ppm acetaldehyde vapor, and the response and recovery times were found to be of 60 s and 11 s, respectively. This sensor also showed good selectivity to acet-aldehyde gas, compared with the other reducing gases such as acetone, benzene, diethylamine, ethanol, dimethylamine, 2-propanol, monomethylamine and ammonia.[240] Sensors made of Co_3O_4 nanosheets were also reported to have very fast response and recovery of 15/20 s to 50 ppm CO and CH_4.[234]

The p-type Cr_2O_3 based gas sensor is normally operated at higher temperatures above 100 °C, and there are few reports about the Cr_2O_3 based RT gas sensors. However, 3D cubic

mesoporous Cr_2O_3 nanostructures were recently prepared and the sensor made of this nanostructure exhibits an enhanced sensitivity for detecting ethanol vapor at room temperature, which is much better than those of the dense Cr_2O_3 film.[237] The response of the 3D cubic mesoporous Cr_2O_3 sensor is 13.0 to 1000 ppm ethanol, whereas it is only 2.0 for the dense Cr_2O_3 film.

Although there are some reports on using the p-type SMONs in gas sensors operated at high temperature, these are much fewer compared to those on using n-type SMONs. The sensitivity of p-type SMON sensors is generally not as high as that of the n-type SMON sensors. Modification of the p-type SMONs using noble metal nanoparticles or metal ions is an effective route to further enhance the sensing performance, which will be discussed in Section 3.

3. Room temperature gas sensors based on modified and composite semiconducting metal oxide nanostructures

3.1 Metal modified semiconducting metal oxide and gas sensors

3.1.1 Gas sensors based on noble metal modified semiconducting metal oxide nanostructures.
Due to their chemical sensitization and electronic sensitization, noble metals have been widely applied for surface modifications of SMONs, which has become one of the effective routes to improve their sensing performance, especially for the sensors operated at RT.[241] This can be seen from the comparison of room temperature sensing properties between the pristine and noble metal modified SMONs as listed in Table 3. So far, the noble metals used to modify the SMON based gas sensors are mainly Au,[242–246] Ag,[247,248] Pt[249,250] and Pd.[251–254] Nanoparticles of the noble metals are usually decorated onto surfaces of SMONs using the wet-chemical method,[116] thermal vaporization,[253] sputtering method[255] and electrospinning technology.[256] Many of these sensors have the commonly reported spill-over effect,[241] which means that the active centers on the surface of the solid catalyst produce oxygen active species by adsorbing oxygen molecules. Due to this effect, more oxygen ions are formed on the surface of the SMONs. Being excellent active catalysts, noble metal nanoparticles can facilitate the adsorption of oxygen molecules and enhance the formation of oxygen ions by chemical reduction, which then spill onto the surface of the SMONs, thus increasing the concentration of oxygen ions. The target molecules can also be directly adsorbed onto these noble metal nanoparticles, and then they migrate onto the surface of the SMONs to react with the oxygen ions. These spill-over effects significantly enhance the sensing performance. In addition, these noble metal nanoparticles can also accelerate the transfer of electrons onto the surfaces of the SMONs. Therefore, both the chemical sensitization and electronic sensitization enhance the sensitivity and speed of the SMON-based sensors.

At RT, some gases such as CO and H_2 are very difficult to detect using the sensors made of pristine SMONs. However, this problem might be solved by modifying the surface of these SMONs using noble metal nanoparticles. For example, Arunkumar et al.[113] prepared ZnO nanostar features using a hydrothermal route and then decorated these nanostars using Au nanoparticles with an average size of ∼5–6 nm as shown in Fig. 14a. The ZnO nanostars decorated with 3 wt% gold nanoparticles can enhance the response (∼15 for 50 ppm CO) and achieve very fast response/recovery times (∼8/15 s) at 35 °C.[113] The selectivity of the sensor for Co sensing is excellent against the other interfering gases including methanol, ethanol, acetone and hydrogen. Fig. 14b shows the energy band diagrams of ZnO and Au/ZnO nanostars before and after CO exposure. Due to the spillover effect, a nanoscale depletion region is formed at the interface between Au nanoparticles and ZnO as a result of strong electronic interactions, thus altering the height of the Schottky barrier. Therefore, the enhanced performance of the sensor operated at RT is attributed to the spillover effect.[113]

Choi et al.[114] grew a network of ZnO nanowires using a vapor–liquid–solid method and then these nanowires were functionalized with Pd nanodots using a γ-ray radiolysis method, and the sensor made of these decorated nanowires shows an improvement of the sensing performance. This improvement is attributed to the electronic and chemical sensitizations from the Pd nanodots.[114] Wang et al.[115] reported a highly sensitive RT CO sensor based on Pt/SnO_2 porous nanostructures. The porous SnO_2 nanostructures were synthesized using a solvothermal method, and Pt nanoparticles were then decorated onto the SnO_2 using hexachloro-platinic acid. The sensor exhibits a good response with a value of 64.5 to 100 ppm CO at RT. It also shows good selectivity, compared to the other gases including CO, H_2, $N(CH_3)_3$, NH_3 and CH_4. Similarly, a RT CO gas sensor made of Au/In_2O_3 composite nano-rods was fabricated, and showed a high response and fast response/recovery times (30/30 s to 100 ppm CO).[244]

Modification of SMONs by noble metals can not only enhance the sensitivity, but also significantly improve the selectivity and response/recovery speed. For example, a ZnO nanowire-based sensor modified with Pd nanoparticles exhibits both ultra-high sensitivity and very fast response and recovery.[252,265] A Pd-modified ZnO nanowire-based RT nanosensor was prepared using electrochemical deposition by Lupan et al.,[252] and it exhibits very fast response/recovery times of 6.4/7.4 s and a super-high response value of 13 100 to 100 ppm H_2 as shown in Fig. 15a and b. This H_2 sensor shows very good selectivity against the other gases such as CO, CH_4, ethanol and acetone. The sensor can be operated at very low current levels with ultra-low power consumption.[252]

Ultra-sensitive RT hydrogen gas sensors based on noble metal modified SnO_2 have also been reported. For example, the sensor based on Pt/SnO_2 nanoparticles exhibits a super-high response (e.g., 10 500 to 1000 ppm H_2) at RT.[249] Lee et al.[253] reported a RT hydrogen sensor made of Pd/SnO_2 nanowires (as shown in Fig. 15c) prepared using a thermal evaporation method, and the sensor shows an ultra-high sensitivity of about 120 000% (defined as $(\Delta R/R_g) \times 100\%$) to 10 000 ppm H_2 and a

Table 3 Comparison of room temperature sensing properties of the noble metal modified semiconducting metal oxide nanostructures

Material	Structure	Synthesis method	Target gas	Concentration (ppm)	Response value	t_{res}/t_{rec}	LOD	Ref.
Pt/ZnO	Nanowires	Vapor–liquid–solid	CO	0.1	1.02	120/180 s	100 ppb	114
ZnO					0	—	—	
Au/ZnO	Nanostars	Hydrothermal	CO	50	55.3	10/12 s	5 ppm	113
ZnO				1000	0	—	—	
Au/ZnO	Nanowires	Hydrothermal	H_2S	5	79.4	—/170 s	~1 ppm	242
ZnO					5	—/860 S	—	
Au/ZnO	Nanorods	Vapor phase transport	H_2S	3	~475	11/20 min	~0.5 ppm	257
ZnO					~125	10/13 min		
Au/ZnO	Core–shells	Sol–gel	HCOH	5	10.57	138/104 s	500 ppb	258
ZnO	Shells				1.91	332/736 s	—	
Pd/ZnO	Nanoparticles	Sol–gel	NO_2	50	45.2^b	67/250 s	10 ppm	251
Pt/SnO_2	Porous	Solvothermal	CO	100	64.5	144/882 s	~50 ppm	115
Au/SnO_2	Nanoparticles	Sputtering	NO_2	50	90^b	70/— s	600 ppb	243
SnO_2					$\sim25^b$	—	—	
Au/In_2O_3	Nanorods	Aqueous solution	CO	100	9	30/30 s	~50 ppm	244
In_2O_3					0	—	—	
Au/TiO_2	Core–shells	Sol–gel	O_3	2.5	3.27	5/24 s	0.4 ppm	259
TiO_2	Shells				1.36	32/76 s	—	
Ag/TiO_2	Nanoparticles	Sol–gel	Ethanol	5	4.35	52/61 s	0.15 ppm	247
TiO_2					1.54	112/136 s	—	
Pd/TiO_2	Nanofiber array	Electrospinning	NH_3	100	6.97	3/150 s	~0.1 ppm	260
TiO_2					0	—	—	
Ag/TiO_2	Nanorods	Wet chemical	Ethanol	50	11.98^a	3/73 s	~5 ppm	116
TiO_2					8.15^a	6/213 s	—	
Au/VO_2	Nanowires	CVD/Ion sputtering	NO_2	5	3.22	~50/~600 s	~0.5 ppm	130
VO_2		CVD			~1	—	—	
Pt/VO_x	Thin films	Magnetron sputtering	CH_4	500	18.2^b	~1000/~2000 s	~500 ppm	261
Au/VO_2	Nanosheets	CVD	CH_4	500	$\sim70^b$	~50/~100 s	~100 ppm	262
VO_2					$\sim35^b$	—		
Pd/Ga_2O_3	Nanowires	Thermal evaporation	NO_2	100	41.44^b	200/70 s	~10 ppm	263
Ga_2O_3					0	—	—	
Pd/ZnO	Nanorods	Aqueous solution	H_2	1000	91.2^b	18.8/— s	0.2 ppm	264
ZnO					$\sim20^b$	—	—	
Pd/ZnO	Nanowires	CVD	H_2	4000	1017.9^b	36/50 s	20 ppm	265
Pd/ZnO	Nanowires	Electrochemical deposition	H_2	100	13 100	6.4/7.4 s	—	252
Pd/SnO_2	Nanofibers	Electrospun	H_2	1000	12.09	4/3 s	0.02 ppm	266
SnO_2					~3	2/— s		
Pt/SnO_2	Nanoparticles	Aqueous solution	H_2	1000	10 500	20/— s	—	249
SnO_2					0	—		
Pd/SnO_2	Nanoparticles	Thermal vaporization	H_2	10 000	$12 0000^b$	2/— s	40 ppm	253
Pd/TiO_2	Nanotubes	Sputtering	H_2	8000	92.05^b	3.8/43.3 s	—	255
TiO_2				5000	54.6^b	73.8/103.8 s		
Pt/TiO_2	Nanocomposites	Pressing and sintering	H_2	1000	6000	10/20 s	—	267
Pd/WO_3	Nanocomposites	Hydrothermal	H_2	1000	34	24/— s	—	268
WO_3	Nanoplates				~0	—		
Pt/Nb_2O_5	Porous ceramics	Pressing and sintering	H_2	10 000	165	7/39 s	200 ppm	269
Nb_2O_5					0	—	—	
Au/In_2O_3	Nanofibers	Electrospinning	Ethanol	100	11.12	47/351 s	20 ppm	270
In_2O_3					5.4	—	—	
Pt/In_2O_3	Nanocubes	Hydrothermal	H_2	15 000	~20	33/66 s	—	241

C = concentration; t_{res}/t_{rec} = response time/recovery time; LOD = limit of detection; response is defined as R_a/R_g (for reducing gases) or R_g/R_a (for oxidizing gases), R_a: resistance of the sensor exposed to the reference, R_g: resistance of the sensor exposed to the target. [a] Here the response is defined as $\Delta R/R_g$ (for reducing gases) or $\Delta R/R_a$ (for oxidizing gases), ΔR: the change in resistance. [b] Here the response is defined as $(\Delta R/R_g) \times 100\%$ (for reducing gases) or $(\Delta R/R_a) \times 100\%$ (for oxidizing gases).

fast response time of 2 s as shown in Fig. 15d. The Pd/SnO$_2$ nano-fibers[266] were also synthesized using an electrospinning method, and the sensor made of these nanofibers exhibits super-fast response/recovery times to H$_2$ (4/3 s to 1000 ppm H$_2$) and an ultra-low LOD of 20 ppb. The response of a sensor made of Pt/TiO$_2$ nanocomposites to 1000 ppm H$_2$ in N$_2$ was also reported as high as 6000 at RT, with short response/recovery times of only 10/20 s.[267]

Apart from the chemical sensitization and electronic sensi-tization, there are other mechanisms to enhance the sensing performance of the SMONs: for example, the formation of

nano-scale Schottky type junctions between Au nanoparticles and ZnO nanorods and Au sulfidation with high concentrations of H$_2$S.[257] Hosseini *et al.*[257] prepared ZnO nanorods using a vapor phase transport method, and found that H$_2$S sensing performance has been significantly enhanced at RT after the modification of the surface of ZnO nanorods with Au nano-particles (see Fig. 16a). As shown in Fig. 16b and c, both high response (1270 to 6 ppm of H$_2$S) and good H$_2$S selectivity of the Au/ZnO nanorods have been achieved, which are much better than those of the pristine ZnO nanorods.
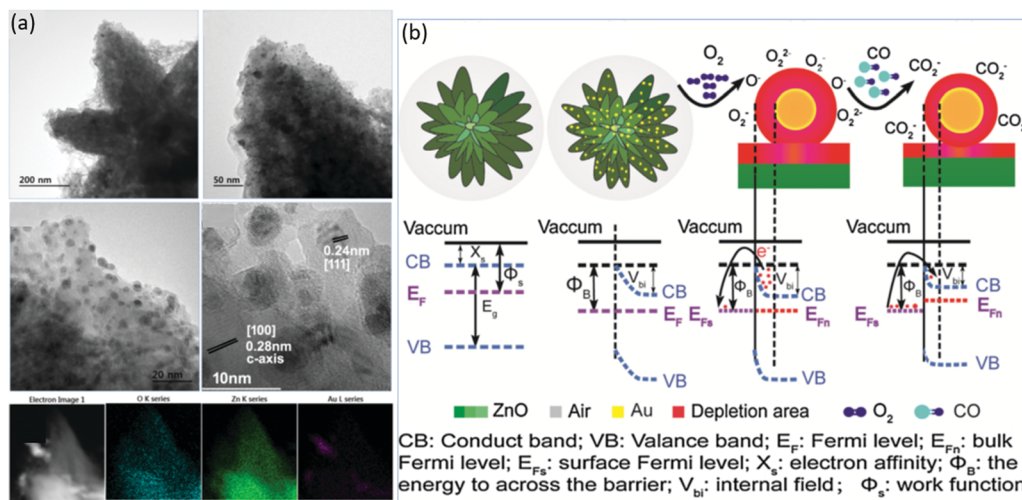
Fig. 14 (a) TEM images and element mapping of Au/ZnO nanostars; (b) energy band diagrams of ZnO and Au/ZnO nanostars before and after CO exposure.[113] Copyright 2017, Elsevier.
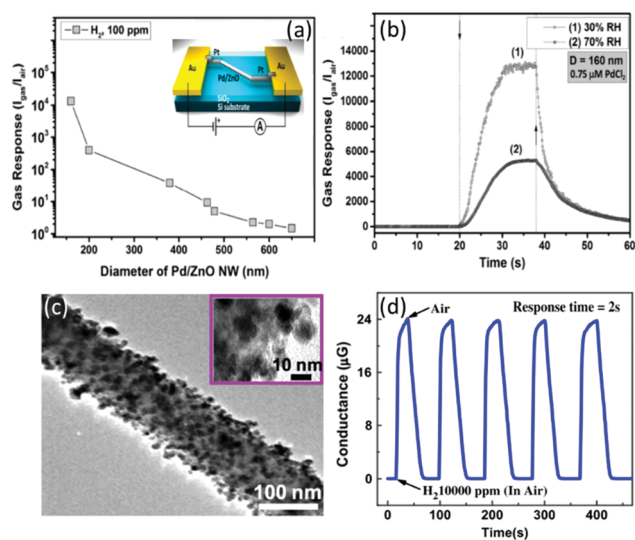

Fig. 15 (a) Responses of nanosensors based on single Pd/ZnO nanowires with different diameters to 100 ppm of H_2 at RT and 30% RH (the inset shows the schematic of the nanosensor device structure); (b) response of the Pd/ZnO nanowire based sensor to 100 ppm of H_2 at 30% and 70% RH at RT.[252] Copyright 2018, Elsevier. (c) TEM image of 30 at% Pd/SnO_2 nanofiber; (d) the response/recovery curves of the 30 at% Pd/SnO_2 nanofiber based sensor for H_2 gas.[253] Copyright 2010, Elsevier.

In summary, due to the combined effects of chemical sensitization and electronic sensitization, noble metal nanoparticles and other nanostructures are suitable to be used to modify the SMONs in order to improve the sensing performance of the RT gas sensors. One significant improvement is the shortening of the response and recovery times, along with the enhanced response values and selectivity.

3.1.2 Gas sensors based on conventional metal ion doped semiconducting metal oxide nanostructures. Doping of metal ions in SMONs can increase the number of active sites and defects on the surface of SMON nanocrystals, and thus enhance

the amount of oxygen species and increase the adsorbed gas molecules on the sensor's surface. Therefore, the gas sensing performance of the SMONs can be effectively improved by doping of metal ions including Al^{3+},[117,271] Cu^{2+},[272,273] Zn^{2+},[274] Ni^{2+},[275,276] Co^{3+},[277,278] Fe^{3+},[279] Mg^{2+}[280] and Sb^{5+}.[281] The recent key sensing applications of RT gas sensors using this method are summarized in Table 4.

The amount of dopant Al^{3+} ions was found to significantly affect the gas sensing properties of NiO nanosheets.[117] Al^{3+} doped NiO nanosheets have introduced many new oxygen vacancies due to aliovalent ion doping. Superoxide complexes such as Ni^{2+}–O_2^- are easily formed on the surface of the NiO due to the existence of oxygen vacancies. As they are very active, they can significantly increase the sensitivity of the NiO nanosheets. Compared with those of the pure NiO nanosheets, the response of the Al doped NiO nanosheet based sensor to NO_2 was enhanced up to 35 times at RT. Doping with metal ions including Sb, Cd, and Ce has also been proved to enhance the sensing properties of the WO_3 nanoparticles to NO_2 gas at RT.[209] Among these, Sb-doped WO_3 nanoparticles exhibit a 6.8 times higher response and much better selectivity than those of the undoped WO_3 (as shown in Fig. 17). The enhancement mechanisms have been identified to be the increase in the number of oxygen vacancies on the surface of metal doped WO_3 based on the analysis results from photoluminescence, Raman spectroscopy and XPS.[209]

The responses and recovery speeds of the sensor can be significantly improved by doping of metal ions into the SMONs, which is important for practical applications of the RT gas sensors. For example, a Zn-doped NiO dendritic nanostructure[119] exhibits faster responses (5–8 times) and faster recovery (30–50 times) rates than those of the pure NiO dendritic crystals. A sensor based on Mg-doped ZnO thin films on glass substrates deposited through a spray pyrolysis process[283] shows a much higher response (796 towards 100 ppm of NH_3) and faster response/recovery speeds (34/28 s) than those of the pure ZnO film measured at RT.
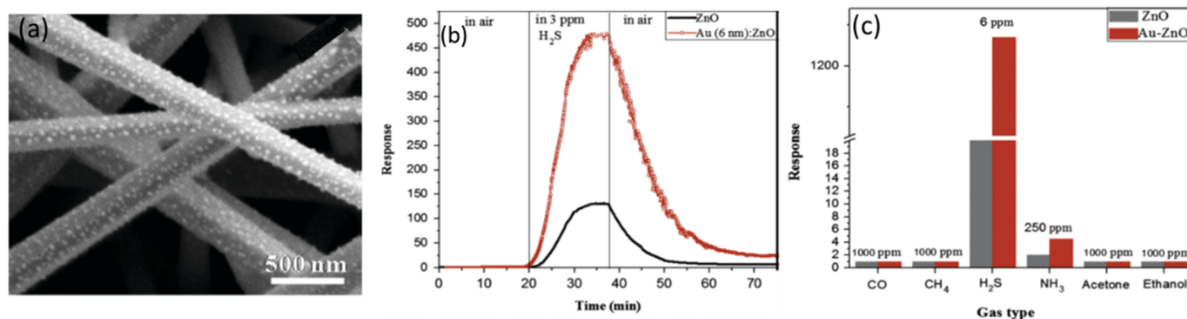
Fig. 16 (a) SEM image of Au/ZnO nanorods; (b) response/recovery curves of the Au/ZnO nanorod-based sensor and pristine ZnO nanorod-based sensor to 3 ppm H_2S at room temperature; (c) responses of the Au/ZnO nanorod-based sensor and pure ZnO nanorod-based sensor to different gases.[257] Copyright 2015, Elsevier.

Table 4 Summary of room temperature sensors made of metal ion doped semiconducting metal oxide nanostructures and their sensing properties

Material	Structure	Synthesis method	Target gas	C (ppm)	Response	t_{res}/t_{rec}	LOD	Ref.
Al/NiO	Nanosheets	Solvent-thermal	NO_2	10	2.77^a	50/200 s	250 ppb	117
Cu/Cu$_2$O	Hollow spheres	Hydrothermal	NO_2	10	6.27	34/— s	—	282
Sb/WO$_3$	Nanoparticles	Chemical solution	NO_2	10	51	$\sim$150/$\sim$200 s	$\sim$1 ppm	209
Zn/NiO	Dendritic crystals	Electrolytic	NH_3	30	0.2^a	5/30 s	5 ppm	119
Co/CuCo$_2$O$_4$	Nanoplatelets	Hydrothermal	NH_3	400	7.9^b	—/14 min	$\sim$25 ppm	273
Cu/ZnO	Nanorods	Hydrothermal	NH_3	20	31.1^b	15/48 s	$\sim$10 ppm	118
Ce$_{0.94}$Zr$_{0.06}$O$_2$	Nanosheets	Sol-hydrothermal	NH_3	100	87	—	100 ppb	127
Mg/ZnO	Thin films	Spray pyrolysis	NH_3	100	769	34/28 s	$\sim$1 ppm	283
Sb/SnO$_2$	Nanoparticles	Sol–gel	NH_3	50	4316^b	70/— s	—	284
SnO$_2$:Sb	Nanowires	CVD	Ethanol	300	1.3	10/87 s	40 ppm	285
Al/ZnO	Nanowires	Electrodeposition	Ethanol	1000	1.7	10/30 s	—	286
Al/ZnO	Hexagonal facets	Sol–gel	Ethanol	300	94^b	68/50 s	—	271
Co/TiO$_2$	Nanoparticles	Sol–gel	Ethanol	500	$\sim$105^b	—	—	277
Fe/WO$_3$	Microspheres	Spray pyrolysis	Ethanol	400	$\sim$140	$\sim$10/$\sim$40 s	$\sim$100 ppm	279
Ni/ZnO	Nanorods	Electrodeposition	Acetone	100	1.6	—	—	275
Na/ZnO	Nanoflowers	Solution route	Acetone	100	3.35	18/63 s	0.2 ppm	287
Mg/ZnO	Nanorods	Frequency sputtering	H_2	200	30	85/70 s	—	288
Nb/TiO$_2$	Nanotubes	Annealing	H_2	1000	30.9^b	100/— s	—	289
Mg/ZnO	Film	Rf sputtering	H_2	200	35–40	75/54 s	—	280
Cd/ZnO	Nanowires	Electrodeposition	H_2	100	274^b	14/11 s	—	89
Co/TiO$_2$	Mesoporous	Self-assembly	H_2	1000	4082	66/— s	50 ppm	278
Sb/SnO$_2$	Nanoribbons	Thermal evaporation	H_2S	100	$\sim$18	$\sim$500/$\sim$500 s	100 ppb	281
Zn/ZnO	Nanotetrapods	Thermal evaporation	H_2S	4	38^b	$\sim$200/$\sim$1000 s	1 ppm	290
Zn/In$_2$O$_3$	Nanowires	CVD	CO	5	$\sim$57^b	20/10 s	$\sim$1 ppm	274
Sb/SnO$_2$	Nanoporous films	Sol–gel	Cl_2	3	500^a	60/120 s	$\sim$1 ppm	291

C = concentration; t_{res}/t_{rec} = response time/recovery time; LOD = limit of detection; response is defined as R_a/R_g (for reducing gases) or R_g/R_a (for oxidizing gases), R_a: resistance of the sensor exposed to the reference, R_g: resistance of the sensor exposed to the target.^{a} Here the response is defined as $\Delta R/R_g$ (for reducing gases) or $\Delta R/R_a$ (for oxidizing gases), ΔR: the change in resistance. ^{b} Here the response is defined as $(\Delta R/R_g) \times 100\%$ (for reducing gases) or $(\Delta R/R_a) \times 100\%$ (for oxidizing gases).

The sensor based on Sb doped SnO$_2$ nanowires prepared using a chemical vapor deposition (CVD) method[285] shows a typical p-type behavior, and a fast response time of about 10 s to 300 ppm ethanol at RT.

Adsorption of water vapor on the SMON surfaces is sometimes enhanced by metal ion doping, which seems a bad news for a gas sensor. However, for RT NH$_3$ gas sensors, this is especially beneficial as the NH$_3$ molecules react with the absorbed H$_2$O to form the NH$_4^+$ and OH$^-$ as is schematically shown in Fig. 18a. The electrolytic conductivity of NH$_4^+$ and OH$^-$ can significantly improve the sensitivity of sensors at RT.[127,198] Porous Ce$_{0.94}$Zr$_{0.06}$O$_2$ nano-sheets (see Fig. 18b) with an average thickness of 8 nm were prepared using a sol-hydrothermal process.[127] Doping of Zr^{4+} ions into the CeO$_2$ nanosheets enlarges the specific surface

areas (185.4 m^2 g^{-1}) and increases the pore volumes (0.51 cm^3 g^{-1}). These modifications result in a much higher sensitivity (e.g. 87 to 100 ppm NH$_3$) at RT (see Fig. 18c), better selectivity and a very low LOD of 100 ppb.

The H$_2$ sensors made of metal ion doped SMONs were reported to exhibit high responses, although their response/recovery times were also reported to be longer than those made of the noble ion modified SMON-based RT H$_2$ gas sensors.[278,280,288,289] For example, Co-doped TiO$_2$ sensors exhibit an ultra-high response with a value of 4082 to 1000 ppm H$_2$ gas, although the response time is 66 s, which is quite slow for detection of highly explosive H$_2$.[278]

In summary, compared to those sensors made of noble metal nanoparticle modified SMONs, the improved effects of gas sensors made of the metal ion modified SMONs are not as significant.
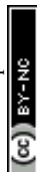
Fig. 17 (a) Responses of sensors made of 2%-Sb-WO$_3$, 2%-Ce-WO$_3$ and 2%-Cd-WO$_3$ to different concentrations of NO$_2$; (b) responses of sensors made of 2%-Sb-WO$_3$ to different gases.[209] Copyright 2017, American Chemical Society.
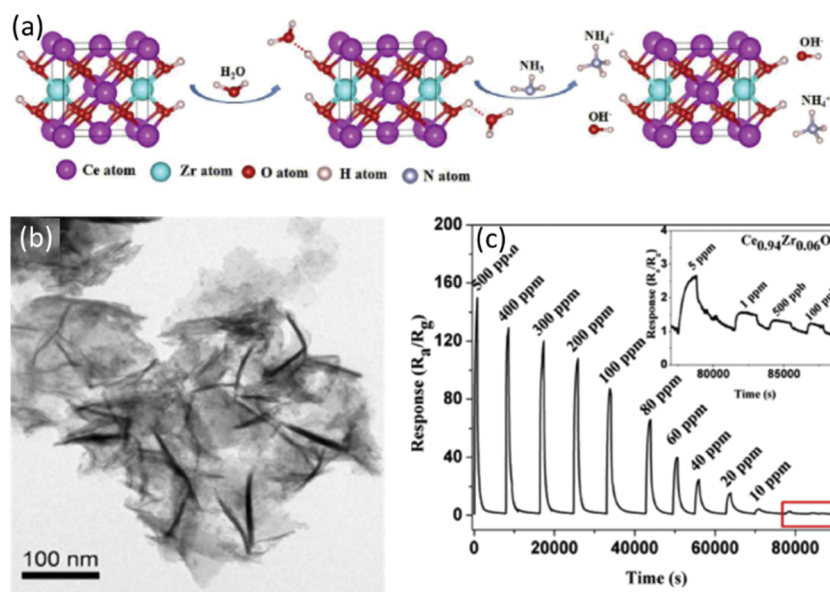

Fig. 18 (a) Schematic diagrams of the NH$_3$ reaction mechanism on the surface of Ce$_{0.94}$Zr$_{0.06}$O$_2$ nano-sheets; (b) TEM image of porous Ce$_{0.94}$Zr$_{0.06}$O$_2$ nano-sheets; (c) response/recovery curves of the porous Ce$_{0.94}$Zr$_{0.06}$O$_2$ nanosheet based sensor to NH$_3$.[127] Copyright 2018, Elsevier.

However, the SMONs can be modified simultaneously by both metal ions and noble metal nanoparticles, which will combine the advantages of both metal ions and noble metal nanoparticles.

3.2 Composites of semiconducting metal oxide nanostructures and gas sensors

3.2.1 Mechanism for enhanced sensing performance. The RT gas sensing performance of the SMONs operated at RT can be improved by integrating them with other metal oxides or carbon nanomaterials. For example, heterojunctions can be formed at the interfaces of different metal oxides or at the interfaces between SMONs and carbon nanomaterials, as schematically illustrated in Fig. 19. At the p–n heterojunctions between p-type and n-type SMONs, the electrons at the conduction band states of n-type SMONs will transfer to the lower energy valence band states of p-type SMONs across the interface. Thus, a depletion layer will form at the p–n heterojunction due to recombination of electrons and holes.

For the n–n heterojunction, the electrons will be transported at the interfaces between different materials due to the differences in their conduction band states. As a result, a depletion layer forms at the surface of n-type SMONs with higher-energy conduction band states due to the loss of electrons. At the same time, an accumulation layer forms at the surface of n-type SMONs with lower-energy conduction band states due to the accumulation of electrons.

For the p–p heterojunction, the major charge carriers are holes. Due to the differences of valence band energies of different SMONs, the charge carriers are transported from one p-type SMON (which has a higher energy valence band state) to the other p-type SMON (which has a lower-energy valence band state). Therefore, a hole depletion region is formed at the surface of the first SMONs (with higher energy valence band state) and a hole accumulation region is formed at the surface of the second SMONs (with a lower energy valance band state) as shown in Fig. 19.
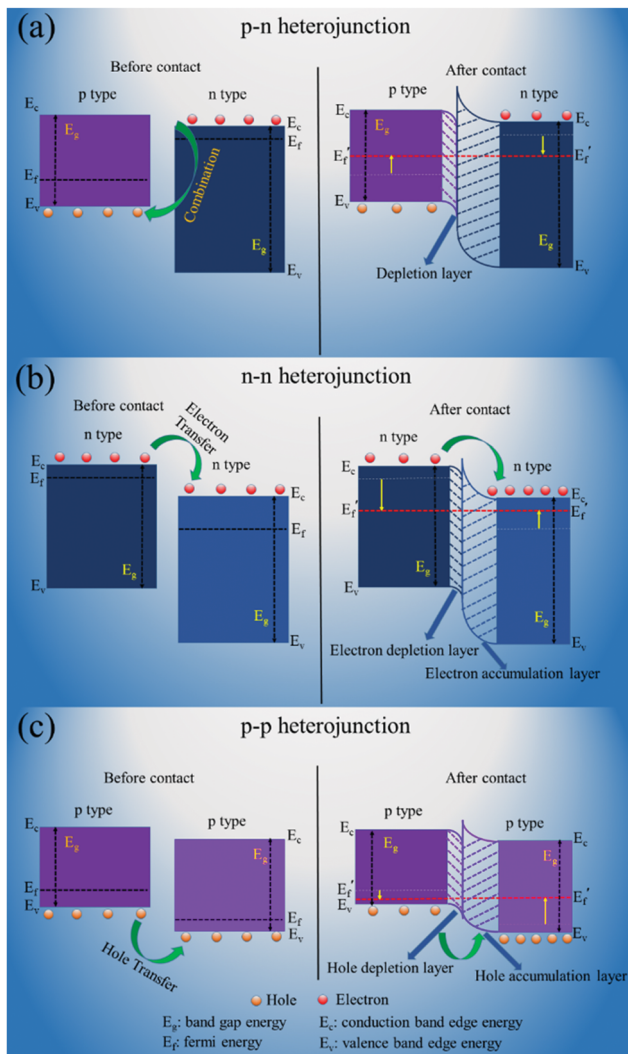
Fig. 19 Schematic illustrations of the energy band structures at heterojunction interfaces of different types of heterojunctions: (a) p–n junction, (b) n–n junction and (c) p–p junction.

These formed heterojunctions can effectively accelerate the transport of electrons. On the other hand, these heterojunctions can also enhance oxygen adsorption, therefore, abundant oxygen vacancies are formed on the surfaces of the SMON composites, which can provide new active sites for sensing reactions. In addition, the composites of SMONs often contain numerous mesopores, which are beneficial to the adsorption and desorption of gas molecules. All of these effects will improve the sensitivity and response rates of the RT gas sensors made of composites of the SMONs.

3.2.2 Gas sensors based on composites of semiconducting metal oxide nanostructures and other metal oxides. Composite oxides of the SMONs have been proposed to combine two or more semiconducting metal oxides together to enhance the gas sensing performance at RT. The examples of composites include n-type SMONs with n-type SMONs (*e.g.* Fe_2O_3/ZnO,[292] ZnO/SnO_2,[293] In_2O_3/SnO_2[134,294]), p-type SMONs with n-type SMONs (*e.g.* NiO–ZnO,[120] CuO/TiO_2,[121] In_2O_3/CuO,[122] NiO/WO_3[295])

and p-type SMONs with p-type SMONs (*e.g.* Cu_2O/Co_3O_4[296] and NiO/CuO[131]). In addition, composites formed by integrating the SMONs with non-semiconductor metal oxide (*e.g.* K_2O/In_2O_3[129] and CaO/SnO_2[297]) have also been reported.

Table 5 summarizes the recently reported RT gas sensors made of composite oxides of the SMONs and/or other metal oxides. For these composite oxides, a number of oxygen vacancies are formed on both the surfaces and interfaces, which provides many active sites for the gas sensing reactions. Plenty of defects will also be formed at the interfaces of nanostructures in different metal oxide nanoparticles. In addition, the heterojunctions are usually formed at the interfaces of different metal oxides, which can effectively accelerate the electron transfer between different particles, thus accelerating the response speed of the sensor. Besides, the composite oxides often contain lots of mesoporous structures due to the accumulation of nanoparticles, which are beneficial to the adsorption and desorption of gas molecules. These factors can improve the sensing performance of the sensor made of these composite oxides, especially for the sensitivity and response speed. Most sensors made of the composite oxides exhibit very fast response times at RT. For example, the gas sensor based on the nanocomposite of CuO/TiO_2[121] shows a very fast response time of 2 s at RT, and the sensor based on plate-like NiO/WO_3 nanocomposites[295] exhibits excellent sensitivity and ultrafast response/recovery times (2.5/1.1 s) to NO_2 at RT.

The composite of mesoporous In_2O_3/CuO multijunction nanofibers[122] was prepared using an electrospinning method by Zhou *et al.* The composite is composed of the In_2O_3 nanoparticles and CuO nanoparticles (with a molar ratio of Cu : In of 100 : 5). The TEM images shown in Fig. 20a and b indicate that the composite has many mesoporous structures with diameters from 1.9 to 22.9 nm and large specific surface areas (48.7 m^2 g^{-1}). The In_2O_3 nanoparticles are surrounded by the CuO nanoparticles to form numerous p–p homojunctions and p–n heterojunctions.[122] XPS analysis indicates that the ratio of oxygen defect/vacancy on its surface is as high as 45.4%. Due to the existence of larger specific and mesoporous surface areas and the availability of chemisorbed oxygen and the formation of heterojunctions, the sensor has a much higher response to NH_3 than that of a CuO nanostructured sensor. The response time is also very short with a value lower than 8 s for NH_3 from 0.3 to 100 ppm (see Fig. 20c). The selectivity and LOD are also significantly improved due to the addition of In_2O_3.

Xu *et al.*[134] prepared composites of In_2O_3/SnO_2 nanorod heterostructures (see Fig. 20d and e) using electrospinning to improve the oxygen deficiency and carrier density of SnO_2. The SnO_2 nanoparticles are distributed along with the In_2O_3 to form numerous heterojunctions and defects at their interfaces. The availability of oxygen vacancies on the surface and at the interface has been verified using XPS.[134] Compared with pure SnO_2 nanorods, In_2O_3/SnO_2 nanorods (with the atom ratio of 25 : 0.3 of Sn : In) exhibit 11 times higher response to NO_x with a very faster response time of 4.67 s and a lower LOD with a value of 0.1 ppm (see Fig. 20f).

NiO/CuO nanocomposites with a NiO : CuO molar ratio of 1 : 1 have been synthesized using a hydrothermal method,[131]

Table 5 Room temperature sensing properties of composites of semiconducting metal oxide nanostructures and other metal oxides

Material	Structure	Synthesis method	Target gas	C (ppm)	Response	t_{res}/t_{rec}	LOD	Ref.
ZnO/SnO_2	Thin films	Hydrothermal	NH_3	20	1.1	300/— s	5 ppm	293
In_2O_3/CuO	Nanofibers	Electrospinning	NH_3	100	1.9^a	2/— s	0.3 ppm	122
Cr_2O_3/ZnO	Thick films	Screen-printing	NH_3	300	13.7^a	25/75 s	—	298
NiO/ZnO	Nanocones	Hydrothermal	NH_3	50	42^b	27/150 s	$\sim$15 ppm	120
CuO/TiO_2	Nanoparticles	Sol–gel	NH_3	50	97^b	2/55 s	$\sim$5 ppm	121
CuO/MNO_2	Flowers/sheets	Hydrothermal	NH_3	100	135^b	120/600 s	20 ppm	299
$Silica/CeO_2$	Nanoparticles	Hydrothermal	NH_3	80	3244^b	750/— s	0.5 ppm	198
Fe_2O_3/ZnO	Nanorods	Sol–gel	NH_3	0.4	10 000	20/20 s	—	292
NiO/WO_3	Plates	Annealing	NO_2	30	4.8	2.5/1.1 s	5 ppm	295
NiO/SnO_2	Nanosheets	Annealing	NO_2	60	$\sim 7.5^a$	—	$\sim$5 ppm	300
NiO/CuO	Flower-like	Hydrothermal	NO_2	100	77.16^b	2 s/—	1 ppm	131
CaO/SnO_2	Rod-like	Electrospinning	NO_x	97	6.63^a	—	10 ppb	297
In_2O_3/SnO_2	Nanorods	Electrospinning	NO_x	100	8.98^a	4.67/— s	0.1 ppm	134
In_2O_3/TiO_2	Nanofibers	Electrospinning	NO_x	97	41.1^b	3/— s	97 ppb	301
Al_2O_3/TiO_2	Nanotubes	Induction	NO_x	97	88.04^b	$\sim$8/$\sim$8 s	0.97 ppm	302
K_2O/In_2O_3	Nanowires	Template	NO_x	97	151.78^a	12/— s	48.5 ppb	129
NiO/In_2O_3	Nanofibers	Electrospinning	H_2S	3	6	14/22 s	3 ppm	303
CuO/ZnO	Nanorods	Pulsed laser deposition	H_2S	0.5	25^b	180/15 s	$\sim$0.5 ppm	304
SnO_2/NiO	Thin films	RF sputtering	H_2S	10	440	—	100 ppb	123
In_2O_3/ZnO	Core–shells	Hydrothermal	H_2S	700	925^b	—	20 ppm	305
Cu_2O/Co_3O_4	Heteroarrays	Electrodeposition	H_2S	20	$\sim$2600	$\sim$100/$\sim$100 s	$\sim$0.1 ppm	296
SnO_2/CuO	Heterojunctions	Screen printing	H_2S	1	3672^a	15/— s	10 ppm	306
NiO/Nb_2O_5	Nanoparticles	Hydrothermal	H_2	500	1.68	100.42/524.84 s	—	307
Cr_2O_3/Nb_2O_5	Nanoparticles	Hydrothermal	H_2	200	5.24	40/— s	—	308
ZnO/CuO	Nanoparticles	Hydrothermal	Alcohol	20	3.32	62/83 s	$\sim$150 ppm	309
VO_2/ZnO	Heteronanostructures	Heteroepitaxial	Acetone	100	4.51	8/18 s	$\sim$10 ppm	310
ZnO/SnO_2	Heterojunctions	Hydrothermal	Ozone	0.06	12	13/90 s	20 ppb	311
CuO/ZnO	Thick film	Screen-printing	Cl_2	300	195^a	18/50 s	—	312
α-Fe_2O_3/ZnO	Nanowires	Piezo-surface coupling	Ethanol	700	706.8^b	—	$\sim$100 ppm	313

C = concentration; t_{res}/t_{rec} = response time/recovery time; LOD = limit of detection; response is defined as R_a/R_g (for reducing gases) or R_g/R_a (for oxidizing gases), R_a: resistance of the sensor exposed to reference, R_g: resistance of the sensor exposed to target.^{a} Here the response is defined as $\Delta R/R_g$ (for reducing gases) or $\Delta R/R_a$ (for oxidizing gases), ΔR: the change in resistance. ^{b} Here the response is defined as $(\Delta R/R_g) \times 100\%$ (for reducing gases) or $(\Delta R/R_a) \times 100\%$ (for oxidizing gases).

and the nanocomposites are consisted of CuO nanoparticles and NiO nanoplates with lots of mesoporous structures. The p–p heterojunctions formed at the interfaces of NiO and CuO accelerate the electron transfers from NiO to CuO, thus resulting in a faster response. The mesoporous hierarchical nanostructures with much larger surface areas facilitate effective adsorption and desorption of gas molecules on the surface. Thus, the sensor exhibits an ultra-fast response speed (2 s to 100 ppm NO_2) to NO_2 at RT.

Kaur et al.[123] prepared a SnO_2/NiO thin film using a sputtering method and then fabricated a RT H_2S sensor. As shown in Fig. 21a, the sensor exhibits a high response with a value of 440 to 10 ppm H_2S, which is 9 and 415 times higher than those made of pure SnO_2 and NiO films, respectively. Selectivity has also been improved using the SnO_2/NiO thin film (see Fig. 21b). The formation of p–n heterojunctions using the p-type NiO and n-type SnO_2 semiconductors apparently changes the resistance of the composite film. The enhanced response of the SnO_2:NiO nanocomposite sensor is mainly due to the modifications of p–n junctions resulted from the conversion of NiO to metallic NiS. However, the recovery time is quite long ($>$20 000 s, see Fig. 21c).

Wang et al.[198] reported a composite oxide sensor using 8% silica modified CeO_2 nanomaterials (see Fig. 21d) synthesized using a sol-hydrothermal route. The addition of silica increases the specific surface areas (83.75 m^2 g^{-1}) and decreases the crystal sizes. Due to the existence of silica, lots of OH^- species are formed on the surface of the sensor, which facilitate the adsorption of water, and the water molecules react with NH_3 to generate NH^{4+} and OH^- and decrease the electrical resistance of the sensor. As shown in Fig. 21e and f, the NH_3 gas sensing performance of the sensor is significantly enhanced as compared to that of pure CeO_2 at RT. Its response value reaches 3244% (defined as $(\Delta R/R_g) \times 100\%$) for 80 ppm of NH_3 gas.

The composites of alkali metal oxide and SMONs have also been reported as an effective way to enhance the sensitivity for sensing acidic gases, such as NO_x.[129] As shown in the gas sensing mechanism of mesoporous K_2O–In_2O_3 nanowires in Fig. 22 the alkali metal oxides on the surfaces can serve as the alkaline center, which is beneficial to the adsorption and diffusion of acidic gases. Using mesoporous Santa Barbara Amorphous Material-16 (SBA-16) as a template, Rehman et al.[129] prepared highly crystalline mesoporous K_2O–In_2O_3 nanowires with diameters of 4–8 nm and pore sizes of 3–5 nm. The composite nanowires possess numerous chemisorbed oxygen and alkaline centers on their surfaces. The gas sensing performance of the mesoporous K_2O–In_2O_3 composite nanowires has been significantly improved with the addition of K_2O. Its response is 151.78 to 97 ppm of NO_x, the response time is decreased to 12 s, and the LOD is as low as 48.5 ppb at RT.[129]

Most reported composite SMON sensors exhibit higher response values and faster response time than those of the single phase SMONs. Many active sites can be generated in the

Fig. 20 (a) TEM and (b) HRTEM images of mesoporous In_2O_3/CuO composite multijunction nanofibers, (c) response values and times of the sensor to different concentrations of NH_3.[122] Copyright 2018, Elsevier. (d and e) TEM images of composite of In_2O_3/SnO_2 nanorod heterostructures; (f) response/recovery curves of the sensor to different concentrations of NO_x.[134] Copyright 2015, Royal Society of Chemistry.
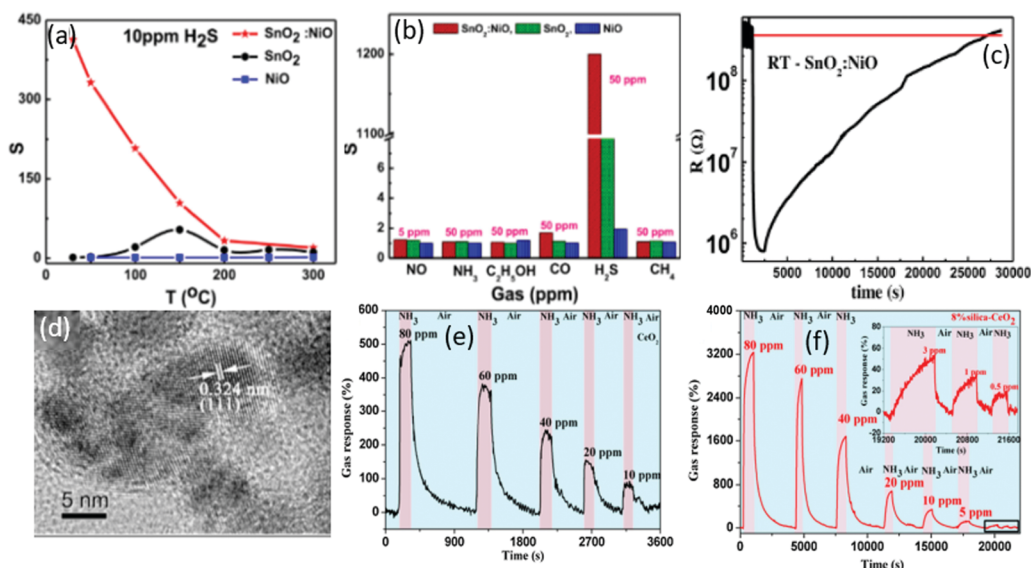

Fig. 21 (a) Response histogram of a SnO_2/NiO thin film-based room temperature gas sensor to different gases; (b) response values of the SnO_2/NiO thin film-based RT gas sensor to different concentrations of H_2S; (c) response/recovery curve to 100 ppm H_2S.[123] Copyright 2017, Elsevier. (d) TEM image of 8% silica-CeO_2; (e) response/recovery curves of the pure CeO_2-based sensor to NH_3; (f) response/recovery curves of the 8% silica-CeO_2-based sensor to NH_3.[198] Copyright 2017, Elsevier.

composite SMONs, such as oxygen vacancies, heterojunctions, defects and mesopores, which can effectively enhance the sensing performance. The composite SMON can be further modified by noble metal nanoparticles, which takes advantage of the chemical sensitization and electronic sensitization of noble metal nanoparticles on the composite SMONs.

3.2.3 Gas sensors based on composites of semiconducting metal oxide nanostructures and carbon nanomaterials. Carbon nanomaterials including carbon nanotubes and graphene

have been demonstrated as promising sensing materials.[314] However, the carbon nanomaterial-based gas sensors generally show low sensitivity and slow response/recovery speeds at RT. The synergistic effect by combining SMONs and carbon nanomaterials can improve the sensing performance because (1) conductivity is significantly improved; (2) many active sites (such as oxygen functional groups, vacancies and defects) are formed at the interfaces. Because of the fast carrier transport kinetics, the composites of the SMONs combined with carbon
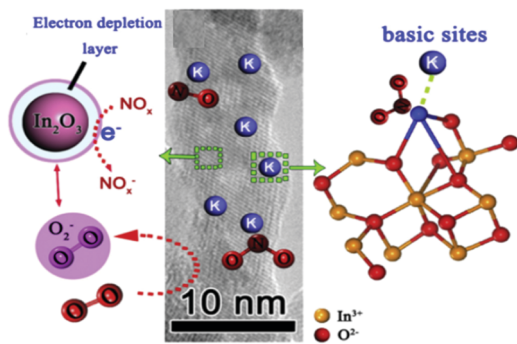
Fig. 22 Gas sensing mechanism to NO_x of mesoporous $K_2O–In_2O_3$ nanowires.[129] Copyright 2016, Elsevier.

nanomaterials show enhanced sensitivity and fast response/recovery at RT.

Table 6 summarizes the RT sensing properties of some composite nanostructures of the SMONs and carbon nanomaterials. Among these carbon materials, the composites of reduced graphene oxide (rGO) and SMONs are the most investigated ones for gas sensor applications. rGO has been used to combine with various types of SMONs for enhancing the gas sensing properties, and these SMONs include Fe_2O_3,[315] In_2O_3,[316] ZnO,[317,318] Fe_3O_4,[319] SnO_2,[320–324] WO_3,[325] NiO/SnO_2[326] and Pd/TiO_2.[327]

The RT NO_2 sensor fabricated using rGO/α-Fe_2O_3[126] exhibits a response value of 3.86 to 5 ppm NO_2, which is better than that of pure rGO, whose response is 1.38. In addition, it has significantly shorter response/recovery times of 32/1432 s, compared with those of the sensors made of pure rGO (2059 s, 40130 s). Dong et al.[342] reported a nanocomposite combining α-Fe_2O_3 nanospheres and reduced graphene oxide nanosheets as shown in Fig. 23a. The α-Fe_2O_3 nanospheres with a diameter from 40 to 50 nm were grown on the surface of graphene nanosheets using a hydrothermal method, and the improved sensing performance of the sensor made of this composite was attributed to the synergistic effect of a-Fe_2O_3/rGO and large specific surface areas. In addition to the interaction of NO_2 with O_2^- on the surface of a-Fe_2O_3, NO_2 molecules also capture the electrons from the rGO to form NO_2^-, thus resulting in an increased hole density, and a decreased resistance of rGO. Therefore, the a-Fe_2O_3/rGO nanocomposites exhibit a much higher response to NO_2 at RT than that of either the pure rGO or a-Fe_2O_3 nanospheres. Its LOD for the NO_2 gas is as low as 0.18 ppm (see Fig. 23b), and good selectivity has been demonstrated against CO, HCHO, H_2S, NH_3 and C_2H_5OH (see Fig. 23c).

Besides the good conductivity of carbon materials, the improved interfacial electron transfer is another key factor for improving the SMONs' sensing performance by adding carbon nanomaterials. For example, an RT NH_3 gas sensor was fabricated using SnO_2 nanorods/rGO composite nanostructures,[347] and the sensor shows fast response/recovery with times of 8/13 s to 200 ppm NH_3 at RT. Fig. 23d shows the band gap diagrams of SnO_2-nanorods/rGO nanostructures before and after the combination of two nanostructures. The p–n heterojunctions are formed at the interface between the rGO and SnO_2 as rGO is a

p-type semiconductor. The Fermi energy of rGO is higher than that of SnO_2, so electrons can be transported to SnO_2 from rGO, which can further enhance the adsorption of NH_3 molecules to improve the gas sensing performance.

Formation of heterojunction structures was found to contribute to the sensing performance of the ZnO nanowall/rGO nanocomposite,[135] in which the ZnO nanowalls were vertically grown on the rGO thin film using a soft solution process to obtain a heterojunction structure as shown in Fig. 23e. At the interfaces between the rGO and ZnO nanowalls of the p–n heterostructures, the Fermi energy of rGO is higher than that of ZnO. Therefore, the charge transfer from rGO layers to the conduction band of ZnO enhances the adsorption of NO_2 molecules. If compared with the sensor made of pure ZnO nanowalls, the sensor made of the ZnO/rGO heterojunction shows a higher response and shorter response/recovery times to NO_2 at RT (see Fig. 23f).[135]

Another key mechanism for the improved gas sensing performance for the SMONs/rGO composite is the increased oxygen vacancy on the SMONs, such as in the SnO_2–rGO composite.[330] Due to the p–n heterojunction formed at the interfaces between n-type SnO_2 and p-type rGO, electrons can easily transfer from the SnO_2 into the rGO to form abundant oxygen vacancies on the surface of SnO_2. These oxygen vacancies are the electronic charge carriers to increase the conductivity of the composite, and they can adsorb oxygen molecules to form more active sites, which will capture electrons from SnO_2 and form the oxygen ions to react with target gas molecules. The oxygen vacancy also facilitates the fast adsorption of the NO_2 molecules onto the surface of SnO_2. All these factors contribute to the excellent sensing properties of SnO_2/rGO composite based sensors to NO_2 gas at RT.

However, the recovery of these composites of SMONs with carbon materials is very slow, although UV-light illumination can be used to enhance a fast and complete recovery. For example, rGO-CeO_2 hybrids were synthesized by anchoring small CeO_2 nanocrystals onto rGO nanosheets using a solvothermal method, and the RT NO_2 gas sensor made of this hybrid showed a full recovery time of several hours.[371] However, the recovery time can be significantly reduced to within 258 s with the aid of UV-light illumination. This UV light enhancement will be further discussed in Section 3.3.

Fig. 24a shows that an ultra-fast response time for sensing of H_2S gas (which is the fastest reported in the literature with a value of 2s to 50 ppm of H_2S) can be achieved using a sensor made of SnO_2 quantum wires/rGO nanosheets.[4] The electronic interactions of SnO_2 quantum wires and rGO nanosheets can enhance the electron transport,[4] and increase the response and recovery speed. In addition, the sensor made of the SnO_2 quantum wires/rGO nanosheets shows a response of 33 with an excellent selectivity against other types of gases including NH_3, SO_2, NO_2 and ethanol at RT as shown in Fig. 24b. In this composite material, the ultrathin and one-dimensional microstructure of SnO_2 quantum wires is effective in providing large surface areas for gas adsorption and reactions.

The sensors made of composites integrating the rGO with p-type SMONs (such as CuO and Co_3O_4) also show enhanced sensing performance. The RT gas sensor based on the CuO/rGO

Table 6 Room temperature sensing properties of composite nanostructures of semiconducting metal oxide nanostructures and carbon nanomaterials

Material	Structure of SMONs	Synthesis method of SMONs	Target gas	C (ppm)	Response	t_{res}/t_{rec}	LOD	Ref.
NiO/rGO	Nanosheets	Hydrothermal	NO$_2$	0.25	0.04^a	576/121 s	∼0.25 ppm	328
WO$_3$/MWCNTs	Nanoparticles	Metal organic decomposition	NO$_2$	0.1	0.25^a	10.5/20 min	100 ppb	125
Ag/SnO$_2$/rGO	Nanoparticles	Hydrothermal	NO$_2$	5	2.17	49/339 s	1 ppm	329
SnO$_2$/rGO	Nanoparticles	Hydrothermal	NO$_2$	1	3.8	14/190 s	50 ppb	330
α-Fe$_2$O$_3$/rGO	Nanoparticles	Hydrothermal	NO$_2$	5	3.86	76/946 s	0.1 ppm	126
Cu$_2$O/rGO	Nanoparticles	Chemical solution	NO$_2$	1	5.2	29.2/76.8 s	100 ppb	331
ZnO/graphene	Spheres	Solvothermal	NO$_2$	50	8^b	132/164 s	∼10 ppm	332
Co$_3$O$_4$/rGO	Thin sheets	Hydrothermal	NO$_2$	800	∼8^b	1.5/1 min	60 ppm	333
In$_2$O$_3$/rGO	Nanosheets	Hydrothermal	NO$_2$	30	8.25	4/24 min	∼5 ppm	334
SnO$_2$/graphene	Nanoparticles	Sol–gel	NO$_2$	20	∼9.5	<1/5 min	5 ppm	124
ZnO/rGO	Nanowalls	Solution	NO$_2$	50	9.61	25/15 s	∼5 ppm	135
CuO/rGO	Nanosheets	Chemical solution	NO$_2$	1	14	66/34 s	60 ppb	335
SnO$_2$/S/rGO	Nanoparticles	Hydrothermal	NO$_2$	5	20.31^b	40 s/357 s	1ppm	336
CeO$_2$/rGO	Bilayer	Spray	NO$_2$	10	20.5^b	92/— s	∼1 ppm	337
SnO$_2$/rGO	Nanoparticles	Hydrothermal	NO$_2$	1000	22.87^b	100/— s	1 ppm	338
Fe$_3$O$_4$/graphene	Nanoparticles	Hydrothermal	NO$_2$	400	24.2^b	275/738 s	∼30 ppm	339
ZnO/rGO	Nanorods	Oriented growth	NO$_2$	1	119^b	75/132 s	50 ppb	340
WO$_3$/S/rGO	Nanorods	Hydrothermal	NO$_2$	20	149.5^b	6 s/56 s	0.25 ppm	341
α-Fe$_2$O$_3$/rGO	Nanospheres	Hydrothermal	NO$_2$	90	150.63^b	–/1648 s	0.18 ppm	342
In$_2$O$_3$/rGO	Layers	Reflux	NO$_x$	97	1.45^a	25/— s	970 ppb	343
CeO$_2$/graphene	Nanosheets	Solvothermal	NO$_x$	300	12.76^b	1.3/— s	5 ppm	344
Cu$_x$O/graphene	Nanoflowers	Reflux	NO$_x$	97	95.1^b	9.6/— s	97 ppb	345
VO$_2$/CNT	Nanocomposites	Hydrothermal	NH$_3$	45	0.04^a	290/1800 s	20 ppb	346
SnO$_2$/rGO	Nanorods	Hydrothermal	NH$_3$	200	1.3	8/13 s	20 ppm	347
Cu$_2$O/rGO	Nanorods	Hydrothermal	NH$_3$	200	2.04	28/206 s	∼100 ppm	348
TiO$_2$/rGO	Microspheres	Hydrothermal	NH$_3$	30	∼3.5^b	∼10/∼10 min	5 ppm	349
Pd/SnO$_2$/rGO	Nanoparticles	Chemical solution	NH$_3$	5	7.6^b	7 min/50 min	∼5 ppm	350
Pd/TiO$_2$/rGO	Nanorods	One-pot polyol	NH$_3$	50	14.9^b	184 s/81 s	2.4 ppm	351
ZnO/GrO	Nanosheets	Chemical solution	NH$_3$	1	24^b	6/2–3 s	1 ppm	352
SnO$_2$/MWCNTs	Nanocomposites	Microelectronic	NH$_3$	200	26	<5/5 min	∼40 ppm	136
SnO/graphene	Hybrid films	CVD	NH$_3$	100	35^b	∼10/— s	∼5 ppm	353
ZnO/CNT	Networks	Flame	NH$_3$	100	330	18.4/35 s	200 ppb	354
SnO$_2$/MWCNT	Nanofibers	Electrospinning	CO	50	1.29	—	47 ppm	355
CuO/rGO	Nanocomposites	Hydrothermal	CO	1	2.56^b	70/160 s	0.25 ppm	356
Pd/SnO$_2$/rGO	Nanoparticles	Hydrothermal	CO	1600	9.5^b	2 min/2 min	∼50 ppm	357
Au/SnO$_2$/CNT	Nanotubes	Chemical solution	CO	2500	70	—	—	358
SnO$_2$/F-MWCNTs	Networks	Sputtering	H$_2$	500	5.4^b	—/9 s	—	359
CuO/rGO/CuO	Sandwich	Hydrothermal	H$_2$	1500	∼12^b	80/60 s	10 ppm	360
ZnO/graphene	Nanotubes	Hydrothermal	H$_2$	100	28.08^b	30/∼150 s	10 ppm	361
Pd/SnO$_2$/rGO	Nanoparticles	Chemical solution	H$_2$	10000	50^b	—	100 ppm	362
TiO$_2$/rGO	Nanosheets	Spray method	HCOH	0.5	0.4^b	70/126 s	∼0.1 ppm	363
SnO$_2$/graphene	Nanohybrids	Electrochemical deposition	HCOH	5	4.6^b	46/95 s	0.02 ppm	364
Pd/TiO$_2$/RGO	Nanotubes	Electrochemical anodization	Methanol	700	∼70^b	—	—	365
TiO$_2$/rGO	Nanotubes	Hydrothermal	Methanol	800	96.93^b	18/61 s	10 ppm	366
Pd/SnO$_2$/rGO	Nanoparticles	Hydrothermal	Methane	4000	2.07^b	10 min/—	—	367
SnO$_2$/rGO	Hybrid films	Hydrothermal	Acetone	10	2.1^b	107/95 s	∼10 ppm	368
ZnO/MWNTs	Nanorods	Hydrothermal	Ethanol	50	4.5^b	7/11 s	∼5 ppm	369
SnO$_2$/Ni-graphene	Nanoparticles	Chemical solution	NO	40	15	—	—	370
SnO$_2$/rGO	Quantum wires	Spin coating	H$_2$S	50	33	2/292 s	43 ppb	4

C = concentration; t_{res}/t_{rec} = response time/recovery time; LOD = limit of detection; response is defined as R_a/R_g (for reducing gases) or R_g/R_a (for oxidizing gases), R_a: resistance of the sensor exposed to the reference, R_g: resistance of the sensor exposed to the target. ^{a} Here the response is defined as $\Delta R/R_g$ (for reducing gases) or $\Delta R/R_a$ (for oxidizing gases), ΔR: the change in resistance. ^{b} Here the response is defined as $(\Delta R/R_g) \times 100\%$ (for reducing gases) or $(\Delta R/R_a) \times 100\%$ (for oxidizing gases).

nanohybrids can detect a low-concentration of NO$_2$ with a highly sensitive response (14 to 1 ppm NO$_2$) and fast response/recovery times (66/34 s), mainly due to the formation of large surface areas and enhanced carrier transfers between the CuO and NO$_2$ molecules.[335] Furthermore, Ding et al. reported that the integration of chemically functionalized three-dimensional graphene oxide hydro-gels with metal–organic framework derived Co$_3$O$_4$ nanostructures achieved ultra-high response, short response time and distinct cross-selectivity.[372]

The composite of SMONs with carbon nanotubes (CNT) such as SWCNTs/SnO$_2$[373] and CNT/SnO$_2$[374–377] can also improve the sensing performance.[378] The p–n junctions formed between the SMONs and p-type MWCNTs are responsible for their enhanced gas sensing responses. For example, Srivastava et al.[124] reported an RT NO$_2$ gas sensor based on multi-walled carbon nanotubes/SnO$_2$. The sensor exhibits a much higher response to NO$_2$ than the pure SnO$_2$ based sensor operated at RT. Due to the good conductivity of the CNTs and the high porosity of the ZnO networks,[354] the response value of 2%CNTs/ZnO networks has been increased from 37 to 330 when the sensor was exposed to 100 ppm NH$_3$ at RT (see Fig. 24c). The response/recovery times are decreased from 58/61 s to 18/35 s, respectively. The sensor
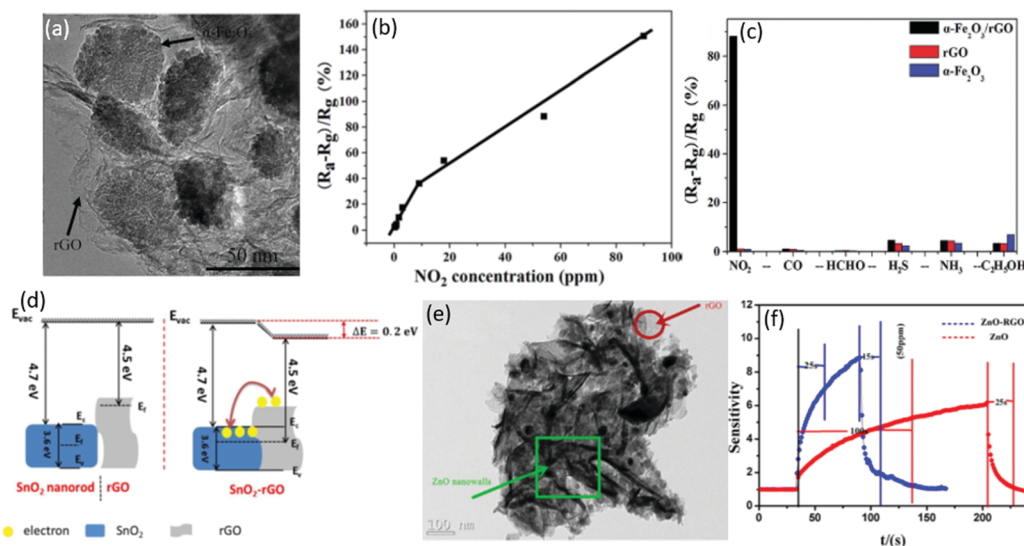
Fig. 23 (a) TEM image of the α-Fe$_2$O$_3$/rGO composite; (b) response values of the sensor based on α-Fe$_2$O$_3$/rGO at different NO$_2$ concentrations; (c) response histogram of the sensor to different gases.[342] Copyright 2014, Royal Society of Chemistry. (d) Band gap diagrams of SnO$_2$-nanorods/ reduced graphene oxide nanostructures before and after combination.[347] Copyright 2017, Elsevier. (e) TEM image of the ZnO/rGO composite; (f) response/recovery curves to 50 ppm NO$_2$ of the sensor based on a-ZnO/rGO or ZnO.[135] Copyright 2017, Elsevier.
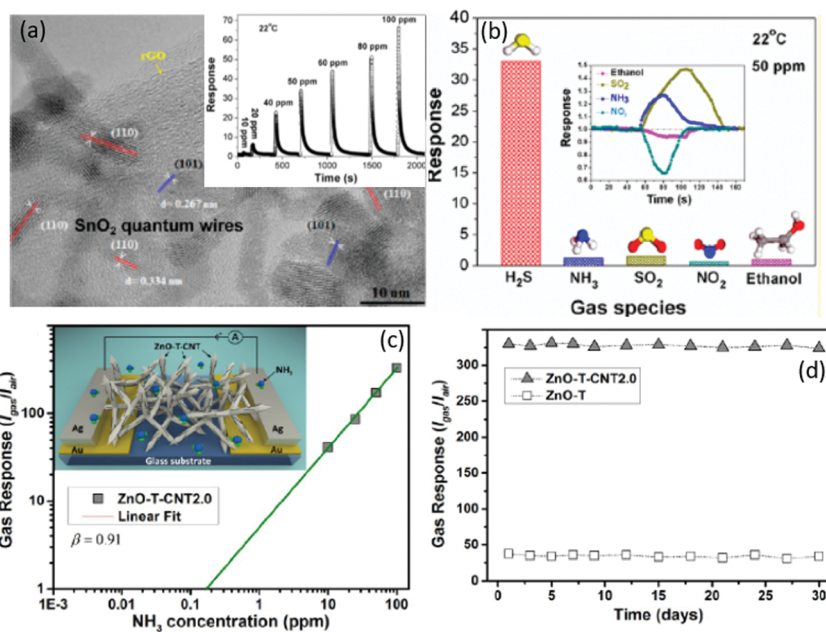
Fig. 24 (a) TEM image of the SnO$_2$ quantum wires/rGO nanosheets, the inset shows the response/recovery of the sensor based on SnO$_2$ quantum wires/rGO nanosheets for different H$_2$S concentrations; (b) response histogram of the SnO$_2$ quantum wires/rGO nanosheet based sensor to different gases.[4] Copyright 2016, American Chemical Society. (c) Response values at different concentrations of NH$_3$ gas for 2%CNTs/ZnO networks (the inset presents the sensor structure); (d) long-time stability of the RT gas sensors to 100 ppm of NH$_3$ at 30% RH.[354] Copyright 2017, American Chemical Society.

also displays good stability at RT over a duration of one month (see Fig. 24d). In addition, the CNTs can serve as acceptors for the released electrons, which are injected into the SMONs from the target gases. A H$_2$S gas sensor made of nanocomposites of SnO$_2$ quantum dots/MWCNTs reported by Liu *et al.*[379] exhibited a high response value of 108 to 50 ppm H$_2$S with fast response/recovery times of 23/44 s.

Adding noble metal nanoparticles into the composite is another method to further improve the gas sensing performance of SMONs/rGO composites. Being good catalysts, these noble metal nanoparticles can enhance the catalytic efficiency by creating extra new sites to promote fast adsorption of gas molecules and decrease the reaction temperatures by lowering the activation energy of the gas sensing reactions. For example,

Shojaee et al.[357] reported that the nanocomposites of Pd loaded SnO$_2$ and partially reduced graphene oxide showed good performance to detect CO from 50 to 1600 ppm with fast response and recovery times at 26 °C. The Pd/SnO$_2$/rGO based H$_2$ sensor[362] and Pd/TiO$_2$/rGO based NH$_3$ sensor[351] prepared using a chemical solution method exhibited higher sensitivity and faster response time than those of the SnO$_2$/rGO and TiO$_2$/rGO sensors. In addition to Pd nanoparticles, Ag nanoparticles were also used to improve the RT sensing performance of SnO$_2$–rGO hybrids for detection of NO$_2$. The Ag/SnO$_2$/rGO hybrid composites exhibit much shorter response time and recovery time (49 s and 339 s) to 5 ppm NO$_2$ at RT than the SnO$_2$–rGO hybrids (415 s and 740 s)[329].

Similar to those cases for the rGO/SMON composites, modifications of the CNT/SMON composites using noble metal nanoparticles can also improve their gas sensing properties. For example, CNT/Au/SnO$_2$ composites were synthesized by homogeneously coating SnO$_2$ and Au nanocrystals onto the CNTs, and then applied to detect CO gas at RT.[358] The sensor made of the CNT/Au/SnO$_2$ composites shows better selectivity to CO than that made of the CNT/SnO$_2$ composite. It has a high sensitivity of 70 when exposed to 2500 ppm of CO, and shows higher sensitivity values to CO gases with different concentrations varying from 500 to 2500 ppm when compared with those of the Au/SnO$_2$ composites.

In brief, due to the high conductivity of carbon nanomaterials and the formation of heterojunctions, the response/recovery times of the composites of SMONs with carbon nanomaterials are much shorter than those from the pure SMONs, although it seems that the increase of response values achieved using these composites might be less significant.

3.3 Room temperature photoactivated gas sensors based on semiconducting metal oxide nanostructures

Generally, many of the SMON-based gas sensors are needed to heat up for the best gas sensing performance, which is inconvenient in many situations. Instead, UV light can be used to activate and enhance the gas sensing performance of SMONs operated at RT.[380] The reported SMONs whose sensing properties can be improved by UV light are mainly ZnO,[381–385] In$_2$O$_3$,[386,387] TiO$_2$[388,389] and SnO$_2$,[390,391] which have been summarized in Table 7. The SMONs can absorb UV light to produce photo-generated electrons and holes. The photo-generated electrons on the surface can enhance the chemisorption of oxygen molecules to form more O$_2^-$ as listed in eqn (20) and (21),[392] thus can enhance the sensitivity and response/recovery times of the SMONs under UV light.

$$h\nu \rightarrow h^+ + e^- \tag{20}$$

$$O_2 + e^-{}_{(h\nu)} \rightarrow O_2^-{}_{(h\nu)} \tag{21}$$

With the assistance of a UV LED (photon energy of 2.5 mW), the RT gas sensor made of mesoporous hollow TiO$_2$ microspheres[388] exhibited a high response to formaldehyde with faster response/recovery (40/50 s) and good selectivity. Higher response has also been reported using the sensor made of ZnO/SnO$_2$ composite materials[395] to detect NO$_2$ under UV light illumination at RT. After the sensing materials are exposed to NO$_2$ gas, the NO$_2$ molecules will collect the photo-generated electrons to form NO and O$_2^-$ as shown in eqn (22),[393] which results in an increase in the resistance of the sensor.

$$2NO_{2(g)} + e^-{}_{(h\nu)} \rightarrow 2NO_{(h\nu)} + O_2^-{}_{(h\nu)} \tag{22}$$

Simultaneously, a heterojunction is formed at the interfaces between ZnO and SnO$_2$. The photogenerated electrons are transferred from ZnO to SnO$_2$ due to the higher Fermi energy level of ZnO than that of SnO$_2$ (see Fig. 25a). The efficient charge separation increases charge concentrations on the surface of SnO$_2$, which remarkably improves the sensitivity under UV light stimulation at RT as shown in Fig. 25b.

Apart from the UV light, visible light (including blue light and white light) assisted RT gas sensors with enhanced performance have also been reported.[387,398–400] Klaus et al.[387] reported a blue light (460 nm) activated ozone gas sensor based on nanoporous In$_2$O$_3$ particles, which showed a high response value of 200 and a low LOD of 50 ppb at RT. Geng et al.[399] reported that a sensor made of Cu$_x$O$_{1-y}$/ZnO$_{1-\alpha}$ nanocomposites showed enhanced NO$_2$

Table 7 Room temperature sensing properties of semiconducting metal oxide nanostructures enhanced by UV light

Material	Structure	Synthesis method	Target gas	C (ppm)	Response	t_{res}/t_{rec}	LOD	Ref.
ZnO	Nanorods	Hydrothermal	HCHO	110	11.5[a]	14/0.5 min	1.8 ppm	383
ZnO	Nanofibers	Electrospinning	HCHO	100	12.3	32/17 s	∼5 ppm	384
ZnO	Nanoparticles	Hydrothermal	NO$_2$	20	85[a]	26/16 s	∼1 ppm	393
ZnO	Microwires	Surface etching	NO$_2$	20	411[b]	221/118 s	∼10 ppm	381
ZnO	Nanowires	Wet-chemical	C$_2$H$_5$OH	700	85[b]	—	∼100 ppm	382
In$_2$O$_3$	Nanostructures	Arc-discharge	NO	50	41.7	∼10/— min	∼2 ppm	386
In$_2$O$_3$	Nanoporous particles	Nanocasting	Ozone	0.22	200	2.5/— min	50 ppb	387
TiO$_2$	Thin films	Rf-sputter	NO$_2$	250	∼1.8[b]	100/210 s	100 ppm	389
TiO$_2$	Hollow microspheres	Hydrothermal	HCHO	5	∼40	40/55 s	124 ppb	388
SnO$_2$	Nanowires	—	NO$_2$	10	∼85[b]	10/15 min	∼0.1 ppm	390
SnO$_2$/TiO$_2$	Hollow spheres	Thermal evaporation	Ethanol	100	160	50/150 s	—	394
ZnO/SnO$_2$	Nanorods	Wet chemical	NO$_2$	0.5	1266[a]	7/8 min	∼200 ppb	395
Ag/ZnO	Nanorods	Hydrothermal	HCHO	40	119.8[b]	—	5 ppm	396
NiO/TiO$_2$	Microspheres	Hydrothermal	NH$_3$	100	140[b]	∼400/∼400 s	∼10 ppm	397

C = concentration; t_{res}/t_{rec} = response time/recovery time; LOD = limit of detection; response is defined as R_a/R_g (for reducing gases) or R_g/R_a (for oxidizing gases), R_a: resistance of the sensor exposed to the reference, R_g: resistance of the sensor exposed to the target.[a] Here the response is defined as $\Delta R/R_g$ (for reducing gases) or $\Delta R/R_a$ (for oxidizing gases), ΔR: the change in resistance. [b] Here the response is defined as $(\Delta R/R_g) \times 100\%$ (for reducing gases) or $(\Delta R/R_a) \times 100\%$ (for oxidizing gases).
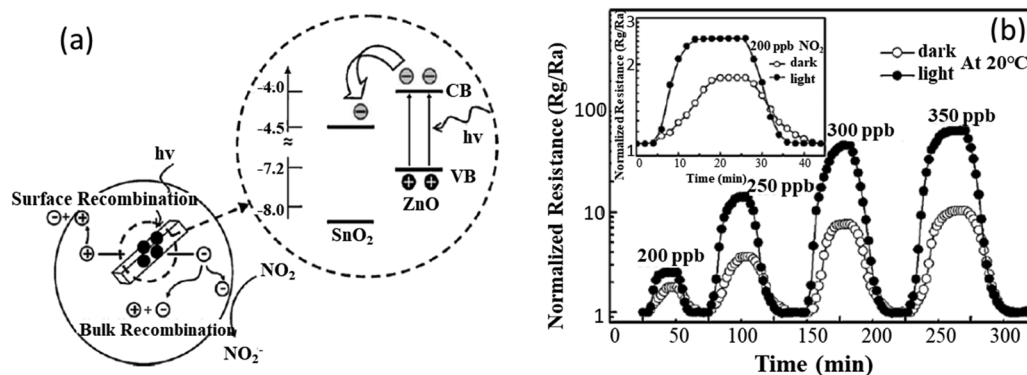
Fig. 25 (a) Schematic diagram of the carrier transport under UV light and the electron–hole pair separation on heterostructure of ZnO/SnO$_2$ composite; (b) response/recovery of ZnO/SnO$_2$ composites at different concentrations of NO$_2$ with and without UV light stimulation at room temperature.[395] Copyright 2011, Elsevier.

sensing properties at RT with high response and good selectivity after being illuminated with white light. Similarly, infrared (IR) light should also be beneficial for the improvement in the sensing performance.

Although the photoactivated SMON gas sensors could achieve the improved gas sensing performance operated at RT, the light-emitting diodes, UV source, or infrared light, as well as optical power detection devices are necessary to be used, which will increase the size and production cost of the sensor device. The integration and shrinkage of the devices along with mass production capabilities are challenges. In addition, for the application of the gas sensors in a real environment, the gas sensor will be exposed to air for real-time monitoring. Sunlight will severely influence the gas sensing response.

4. Mechanically flexible gas sensors based on semiconducting metal oxide nanostructures

Mechanically flexible gas sensors are in great demand due to their promising applications in wearable electronic devices. SMONs with a potentially higher carrier mobility and mechanical robustness are good candidates for the realization of stretchable and flexible sensors.[223] The mechanically flexible and wearable RT gas sensors based on SMONs have been an active research area recently as listed in Table 8. Compared with those on the rigid substrates, the wearable devices need substrates which are flexible, light weight, transparent, transportable, with a small volume, and low cost.[401] Due to their excellent dielectric

Table 8 Sensing performance of room temperature flexible gas sensors based on semiconducting metal oxide nanostructures

Material	Structure	Substrate	Synthesis method	Target gas	C (ppm)	Response	t_{res}/t_{rec}	LOD	Ref
ZnO	Nanowires	PET	Hydrothermal	H$_2$	1000	5^b	~600/— s	—	402
Ga/ZnO	Nanorods	PI	Hydrothermal	H$_2$	1000	91^b	~18.8/— s	0.2 ppm	264
Pd/ZnO	Nanorods	PI/PET	Hydrothermal	H$_2$	1000	91.2^b	~18.8/— s	0.2 ppm	173
ZnO	Nanorods	Nylon	Hydrothermal	H$_2$	500	109^b	149/122 s	—	409
CuO	Nanorectangles	PET	Hydrothermal	NH$_3$	5	~0.25^a	90/120 s	5 ppm	223
SnO$_2$/SnS$_2$	Nanotubes	PET	Hydrothermal	NH$_3$	100	2.48	21/110 s	1 ppm	403
Polyaniline/WO$_3$	Flowerlike	PET	Polymerization	NH$_3$	10	7	13/49 s	500 ppb	410
ZnO	Nanoparticles	Cotton fabrics	Sol–gel	NH$_3$	100	9	39/34 s	—	411
Au/In$_2$O$_3$/Polyaniline	Nanospheres	PI	Hydrothermal	NH$_3$	100	46	118/144 s	—	412
CeO$_2$/CuBr	Nanoparticles	PI	Electron beam evaporation	NH$_3$	5	68	112/74 s	20 ppb	413
Polyaniline/α-Fe$_2$O$_3$	Fiber network	PET	Sol–gel	NH$_3$	100	72^b	50/1575 s	2.5 ppm	414
Polyaniline/CeO$_2$	Thin films	PI	Self-assembly	NH$_3$	50	262.7^b	14/6 min	16 ppb	415
In/Ga/Zn/Oxide	Thin-Films	PI	CVD	NO$_2$	5	~1.3	—	2 ppm	407
ZnO$_{1-x}$	Sheet-like	PP	Suspension flame spraying	NO$_2$	1	2.568^a	60/230 min	0.25 ppm	405
MWCNTs/WO$_3$	Nanoparticles	PET	Hydrothermal	NO$_2$	5	14^b	10/27 min	0.1 ppm	416
WO$_3$/MWCNT/rGO	Nanoparticles	PI/PET	Hydrothermal	NO$_2$	5	17^b	7/15 min	1 ppm	417
SWNT/Fe$_2$O$_3$	Composites	PP	CVD	NO$_2$	100	18.3^b	—	~1 ppm	406
PdO/Co$_3$O$_4$	Nanocubes	PI	Chemical precipitation	NO$_2$	20	27.33^b	—	1 ppm	408
Cellulose/Fe$_2$O$_3$	Nanoparticles	PET	Hydrothermal	NO$_2$	200	~1100^b	50/30 s	1 ppm	418
WO$_{3-\delta}$	Films	PI	Granule spray	NO$_2$	10	18500^b	17/25 s	1.88 ppm	419
In$_2$O$_3$	Cubic crystals	PVA	Hydrothermal	Ethanol	100	~1.4	5/3 s	10 ppm	105
rGO/WO$_3$	Nanoneedles	PET	Hydrothermal	Isopropanol	200	~8.5	60/— s	1 ppm	404
Ag/ZnO	Nanorods	PI	Hydrothermal	C$_2$H$_2$	1000	26.2	66/68 s	3 ppm	420

C = concentration; t_{res}/t_{rec} = response time/recovery time; LOD = limit of detection; response is defined as R_a/R_g (for reducing gases) or R_g/R_a (for oxidizing gases), R_a: resistance of the sensor exposed to the reference, R_g: resistance of the sensor exposed to the target. ^{a} Here the response is defined as $\Delta R/R_g$ (for reducing gases) or $\Delta R/R_a$ (for oxidizing gases), ΔR: the change in resistance. ^{b} Here the response is defined as $(\Delta R/R_g) \times 100\%$ (for reducing gases) or $(\Delta R/R_a) \times 100\%$ (for oxidizing gases).

properties, and thermal and chemical stability, many plastic substrates have been used as flexible substrates for the RT gas sensors including polyethylene terephthalate (PET),[223,402–404] polypropylene (PP),[405,406] polyimide (PI),[264,407,408] polyvinyl acetate (PVA)[105] and nylon.[409]

For many of these flexible RT gas sensors, a sensitive layer such as ZnO nanorods is often used to deposit onto the device, for example, ZnO nanorods/nylon,[409] Ga-ZnO nanorods/PI,[264] Pd–ZnO nanorods/PI/PET.[173] The aqueous solution method to prepare these ZnO nanorod layers on the polymer substrate is facile with advantages of low growth temperature and easy modifications. For example, Mohammad et al.[409] prepared well-aligned ZnO nanorods on a thin nylon substrate with a thickness of 15 μm using a hydrothermal process, and then made a H_2 gas sensor. There are many contact points among ZnO nanorods which form paths of electric carriers and result in the improvement of electron transport. The mechanically flexible hydrogen gas sensor exhibited a good response value of 109% (defined as $(\Delta R/R_g) \times 100\%$) with fast response/recovery.

Rashid et al.[173] prepared vertically aligned ZnO nanorods on the PI substrate using a hydrothermal method, and then made the sensors for hydrogen detection at RT. Pd nanoparticles with 10 nm size were further sputtered on the surface of ZnO nanorods using RF magnetron sputtering. After being bent for 10^3 cycles, there were no cracks or breaks on the ZnO nanorod film (see Fig. 26a). Such flexible hydrogen sensors had a response value of ~91% (defined as $(\Delta R/R_g) \times 100\%$) for 1000 ppm hydrogen with good repeatability and stability, and a low LOD of 0.2 ppm at RT. The gas sensing performance at different bent angles from 0°, to 90° did not exhibit apparent changes (see Fig. 26b). Even after the sensor was bent to a curvature angle of 90° for 10^5 cycles, the sensing performance of this flexible H_2 sensor did not show any degradation (see Fig. 26c). The vertically well-aligned ZnO nanorods with the Pd catalyst on Ga-modified ZnO seed layer on flexible PI substrates also showed good H_2 sensing properties and good mechanical flexibility at RT with good repeatability, stability and a low LOD of 0.2 ppm, even after being bent at a curvature angle of 90°.[264]

In addition to being directly grown onto the plastic substrates, the ZnO nanowires were also transferred onto plastic substrates of PET to fabricate a flexible gas sensor using various methods, including slide transfer, roll transfer and heat transfer.[402] A 2D sheet-like ZnO layer was deposited onto the flexible

polypropylene papers using a suspension flame spraying method, and the prepared ZnO flexible sensor exhibited good responses and stability to sub-ppm level of NO_2 at RT under white LED light illumination.[405]

Other types of SMONs have also been applied for making flexible RT gas sensors, and these include WO_3, SnO_2, CeO_2, Co_3O_4, In_2O_3, etc. For example, Ryu et al.[419] fabracted flexible RT NO_2 gas sensors based on a WO_3-δ film on a plastic substrate of polyimide (PI) using the granule spray method with a vacuum process. The sensor has a repsonse of up to 18500% to 10 ppm NO_2 with fast response/recovery times of 17/25 s and reliable flexibility after 4000 bending/extending cycles. As another example, a nanocompsite of polyaniline and nanoflower-like WO_3 synthesized using a facile chemicaloxidation polymerization process was prepared on a PET substrate to fabricate a NH_3 flexible sensor, which shows a high response and fast response/recovery times (13/49 s) to 10 ppm NH_3 at RT.[410]

Modifying the SMONs using polyaniline (PANI) can effectivly enhance the sensing performance and stability of the flexible gas sensors, such as PANI–CeO_2, PANI/α-Fe_2O_3 and PANI/WO_3. The morphology and sensing performance of flexible RT NH_3 gas sensors based on PANI–CeO_2 nanocomposite thin films are stable after being bent/cycled for 500 times.[415] Furthermore, adding noble metals into the SMON/PANI composites can further improve their RT sensing performance. For example, after adding Au nanoparticles, the response of the RT NH_3 gas sensor made of the composite of mesoporous In_2O_3 nanospheres/polyaniline has been increased up to 4 times higher.[412]

Graphene and carbon nanotubes have excellent performance during severe plastic deformation, thus the composite integrating these carbon nanomaterials with the SMONs can achieve excellent sensing performance and mechanical flexibility. For example, a flexible isopropanol sensor was fabricated using a mixture of $WO_3 \cdot 0.33H_2O$ nano-needles and rGO on PET substrates (see Fig. 27a).[404] Compared with the sensor made of pure $WO_3 \cdot 0.33H_2O$ nano-needles, the 5%rGO/$WO_3 \cdot 0.33H_2O$ based sensor showed better selectivity and a superior response (4.96 to 100 ppm to isopropanol) (see Fig. 27b), with good performance after repeated bending for many cycles. Similarly, SWNT–Fe_2O_3 composite films were prepared using the CVD method and then transferred onto the flexible PP polymer substrate.[406] Compared with that fabricated using the single SWNTs, the flexible gas sensor of the SWNT–Fe_2O_3 composite film exhibited

Fig. 26 (a) SEM images of Pd/ZnO nanorods after 10^3 times bending/relaxing. (b) Response/recovery curves of the flexible sensor to H_2 at different bending angles, (c) the reliability test of the flexible sensor.[173] Copyright 2013, Elsevier.
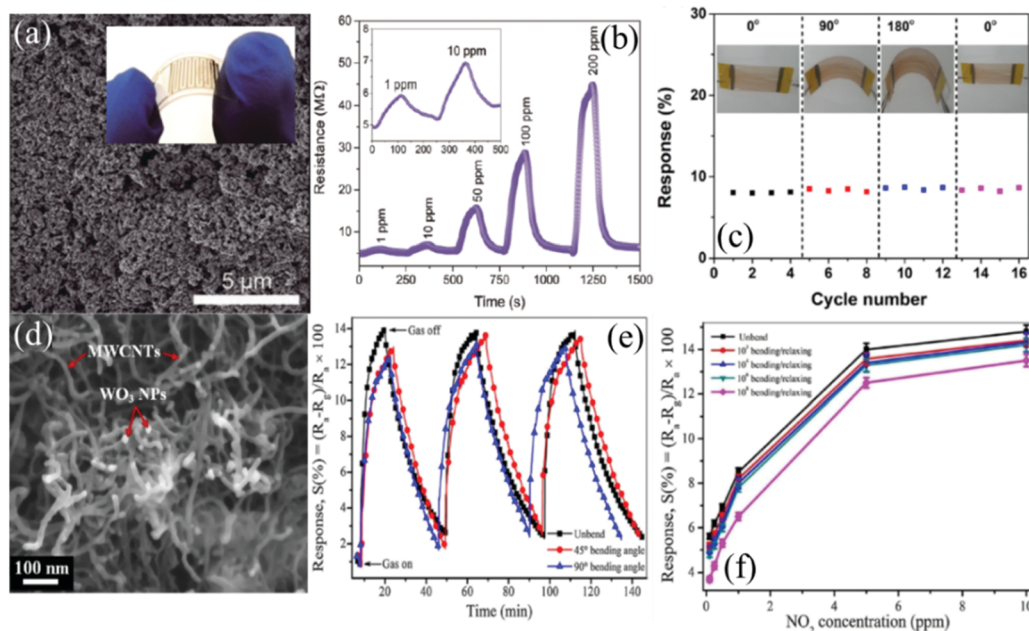
Fig. 27 (a) SEM images of 5%rGO/WO$_3$·0.33H$_2$O deposited on polyethylene terephthalate; the inset is the photograph of the flexible gas sensor, (b) response/recovery curves to isopropanol with different concentrations.[404] Copyright 2018, Royal Society of Chemistry. (c) Responses of the SWNT/Fe$_2$O$_3$ gas sensor to 20 ppm H$_2$S under different bending angles from 0° to 180° and back to 0°.[406] Copyright 2017, Elsevier. (d) SEM images of the MWCNTs/WO$_3$ composite, (e) response curves to 5 ppm NO$_2$ at RT under different bending angles, (f) responses to different NO$_2$ concentrations at RT after bending/relaxing several times (90° angle).[416] Copyright 2015, Elsevier.

an improved response to H$_2$S at RT. Under repeated bending to large angles (such as 90° and 180°) for 16 times as shown in Fig. 27c, the flexible sensor exhibited stable sensing response values to H$_2$S. As another example, hydrothermally synthesized WO$_3$ nanoparticles were mixed with MWCNTs (see Fig. 27d), and then cast onto a PET substrate to fabricate a flexible NO$_2$ gas sensor.[416] This sensor not only shows good sensing performance, but also has excellent mechanical flexibility (see Fig. 27e). There was no significant degradation of response values after bending/relaxing for 10^6 cycles, demonstrating the excellent mechanical robustness of the MWCNTs/WO$_3$ composite layers on the flexible gas sensors (see Fig. 27f).

Cotton fabrics are also reported to be used as a good substrate for flexible RT gas sensors, for example, a flexible NH$_3$ gas sensor was made by growing nanostructured ZnO onto cotton fabrics.[411] Flexible nanowires of the SMONs can also be isostatically pressed into a thin paper, and then the nanowire paper is cut into small pieces to directly fabricate a flexible gas sensor. Based on this idea, a-MoO$_3$ nanowire paper[421] has been fabricated and a flexible gas sensor was made to detect hydrogen gas. The sensor shows fast response and recovery speeds (3.0 and 2.7 s toward 1.5% H$_2$), good selectivity, and high sensitivity at RT. Wei *et al.*[422] also reported a flexible gas sensor based on cellulose/TiO$_2$/PANI composite nanofibers, which showed excellent ammonia gas sensing performance at RT. Similarly, a stretchable ZnO nano-accordion structure has also shown good applications in flexible RT gas sensors.[423]

In summary, flexible RT gas sensors can be fabricated using SMONs as the sensing materials on a mechanically flexible platform,

and the sensors have demonstrated excellent mechanical robustness and can maintain good sensing performance at RT after bending/recovering many times. Furthermore, the composite of SMONs with graphene or CNT can achieve better mechanical robustness for the flexible gas sensor. However, so far, excellent sensing performance and reliability and stability have not been achieved in the case of flexible RT gas sensors compared with their rigid counterparts.

5. Conclusions and outlook

In this paper, we have summarized the recent progress in designs and mechanisms of RT gas sensors based on different SMONs. Our emphasis has been on the critical review of different structures of SMON-based gas sensors that may help the design of new devices. The key topics covered in this paper include single phase n-type SMONs, single phase p-type SMONs, noble metal nanoparticle modified SMONs, metal ion modified SMONs, SMON composites with multiple metal oxides, and SMON composites with carbon nanomaterials. The different nanostructures of these SMONs include nanoparticles, nanowires, nanofibers, nanorods, nanosheets, nanotubes *etc.* The sensing performance of these SMON based RT sensors has been reviewed for detecting various toxic or flammable gases, such as hydrogen disulfide, nitrogen dioxide, ammonia, carbon monoxide and hydrogen, as well as organic gases of formaldehyde, acetone, methanol and ethanol, *etc.* In addition, photoactivated RT gas sensors and flexible RT gas sensors based on SMONs are also summarized.

Availability of numerous surface chemisorbed oxygen species of O_2^- at RT was identified to be the key reason for the high sensitivity of these RT gas sensors. These oxygen species react with the target molecules to change the electronic resistance of the sensor. However, many RT H_2S sensors are exceptional as the sensing mechanism is dominated by the formation of metallic conducting metal sulfide.

Noble metal nanoparticles on the surface of SMONs can stimulate the adsorption of oxygen molecules to form oxygen ions by reduction processes. These oxygen ions spill onto the surface of SMONs to improve the concentration of oxygen ions on the surface of SMONs for sensing reactions. In addition, noble metal nanoparticles can accelerate the transfer of electrons to SMONs. Therefore, both the chemical sensitization and electronic sensitization enhance the sensitivity and speed of the SMON-based sensors. Doping of metal ions in the SMONs can increase the number of active sites and defects on the surface of SMON nanocrystals, and thus enhance the amount of oxygen species and increase the adsorbed gas molecules on the sensor surface. Heterojunctions can form at the interfaces of different metal oxides or at the interfaces between the SMONs and carbon nanomaterials. These can effectively accelerate the transformation of electrons and enhance oxygen adsorption, and are beneficial to improve the sensitivity and response rates in application of RT gas sensors. The sensing performance also depends significantly on the nanostructures of the SMONs. Large specific surfaces are beneficial to the formation of more oxygen species, and porous nanostructures facilitate the adsorption and desorption of target gases, thus achieving fast response and recovery.

Generally, the RT SMON based gas sensors show high response values and low LODs; however, their response and recovery times could be too long. Modifications of the SMON sensors using various methods can improve their sensing performance, which include using noble metal modified SMONs; metal ion doped SMONs, composite SMONs, and composites with carbon nanomaterials. The key conclusions are summarized below:

(1) Surface modifications of the SMONs using noble metal nanoparticles can effectively enhance their sensitivity, response/recovery speeds, selectivity and LODs through both chemical sensitization and electronic sensitization.

(2) Metal ion doped SMONs have increased number of active sites and more defects on their surfaces, which can enhance the oxygen species for sensing reactions and improve the adsorption of gas molecules.

(3) SMON composites can form abundant oxygen vacancies on their surfaces, thus providing many active sites. Heterojunctions can be formed at the interfaces of different metal oxides, which can effectively accelerate the transformation of electrons between different particles, thus improving the response rates. The composite SMONs often contain numerous mesopores which are beneficial to the adsorption and desorption of gas molecules. Hence, sensors based on the majority of reported composite oxides exhibit a high response value and very fast response.

(4) Because of the high conductivity of carbon nanomaterials, the composites of SMONs combined with carbon nanomaterials can achieve fast response/recovery.

(5) The photo-generated electrons on the surfaces of SMON sensing materials can enhance the chemisorption of oxygen molecules to form more O_2^-, which can enhance the sensitivity and response/recovery speed of the SMONs.

(6) RT flexible gas sensors based on the sensing layer of the SMON sensing materials have excellent mechanical robustness and can maintain good sensing performance after repeated bending/recovering.

Although there has been significant progress in developing novel SMONs for gas sensing at RT, there are still many challenges and problems towards achieving high response, fast response/recovery speed, good selectivity and long-term stability:

(1) One of the key challenges is the durability and long-term stability of the sensors for application under varying environmental conditions, such as different humidity levels and different temperatures, which could have significant influences on the sensing properties of many RT gas sensors. This is especially important for RT NH_3 sensing, as high humidity seriously affects the sensitivity and the response time. Light exposure, especially ultraviolet and infrared light, and even visible light, all influence the response of the RT SMON sensors. In the literature, the performance of sensors has been normally characterized based on experiments conducted in a well-controlled laboratory environment. However, in a practical setting with variable environmental conditions, the sensing performance may be altered with light exposure. Therefore, the sensing properties under different environmental conditions should be systematically investigated in order to establish the relationship between environmental conditions and sensing properties, which are then used to correct the sensing results.

(2) Interfering gases often affect the sensing performance, resulting in a drastically reduced response. Lack of good selectivity is still the most serious problem hindering the wide applications of these RT gas sensors. There are few reports on specific gas sensors which only respond to a target gas but not all the other gases. Because the resistive gas sensors rely on their changes in resistance upon adsorption of gas molecules, it can distinguish between the reducing gases and oxidizing gases based on the increase or decrease of resistance; however, it is difficult to discriminate a group of gases which can produce similar changing trends of resistance values.

Therefore, selectivity is particularly important for multiple-agent gas sensors. To solve this problem, arrays of different sensing materials can be fabricated such that forming an array of gas sensors, which could obtain good selectivity by analyzing and comparing data from the different single sensors.[424] For example, Zhang et al.[425] reported a method to detect multiple VOCs using an array of gas sensors based on Ag doped $LaFeO_3$ (ALFO). The device was optimized for the detection of acetone, benzene, methanol and formaldehyde to monitor air quality. The selectivity of ALFO can be altered using a molecular imprinting technique towards specific targets. Responsivity values of individual sensing elements vary between 14 and 21 while the values to other VOCs are lower than 4. The response and recovery times are on the order of 10 s and 100 s levels. Flitti et al.[426] reported a micromachined 4×4 array of sensors

for multiple target detection. The sensing film for individual elements is based on SnO$_2$ and the elements are post-treated using metal catalysts of Pt, Pd, and Au and ions implanted using B, P, and H. The basic post-treatment methods are effective in selectively detecting gases of CO, CH$_4$, ethanol, CH$_4$–CO, ethanol–CO, and ethanol–CH$_4$ using an algorithm based on vector angle similarity. Recognition accuracy higher than 95% is reported in this study.[427] This method has been demonstrated being capable of forming 12 000 virtual sensors using dedicated temperature modulations. Sensing networks will be the future trends.

(3) The sensing mechanism of the SMONs is mainly based on the interaction between the target gas molecules and chemisorbed oxygen species, such as O$_2^-$, O$^-$ and O^{2-} ions. However, other oxygen groups such as OH$^-$ can also react with the target gas molecules. More effective analysis and theory development of the surface groups is urgently needed to assess their effect on the sensing properties, and the surface modification methods should be developed to minimize this influence.

(4) Many gas sensing mechanisms of SMON based materials with various sizes and morphologies have been presented to explain their sensing properties. However, it is not clearly elucidated why the same SMON based materials with similar sizes and morphologies show markedly different sensing properties. Therefore, *in situ* characterization techniques and theory development for the sensing mechanisms are necessary.

(5) Response times of many RT gas sensors are very long, which cannot meet the need for timely triggering of the alarm. Exploring novel SMON based sensing materials for rapid response at RT is still necessary. 3-D nano-arrays of SMONs facilitate gas diffusion, which might be promising to shorten the response time.

(6) Flexible wearable RT gas sensors are in great demand due to their promising applications. SMONs with the potential of higher carrier mobility and mechanical robustness are among the good candidates for making stretchable and flexible gas sensors. For RT gas sensors, there are still challenges regarding their manufacturing technologies, and cracking and spalling problems of SMON layers on the flexible substrates usually happen, which need to be solved to achieve reliable RT flexible gas sensors. Therefore, finding new low-cost SMON based sensing materials with excellent sensing performance and mechanical robustness is still the major challenge.

Conflicts of interest

There are no conflicts to declare.

Acknowledgements

References

1 M. Jerrett, D. Donaire-Gonzalez, O. Popoola, R. Jones, R. C. Cohen, E. Almanza, A. de Nazelle, I. Mead, G. Carrasco-Turigas, T. Cole-Hunter, M. Triguero-Mas, E. Seto and M. Nieuwenhuijsen, *Environ. Res.*, 2017, **158**, 286–294.

2 Z. A. Barakeh, P. Breuil, N. Redon, C. Pijolat, N. Locoge and J.-P. Viricelle, *Sens. Actuators, B*, 2017, **241**, 1235–1243.

3 D. Sett and D. Basak, *Sens. Actuators, B*, 2017, **243**, 475–483.

4 Z. Song, Z. Wei, B. Wang, Z. Luo, S. Xu, W. Zhang, H. Yu, M. Li, Z. Huang, J. Zang, F. Yi and H. Liu, *Chem. Mater.*, 2016, **28**, 1205–1212.

5 H. Ren, C. Gu, S. W. Joo, J. Zhao, Y. Sun and J. Huang, *Sens. Actuators, B*, 2018, **266**, 506–513.

6 G. Tuerdi, P. Nizamidin, N. Kari, A. Yimit and F. Wang, *RSC Adv.*, 2018, **8**, 5614–5621.

7 A. Paliwal, A. Sharma, M. Tomar and V. Gupta, *Sens. Actuators, B*, 2017, **250**, 679–685.

8 B. Gong, T. Shi, W. Zhu, G. Liao, X. Li, J. Huang, T. Zhou and Z. Tang, *Sens. Actuators, B*, 2017, **245**, 821–827.

9 R. Kitture, D. Pawar, C. N. Rao, R. K. Choubey and S. N. Kale, *J. Alloys Compd.*, 2017, **695**, 2091–2096.

10 M. Asad and M. H. Sheikhi, *Sens. Actuators, B*, 2014, **198**, 134–141.

11 S.-H. Wang, C.-Y. Shen, H.-M. Huang and Y.-C. Shih, *Sens. Actuators, A*, 2014, **216**, 237–242.

12 L. Rana, R. Gupta, M. Tomar and V. Gupta, *Sens. Actuators, B*, 2017, **252**, 840–845.

13 T. Goto, T. Itoh, T. Akamatsu, N. Izu and W. Shin, *Sens. Actuators, B*, 2016, **223**, 774–783.

14 L. Sun, W. L. Luan, T. C. Wang, W. X. Su and L. X. Zhang, *Nanotechnology*, 2017, **28**, 075501.

15 H. Liang, X. Zhang, H. Sun, H. Jin, X. Zhang, Q. Jin, J. Zou, H. Haick and J. Jian, *ACS Sens.*, 2017, **2**, 1467–1473.

16 G. Jiang, M. Goledzinowski, F. J. E. Comeau, H. Zarrin, G. Lui, J. Lenos, A. Veileux, G. Liu, J. Zhang, S. Hemmati, J. Qiao and Z. Chen, *Adv. Funct. Mater.*, 2016, **26**, 1729–1736.

17 E. Menart, V. Jovanovski and S. B. Hočevar, *Sens. Actuators, B*, 2017, **238**, 71–75.

18 S. S. Shendage, V. L. Patil, S. A. Vanalakar, S. P. Patil, N. S. Harale, J. L. Bhosale, J. H. Kim and P. S. Patil, *Sens. Actuators, B*, 2017, **240**, 426–433.

19 Y. Li, N. Chen, D. Deng, X. Xing, X. Xiao and Y. Wang, *Sens. Actuators, B*, 2017, **238**, 264–273.

20 R. Kumar, O. Al-Dossary, G. Kumar and A. Umar, *Nano-Micro Lett.*, 2014, **7**, 97–120.

21 A. Dey, *Mater. Sci. Eng., B*, 2018, **229**, 206–217.

22 S. W. Lee, W. Lee, Y. Hong, G. Lee and D. S. Yoon, *Sens. Actuators, B*, 2018, **255**, 1788–1804.

23 H. Wu, Z. Chen, J. Zhang, F. Wu, C. He, Y. Wu and Z. Ren, *J. Mater. Chem. A*, 2017, **5**, 24493–24501.

24 S. Park, M. Park, S. Kim, S.-G. Yi, M. Kim, J. Son, J. Cha, J. Hong and K.-H. Yoo, *Appl. Phys. Lett.*, 2017, **111**, 213102.

25 S. W. Lee, W. Lee, D. Lee, Y. Choi, W. Kim, J. Park, J. H. Lee, G. Lee and D. S. Yoon, *Sens. Actuators, B*, 2018, **266**, 485–492.

26 N. Joshi, T. Hayasaka, Y. Liu, H. Liu, O. N. Oliveira, Jr. and L. Lin, *Mikrochim. Acta*, 2018, **185**, 213.

27 Y. Li, M. Jiao, H. Zhao and M. Yang, *Sens. Actuators, B*, 2018, **264**, 285–295.

28 J. Cai, C. Zhang, A. Khan, C. Liang and W.-D. Li, *RSC Adv.*, 2018, **8**, 5312–5320.

29 H. J. Park, W.-J. Kim, H.-K. Lee, D.-S. Lee, J.-H. Shin, Y. Jun and Y. J. Yun, *Sens. Actuators, B*, 2018, **257**, 846–852.

30 H. T. Hien, H. T. Giang, N. V. Hieu, T. Trung and C. V. Tuan, *Sens. Actuators, B*, 2017, **249**, 348–356.

31 V. L. Patil, S. A. Vanalakar, P. S. Patil and J. H. Kim, *Sens. Actuators, B*, 2017, **239**, 1185–1193.

32 M. Jiao, N. V. Chien, N. V. Duy, N. D. Hoa, N. V. Hieu, K. Hjort and H. Nguyen, *Mater. Lett.*, 2016, **169**, 231–235.

33 D. N. Oosthuizen, D. E. Motaung and H. C. Swart, *Sens. Actuators, B*, 2018, **266**, 761–772.

34 X. Liu, M. Hu, Y. Wang, J. Liu and Y. Qin, *J. Alloys Compd.*, 2016, **685**, 364–369.

35 A. Umar, J.-H. Lee, R. Kumar, O. Al-Dossary, A. A. Ibrahim and S. Baskoutas, *Mater. Des.*, 2016, **105**, 16–24.

36 O. Lupan, V. Postica, V. Cretu, N. Wolff, V. Duppel, L. Kienle and R. Adelung, *Phys. Status Solidi RRL*, 2016, **10**, 260–266.

37 S. Xu, H. Zhao, Y. Xu, R. Xu and Y. Lei, *ACS Appl. Mater. Interfaces*, 2018, **10**, 13895–13902.

38 I. Cho, K. Kang, D. Yang, J. Yun and I. Park, *ACS Appl. Mater. Interfaces*, 2017, **9**, 27111–27119.

39 Y. Zhao, W. Zhang, B. Yang, J. Liu, X. Chen, X. Wang and C. Yang, *Nanotechnology*, 2017, **28**, 452002.

40 X. Tong, W. Shen, X. Chen and J.-P. Corriou, *Ceram. Int.*, 2017, **43**, 14200–14209.

41 W. Guo, Q. Feng, Y. Tao, L. Zheng, Z. Han and J. Ma, *Mater. Res. Bull.*, 2016, **73**, 302–307.

42 Z. Li, Y. Huang, S. Zhang, W. Chen, Z. Kuang, D. Ao, W. Liu and Y. Fu, *J. Hazard. Mater.*, 2015, **300**, 167–174.

43 Z. Li, Z. Lin, N. Wang, Y. Huang, J. Wang, W. Liu, Y. Fu and Z. Wang, *Mater. Des.*, 2016, **110**, 532–539.

44 D. Han, L. Zhai, F. Gu and Z. Wang, *Sens. Actuators, B*, 2018, **262**, 655–663.

45 J. Hu, Y. Sun, Y. Xue, M. Zhang, P. Li, K. Lian, S. Zhuiykov, W. Zhang and Y. Chen, *Sens. Actuators, B*, 2018, **257**, 124–135.

46 S. C. Zhang, Y. W. Huang, Z. Kuang, S. Y. Wang, W. L. Song, D. Y. Ao, W. Liu and Z. J. Li, *Nanosci. Nanotechnol. Lett.*, 2015, **7**, 455–461.

47 Z. Li, S. Yan, Z. Wu, H. Li, J. Wang, W. Shen, Z. Wang and Y. Fu, *Int. J. Hydrogen Energy*, 2018, **43**, 22746–22755.

48 T. Zhou, T. Zhang, J. Deng, R. Zhang, Z. Lou and L. Wang, *Sens. Actuators, B*, 2017, **242**, 369–377.

49 S. F. Shen, M. L. Xu, D. B. Lin and H. B. Pan, *Appl. Surf. Sci.*, 2017, **396**, 327–332.

50 Z. Zhang, L. Zhu, Z. Wen and Z. Ye, *Sens. Actuators, B*, 2017, **238**, 1052–1059.

51 S. Poongodi, P. S. Kumar, D. Mangalaraj, N. Ponpandian, P. Meena, Y. Masuda and C. Lee, *J. Alloys Compd.*, 2017, **719**, 71–81.

52 H. Kim, Y. Pak, Y. Jeong, W. Kim, J. Kim and G. Y. Jung, *Sens. Actuators, B*, 2018, **262**, 460–468.

53 R. Sankar Ganesh, M. Navaneethan, V. L. Patil, S. Ponnusamy, C. Muthamizhchelvan, S. Kawasaki, P. S. Patil and Y. Hayakawa, *Sens. Actuators, B*, 2018, **255**, 672–683.

54 X. Hu, Z. Zhu, C. Chen, T. Wen, X. Zhao and L. Xie, *Sens. Actuators, B*, 2017, **253**, 809–817.

55 L. Xiao, S. Xu, G. Yu and S. Liu, *Sens. Actuators, B*, 2018, **255**, 2002–2010.

56 V. S. Bhati, S. Ranwa, S. Rajamani, K. Kumari, R. Raliya, P. Biswas and M. Kumar, *ACS Appl. Mater. Interfaces*, 2018, **10**, 11116–11124.

57 V. S. Bhati, S. Ranwa, M. Fanetti, M. Valant and M. Kumar, *Sens. Actuators, B*, 2018, **255**, 588–597.

58 V. V. Ganbavle, S. I. Inamdar, G. L. Agawane, J. H. Kim and K. Y. Rajpure, *Chem. Eng. J.*, 2016, **286**, 36–47.

59 X. Kou, N. Xie, F. Chen, T. Wang, L. Guo, C. Wang, Q. Wang, J. Ma, Y. Sun, H. Zhang and G. Lu, *Sens. Actuators, B*, 2018, **256**, 861–869.

60 Q. Zhou, W. Chen, L. Xu, R. Kumar, Y. Gui, Z. Zhao, C. Tang and S. Zhu, *Ceram. Int.*, 2018, **44**, 4392–4399.

61 C. Zhao, H. Gong, W. Lan, R. Ramachandran, H. Xu, S. Liu and F. Wang, *Sens. Actuators, B*, 2018, **258**, 492–500.

62 H. W. Kim, H. G. Na, Y. J. Kwon, S. Y. Kang, M. S. Choi, J. H. Bang, P. Wu and S. S. Kim, *ACS Appl. Mater. Interfaces*, 2017, **9**, 31667–31682.

63 P. Tyagi, A. Sharma, M. Tomar and V. Gupta, *Sens. Actuators, B*, 2017, **248**, 980–986.

64 B. Zhang, M. Cheng, G. Liu, Y. Gao, L. Zhao, S. Li, Y. Wang, F. Liu, X. Liang, T. Zhang and G. Lu, *Sens. Actuators, B*, 2018, **263**, 387–399.

65 S. Park, S. Kim, H. Kheel, S. K. Hyun, C. Jin and C. Lee, *Mater. Res. Bull.*, 2016, **82**, 130–135.

66 D. Li, L. Qin, P. Zhao, Y. Zhang, D. Liu, F. Liu, B. Kang, Y. Wang, H. Song, T. Zhang and G. Lu, *Sens. Actuators, B*, 2018, **254**, 834–841.

67 H. Gao, L. Zhao, L. Wang, P. Sun, H. Lu, F. Liu, X. Chuai and G. Lu, *Sens. Actuators, B*, 2018, **255**, 3505–3515.

68 I. Eisele, T. Doll and M. Burgmair, *Sens. Actuators, B*, 2001, **78**, 19–25.

69 S. Stegmeier, M. Fleischer, A. Tawil, P. Hauptmann, K. Egly and K. Rose, *Sens. Actuators, B*, 2011, **154**, 270–276.

70 A. I. Ayesh, *J. Nanomater.*, 2016, **2016**, 1–17.

71 Z. S. Hosseini, A. I. Zad and A. Mortezaali, *Sens. Actuators, B*, 2015, **207**, 865–871.

72 T. Sin Tee, T. Chun Hui, C. Wu Yi, Y. Chi Chin, A. A. Umar, G. Riski Titian, L. Hock Beng, L. Kok Sing, M. Yahaya and M. M. Salleh, *Sens. Actuators, B*, 2016, **227**, 304–312.

73 A. Azam, S. S. Habib, N. A. Salah and F. Ahmed, *Int. J. Nanomed.*, 2013, **8**, 3875–3881.

74 H. Wang, Q. Sun, Y. Yao, Y. Li, J. Wang and L. Chen, *Ceram. Int.*, 2016, **42**, 8565–8571.

75 W. Li, J. Liang, J. Liu, L. Zhou, R. Yang and M. Hu, *Mater. Lett.*, 2016, **173**, 199–202.

76 Y. Wei, C. Chen, G. Yuan and S. Gao, *J. Alloys Compd.*, 2016, **681**, 43–49.

77 Y. Li, Q. Zhang, X. Li, H. Bai, W. Li, T. Zeng and G. Xi, *RSC Adv.*, 2016, **6**, 95747–95752.

78 S. Mohamed Sali, S. Joy, N. Meenakshisundaram, R. K. Karn, C. Gopalakrishnan, P. Karthick, K. Jeyadheepan and K. Sankaranarayanan, *RSC Adv.*, 2017, **7**, 37720–37728.

79 Z. P. Tshabalala, D. E. Motaung, G. H. Mhlongo and O. M. Ntwaeaborwa, *Sens. Actuators, B*, 2016, **224**, 841–856.

80 Y. Huang, W. Chen, S. Zhang, Z. Kuang, D. Ao, N. R. Alkurd, W. Zhou, W. Liu, W. Shen and Z. Li, *Appl. Surf. Sci.*, 2015, **351**, 1025–1033.

81 R. K. Bedi and I. Singh, *ACS Appl. Mater. Interfaces*, 2010, **2**, 1361–1368.

82 P. Shankar and J. B. B. Rayappan, *ACS Appl. Mater. Interfaces*, 2017, **9**, 38135–38145.

83 N. Kumar, A. K. Srivastava, R. Nath, B. K. Gupta and G. D. Varma, *Dalton Trans.*, 2014, **43**, 5713–5720.

84 Z. Zeng, K. Wang, Z. Zhang, J. Chen and W. Zhou, *Nanotechnology*, 2009, **20**, 045503.

85 Y. Shen, S. Zhao, J. Ma, X. Chen, W. Wang, D. Wei, S. Gao, W. Liu, C. Han and B. Cui, *J. Alloys Compd.*, 2016, **664**, 229–234.

86 Z. Li, X. Niu, Z. Lin, N. Wang, H. Shen, W. Liu, K. Sun, Y. Q. Fu and Z. Wang, *J. Alloys Compd.*, 2016, **682**, 647–653.

87 O. Lupan, V. Postica, R. Adelung, F. Labat, I. Ciofini, U. Schürmann, L. Kienle, L. Chow, B. Viana and T. Pauporté, *Phys. Status Solidi RRL*, 2018, **12**, 1700321.

88 Y. L. Wang, X. C. Jiang and Y. N. Xia, *J. Am. Chem. Soc.*, 2003, **125**, 16176–16177.

89 O. Lupan, L. Chow, T. Pauporté, L. K. Ono, B. Roldan Cuenya and G. Chai, *Sens. Actuators, B*, 2012, **173**, 772–780.

90 W. Song, H. Wu, J. Wang, Y. Lin, J. Song, Y. Xie, L. Li and K. Shi, *Aust. J. Chem.*, 2015, **68**, 1569.

91 L. Yu, F. Guo, S. Liu, B. Yang, Y. Jiang, L. Qi and X. Fan, *J. Alloys Compd.*, 2016, **682**, 352–356.

92 Z. Li, Z. Lin, N. Wang, J. Wang, W. Liu, K. Sun, Y. Q. Fu and Z. Wang, *Sens. Actuators, B*, 2016, **235**, 222–231.

93 Z. Li, N. Wang, Z. Lin, J. Wang, W. Liu, K. Sun, Y. Q. Fu and Z. Wang, *ACS Appl. Mater. Interfaces*, 2016, **8**, 20962–20968.

94 J. Zhang, D. Zeng, Q. Zhu, J. Wu, Q. Huang and C. Xie, *J. Phys. Chem. C*, 2016, **120**, 3936–3945.

95 C. Jiang, G. Zhang, Y. Wu, L. Li and K. Shi, *CrystEngComm*, 2012, **14**, 2739.

96 A. Hazra, K. Dutta, B. Bhowmik, P. P. Chattopadhyay and P. Bhattacharyya, *Appl. Phys. Lett.*, 2014, **105**, 081604.

97 B. Bhowmik, A. Hazra, K. Dutta and P. Bhattacharyya, *IEEE Trans. Device Mater. Reliab.*, 2014, **14**, 961–967.

98 J. Z. Zhang and Y. Yan, *J. Mater. Sci.*, 2017, **52**, 13711–13718.

99 S. Shao, H. Wu, S. Wang, Q. Hong, R. Koehn, T. Wu and W.-F. Rao, *J. Mater. Chem. C*, 2015, **3**, 10819–10829.

100 H. Duan, L. Yan, Y. He, H. Li, L. Liu, Y. Cheng and L. Du, *Mater. Res. Express*, 2017, **4**, 095022.

101 Y. Wang, G. Duan, Y. Zhu, H. Zhang, Z. Xu, Z. Dai and W. Cai, *Sens. Actuators, B*, 2016, **228**, 74–84.

102 J. Gao, H. Wu, J. Zhou, L. Yao, G. Zhang, S. Xu, Y. Xie, L. Li and K. Shi, *New J. Chem.*, 2016, **40**, 1306–1311.

103 B. Wu, L. Wang, H. Wu, K. Kan, G. Zhang, Y. Xie, Y. Tian, L. Li and K. Shi, *Microporous Mesoporous Mater.*, 2016, **225**, 154–163.

104 M. Kaur, N. Jain, K. Sharma, S. Bhattacharya, M. Roy, A. K. Tyagi, S. K. Gupta and J. V. Yakhmi, *Sens. Actuators, B*, 2008, **133**, 456–461.

105 M. Seetha, P. Meena, D. Mangalaraj, Y. Masuda and K. Senthil, *Mater. Chem. Phys.*, 2012, **133**, 47–54.

106 R. Senthilkumar, G. Ravi, C. Sanjeeviraja, M. Arivanandhan and Y. Hayakawa, *Solid State Phys.*, 2013, **1512**, 648–649.

107 D. F. Rodriguez, P. M. Perillo, C. A. Rinaldi, A. Lamagna and P. Gouma, *AIP Conf. Proc.*, 2011, **1362**, 199–200.

108 M. N. Cardoza-Contreras, J. M. Romo-Herrera, L. A. Rios, R. Garcia-Gutierrez, T. A. Zepeda and O. E. Contreras, *Sensors*, 2015, **15**, 30539–30544.

109 C. Wang, X. Chu and M. Wu, *Sens. Actuators, B*, 2006, **113**, 320–323.

110 Y. Xia, J. Wang, X. Li, X. Dan, D. Zhou, L. Xiang and S. Komarneni, *Ceram. Int.*, 2016, **42**, 15876–15880.

111 N. Du, H. Zhang, B. D. Chen, X. Y. Ma, Z. H. Liu, J. B. Wu and D. R. Yang, *Adv. Mater.*, 2007, **19**, 1641–1645.

112 P. Dhivya and M. Sridharan, *J. Electron. Mater.*, 2014, **43**, 3211–3216.

113 S. Arunkumar, T. Hou, Y.-B. Kim, B. Choi, S. H. Park, S. Jung and D.-W. Lee, *Sens. Actuators, B*, 2017, **243**, 990–1001.

114 S.-W. Choi and S. S. Kim, *Sens. Actuators, B*, 2012, **168**, 8–13.

115 K. Wang, T. Zhao, G. Lian, Q. Yu, C. Luan, Q. Wang and D. Cui, *Sens. Actuators, B*, 2013, **184**, 33–39.

116 P. P. Subha, K. Hasna and M. K. Jayaraj, *Mater. Res. Express*, 2017, **4**, 105037.

117 S. Wang, D. Huang, S. Xu, W. Jiang, T. Wang, J. Hu, N. Hu, Y. Su, Y. Zhang and Z. Yang, *Phys. Chem. Chem. Phys.*, 2017, **19**, 19043–19049.

118 G. H. Mhlongo, K. Shingange, Z. P. Tshabalala, B. P. Dhonge, F. A. Mahmoud, B. W. Mwakikunga and D. E. Motaung, *Appl. Surf. Sci.*, 2016, **390**, 804–815.

119 J. Wang, L. Wei, L. Zhang, J. Zhang, H. Wei, C. Jiang and Y. Zhang, *J. Mater. Chem.*, 2012, **22**, 20038.

120 J. Wang, P. Yang and X. Wei, *ACS Appl. Mater. Interfaces*, 2015, **7**, 3816–3824.

121 P. Chaudhari and S. Mishra, *Measurement*, 2016, **90**, 468–474.

122 J. Zhou, M. Ikram, A. U. Rehman, J. Wang, Y. Zhao, K. Kan, W. Zhang, F. Raziq, L. Li and K. Shi, *Sens. Actuators, B*, 2018, **255**, 1819–1830.

123 M. Kaur, B. K. Dadhich, R. Singh, K. Ganapathi, T. Bagwaiya, S. Bhattacharya, A. K. Debnath, K. P. Muthe and S. C. Gadkari, *Sens. Actuators, B*, 2017, **242**, 389–403.

124 V. Srivastava and K. Jain, *Mater. Lett.*, 2016, **169**, 28–32.

125 P.-G. Su and T.-T. Pan, *Mater. Chem. Phys.*, 2011, **125**, 351–357.

126 H. Zhang, L. Yu, Q. Li, Y. Du and S. Ruan, Sens. Actuators, B, 2017, **241**, 109–115.

127 Z. Li, J. Wang, S. Zhang, S. Yan, B. Cao, W. Shen, Z. Wang and Y. Q. Fu, J. Alloys Compd., 2018, **742**, 712–720.

128 V. Inderan, M. M. Arafat, S. Kumar, A. Haseeb, Z. T. Jiang, M. Altarawneh and H. L. Lee, Nanotechnology, 2017, **28**, 265702.

129 A. U. Rehman, J. Zhang, J. Zhou, K. Kan, L. Li and K. Shi, Microporous Mesoporous Mater., 2017, **240**, 50–56.

130 J. Liang, K. Zhu, R. Yang and M. Hu, Ceram. Int., 2018, **44**, 2261–2268.

131 H. Xu, J. Zhang, A. U. Rehman, L. Gong, K. Kan, L. Li and K. Shi, Appl. Surf. Sci., 2017, **412**, 230–237.

132 D. Liu, L. Lin, Q. Chen, H. Zhou and J. Wu, ACS Sens., 2017, **2**, 1491–1497.

133 Y. Wang, Y. Zhou, C. Meng, Z. Gao, X. Cao, X. Li, L. Xu, W. Zhu, X. Peng, B. Zhang, Y. Lin and L. Liu, Nanotechnology, 2016, **27**, 425503.

134 S. Xu, J. Gao, L. Wang, K. Kan, Y. Xie, P. Shen, L. Li and K. Shi, Nanoscale, 2015, **7**, 14643–14651.

135 Z. Liu, L. Yu, F. Guo, S. Liu, L. Qi, M. Shan and X. Fan, Appl. Surf. Sci., 2017, **423**, 721–727.

136 N. Van Hieu, L. T. B. Thuy and N. D. Chien, Sens. Actuators, B, 2008, **129**, 888–895.

137 N. Tiwale, Mater. Sci. Technol., 2015, **31**, 1681–1697.

138 A. Mirzaei, B. Hashemi and K. Janghorban, J. Mater. Sci.: Mater. Electron., 2015, **27**, 3109–3144.

139 G. Korotcenkov and B. K. Cho, Sens. Actuators, B, 2014, **196**, 80–98.

140 S. Das and V. Jayaraman, Prog. Mater. Sci., 2014, **66**, 112–255.

141 H.-J. Kim and J.-H. Lee, Sens. Actuators, B, 2014, **192**, 607–627.

142 D. R. Miller, S. A. Akbar and P. A. Morris, Sens. Actuators, B, 2014, **204**, 250–272.

143 G. Korotcenkov, V. Brinzari and B. K. Cho, Microchim. Acta, 2016, **183**, 1033–1054.

144 P. Rai, S. M. Majhi, Y.-T. Yu and J.-H. Lee, RSC Adv., 2015, **5**, 76229–76248.

145 S. Gupta Chatterjee, S. Chatterjee, A. K. Ray and A. K. Chakraborty, Sens. Actuators, B, 2015, **221**, 1170–1181.

146 M. Gardon and J. M. Guilemany, J. Mater. Sci.: Mater. Electron., 2012, **24**, 1410–1421.

147 P. T. Moseley, Meas. Sci. Technol., 2017, **28**, 082001.

148 Y. F. Sun, S. B. Liu, F. L. Meng, J. Y. Liu, Z. Jin, L. T. Kong and J. H. Liu, Sensors, 2012, **12**, 2610–2631.

149 H. Gu, Z. Wang and Y. Hu, Sensors, 2012, **12**, 5517–5550.

150 A. Mirzaei, S. G. Leonardi and G. Neri, Ceram. Int., 2016, **42**, 15119–15141.

151 L. Zhu and W. Zeng, Sens. Actuators, A, 2017, **267**, 242–261.

152 A. D. Faisal, Bull. Mater. Sci., 2017, **40**, 1061–1068.

153 N. Zhang, K. Yu, Q. Li, Z. Q. Zhu and Q. Wan, J. Appl. Phys., 2008, **103**, 104305.

154 T. Kondo, Y. Sato, M. Kinoshita, P. Shankar, N. N. Mintcheva, M. Honda, S. Iwamori and S. A. Kulinich, Jpn. J. Appl. Phys., 2017, **56**, 080304.

155 Y. Li, S. Wang, P. Hao, J. Tian, H. Cui and X. Wang, Sens. Actuators, B, 2018, **273**, 751–759.

156 A. Beniwal, P. K. Sahu and S. Sharma, J. Sol–Gel Sci. Technol., 2018, **88**, 322–333.

157 M. Kodu, T. Avarmaa, A. Floren and R. Jaaniso, J. Eur. Ceram. Soc., 2013, **33**, 2335–2340.

158 K. Khun Khun, A. Mahajan and R. K. Bedi, J. Appl. Phys., 2009, **106**, 124509.

159 T. Yang, M. Zhu, K. Gu, C. Zhai, Q. Zhao, X. Yang and M. Zhang, New J. Chem., 2018, **42**, 13612–13618.

160 D. Hanft, M. Bektas and R. Moos, Materials, 2018, **11**, 1342.

161 L. Xu, B. Dong, Y. Wang, X. Bai, Q. Liu and H. Song, Sens. Actuators, B, 2010, **147**, 531–538.

162 T. M. Perfecto, C. A. Zito and D. P. Volanti, CrystEngComm, 2017, **19**, 2733–2738.

163 X. W. Huang, X. B. Zou, J. Y. Shi, J. W. Zhao, Y. Li, L. Hao and J. Zhang, Anal. Chim. Acta, 2013, **787**, 233–238.

164 H. Liu, W. Shen, X. Chen and J.-P. Corriou, J. Mater. Sci.: Mater. Electron., 2018, **29**, 18380–18387.

165 L. Y. Hong and H. N. Lin, Beilstein J. Nanotechnol., 2016, **7**, 1044–1051.

166 Z. P. Tshabalala, K. Shingange, B. P. Dhonge, O. M. Ntwaeaborwa, G. H. Mhlongo and D. E. Motaung, Sens. Actuators, B, 2017, **238**, 402–419.

167 P. M. Perillo and D. F. Rodríguez, Sens. Actuators, B, 2014, **193**, 263–266.

168 B. C. Yadav, S. Singh and A. Yadav, Appl. Surf. Sci., 2011, **257**, 1960–1966.

169 X. Song, Q. Xu, T. Zhang, B. Song, C. Li and B. Cao, Sens. Actuators, B, 2018, **268**, 170–181.

170 Y. X. Li, Z. X. Song, F. Jiang, Q. Sun, F. Ma, H. R. Wang and K. Chen, Ceram. Int., 2016, **42**, 18318–18323.

171 J. Liang, W. Li, J. Liu and M. Hu, J. Alloys Compd., 2016, **687**, 845–854.

172 C. A. Zito, T. M. Perfecto and D. P. Volanti, New J. Chem., 2018, **42**, 15954–15961.

173 T.-R. Rashid, D.-T. Phan and G.-S. Chung, Sens. Actuators, B, 2013, **185**, 777–784.

174 P. Dhivya, A. K. Prasad and M. Sridharan, Ceram. Int., 2014, **40**, 409–415.

175 S. A. Hakim, Y. Liu, G. S. Zakharova and W. Chen, RSC Adv., 2015, **5**, 23489–23497.

176 S. Lin, D. Li, J. Wu, X. Li and S. A. Akbar, Sens. Actuators, B, 2011, **156**, 505–509.

177 B. Zhang, M. Li, Z. Song, H. Kan, H. Yu, Q. Liu, G. Zhang and H. Liu, Sens. Actuators, B, 2017, **249**, 558–563.

178 W. Ponhan, S. Phadungdhitidhada and S. Choopun, Mater. Today, 2017, **4**, 6342–6348.

179 M. Thepnurat, T. Chairuangsri, N. Hongsith, P. Ruankham and S. Choopun, ACS Appl. Mater. Interfaces, 2015, **7**, 24177–24184.

180 P. Shankar and J. B. B. Rayappan, J. Mater. Chem. C, 2017, **5**, 10869–10880.

181 N. Van Quy, V. A. Minh, N. Van Luan, V. N. Hung and N. Van Hieu, Sens. Actuators, B, 2011, **153**, 188–193.

182 G. K. Mani and J. B. B. Rayappan, Sens. Actuators, B, 2013, **183**, 459–466.

183 X. Pan, X. Zhao, J. Chen, A. Bermak and Z. Fan, Sens. Actuators, B, 2015, **206**, 764–771.

184 V. P. Verma, S. Das, S. Hwang, H. Choi, M. Jeon and W. Choi, *Mater. Sci. Eng., B*, 2010, **171**, 45–49.

185 X. Pan and X. Zhao, *Sensors*, 2015, **15**, 8919–8930.

186 O. Lupan, G. Chai and L. Chow, *Microelectron. J.*, 2007, **38**, 1211–1216.

187 O. Lupan, G. Chai and L. Chow, *Microelectron. Eng.*, 2008, **85**, 2220–2225.

188 B.-R. Huang and J.-C. Lin, *Appl. Surf. Sci.*, 2013, **280**, 945–949.

189 K. Vijayalakshmi and D. Gopalakrishna, *J. Mater. Sci.: Mater. Electron.*, 2014, **25**, 2253–2260.

190 Y. T. Lim, J. Y. Son and J. S. Rhee, *Ceram. Int.*, 2013, **39**, 887–890.

191 J. J. Hassan, M. A. Mahdi, C. W. Chin, H. Abu-Hassan and Z. Hassan, *Sens. Actuators, B*, 2013, **176**, 360–367.

192 S. Yang, Z. Wang, Z. Hu, X. Luo, J. Lei, D. Zhou, L. Fei, Y. Wang and H. Gu, *ACS Appl. Mater. Interfaces*, 2015, **7**, 9247–9253.

193 I. H. Kadhim and H. Abu Hassan, *J. Electron. Mater.*, 2016, **46**, 1419–1426.

194 M. Belaqziz, M. b. Amjoud, A. Gaddari, B. Rhouta and D. Mezzane, *Superlattice Microstruct.*, 2014, **71**, 185–189.

195 A. Kaur Bal, A. Singh and R. K. Bedi, *Phys. B*, 2010, **405**, 3124–3128.

196 X. Mu, C. Chen, L. Han, B. Shao, Y. Wei, Q. Liu and P. Zhu, *J. Alloys Compd.*, 2015, **637**, 55–61.

197 L. Yanxiao, Z. Xiao-bo, H. Xiao-wei, S. Ji-yong, Z. Jie-wen, M. Holmes and L. Hao, *Biosens. Bioelectron.*, 2015, **67**, 35–41.

198 J. Wang, Z. Li, S. Zhang, S. Yan, B. Cao, Z. Wang and Y. Fu, *Sens. Actuators, B*, 2018, **255**, 862–870.

199 Z. Li, S. Yan, S. Zhang, J. Wang, W. Shen, Z. Wang and Y. Q. Fu, *J. Alloys Compd.*, 2019, **770**, 721–731.

200 C. Zhang, X. Geng, H. Liao, C.-J. Li and M. Debliquy, *Sens. Actuators, B*, 2017, **242**, 102–111.

201 R. Chen, J. Wang and L. Xiang, *Sens. Actuators, B*, 2018, **270**, 207–215.

202 Y. Wu, M. Hu and Y. Tian, *Chin. Phys. B*, 2017, **26**, 020701.

203 V. Annapureddy, Y. Kim, G.-T. Hwang, H. W. Jang, S.-D. Kim, J.-J. Choi, B. Cho and J. Ryu, *Adv. Mater. Interfaces*, 2018, **5**, 1700811.

204 L. Han, C. Chen, Y. Wei, B. Shao, X. Mu, Q. Liu and P. Zhu, *J. Alloys Compd.*, 2016, **656**, 326–331.

205 M. Hu, D.-L. Jia, Q.-L. Liu, M.-D. Li and P. Sun, *Chin. Phys. B*, 2013, **22**, 068204.

206 W. Liu, L. Xu, K. Sheng, C. Chen, X. Zhou, B. Dong, X. Bai, S. Zhang, G. Lu and H. Song, *J. Mater. Chem. A*, 2018, **6**, 10976–10989.

207 S. S. Kim, H. G. Na, Y. J. Kwon, H. Y. Cho and H. W. Kim, *Met. Mater. Int.*, 2015, **21**, 415–421.

208 X. Gou, R. Li, G. Wang, Z. Chen and D. Wexler, *Nanotechnology*, 2009, **20**, 495501.

209 S. Bai, Y. Ma, X. Shu, J. Sun, Y. Feng, R. Luo, D. Li and A. Chen, *Ind. Eng. Chem. Res.*, 2017, **56**, 2616–2623.

210 A. Wei, Z. Wang, L.-H. Pan, W.-W. Li, L. Xiong, X.-C. Dong and W. Huang, *Chin. Phys. Lett.*, 2011, **28**, 080702.

211 H. Abdollahi, M. Samkan and M. M. Hashemi, *Microsyst. Technol.*, 2018, **24**, 3741–3749.

212 R. S. Ganesh, G. K. Mani, R. Elayaraja, E. Durgadevi, M. Navaneethan, S. Ponnusamy, K. Tsuchiya, C. Muthamizhchelvan and Y. Hayakawa, *Appl. Surf. Sci.*, 2018, **449**, 314–321.

213 A. El Bouari, A. Gaddari, M. Amjoud, F. Berger, J. B. Sanchez, M. Lahcini, B. Rhouta, D. Mezzane, C. Mavon, R. El Ouatib, H. Hannache, S. Krimi, M. Lamire, I. Mansouri, R. Moussa and A. Aboulayt, *MATEC Web of Conferences*, 2013, **5**, 04010.

214 Y. Xiong, W. Xu, D. Ding, W. Lu, L. Zhu, Z. Zhu, Y. Wang and Q. Xue, *J. Hazard. Mater.*, 2018, **341**, 159–167.

215 S. Yang, Y. Liu, W. Jin, Y. Qi, G. S. Zakharova and W. Chen, *Ferroelectrics*, 2015, **477**, 112–120.

216 Y. Xiong, Z. Zhu, T. Guo, H. Li and Q. Xue, *J. Hazard. Mater.*, 2018, **353**, 290–299.

217 E. Zampetti, A. Macagnano and A. Bearzotti, *J. Nanopart. Res.*, 2013, **15**, 1566.

218 C. Shao, Y. Chang and Y. Long, *Sens. Actuators, B*, 2014, **204**, 666–672.

219 M. Chitra, K. Uthayarani, N. Rajasekaran, N. Neelakandeswari, E. K. Girija and D. P. Padiyan, *Chin. Phys. Lett.*, 2015, **32**, 078101.

220 E. Wongrat, W. Ponhan and S. Choopun, *Ceram. Int.*, 2017, **43**, S520–S524.

221 L. Hou, C.-M. Zhang, P. Ma, L. Li, K.-K. Zhu, X.-F. Kang and W. Chen, *Chin. J. Anal. Chem.*, 2018, **46**, E1854–E1862.

222 A. P. Sharma, P. Dhakal, D. K. Pradhan, M. K. Behera, B. Xiao and M. Bahoura, *AIP Adv.*, 2018, **8**, 095219.

223 B. Sakthivel, L. Manjakkal and G. Nammalvar, *IEEE Sens. J.*, 2017, **17**, 6529–6536.

224 N. S. Ramgir, S. K. Ganapathi, M. Kaur, N. Datta, K. P. Muthe, D. K. Aswal, S. K. Gupta and J. V. Yakhmi, *Sens. Actuators, B*, 2010, **151**, 90–96.

225 Z. Li, J. Wang, N. Wang, S. Yan, W. Liu, Y. Q. Fu and Z. Wang, *J. Alloys Compd.*, 2017, **725**, 1136–1143.

226 J. Zhang, D. Zeng, Q. Zhu, J. Wu, K. Xu, T. Liao, G. Zhang and C. Xie, *J. Phys. Chem. C*, 2015, **119**, 17930–17939.

227 J. Zhou, M. Ikram, A. U. Rehman, J. Wang, Y. Zhao, K. Kan, W. Zhang, F. Raziq, L. Li and K. Shi, *Sens. Actuators, B*, 2018, **255**, 1819–1830.

228 I. Singh and R. K. Bedi, *Solid State Sci.*, 2011, **13**, 2011–2018.

229 S. Li, M. Wang, C. Li, J. Liu, M. Xu, J. Liu and J. Zhang, *Sci. China Mater.*, 2018, **61**, 1085–1094.

230 D. N. Oosthuizen, D. E. Motaung and H. C. Swart, *Sens. Actuators, B*, 2018, **266**, 761–772.

231 Z. Wang, F. Li, H. Wang, A. Wang and S. Wu, *J. Mater. Sci.: Mater. Electron.*, 2018, **29**, 16654–16659.

232 S. Wang, D. Huang, S. Xu, W. Jiang, T. Wang, J. Hu, N. Hu, Y. Su, Y. Zhang and Z. Yang, *Phys. Chem. Chem. Phys.*, 2017, **19**, 19043–19049.

233 J. Wang, L. Wei, L. Zhang, J. Zhang, H. Wei, C. Jiang and Y. Zhang, *J. Mater. Chem.*, 2012, **22**, 20038–20047.

234 B. Geng, F. Zhan, C. Fang and N. Yu, *J. Mater. Chem.*, 2008, **18**, 4977–4984.

235 X. Zhang, J. Wang, L. Xuan, Z. Zhu, Q. Pan, K. Shi and G. Zhang, *J. Alloys Compd.*, 2018, **768**, 190–197.

236 S. Li, F.-L. Li, S.-M. Zhou, P. Wang, K. Cheng and Z.-L. Du, *Chin. Phys. B*, 2009, **18**, 3985–3989.

237 H. Liu, X. Du, X. Xing, G. Wang and S. Z. Qiao, *Chem. Commun.*, 2012, **48**, 865–867.

238 W. Zhang, C. Zeng, M. Kong, Y. Pan and Z. Yang, *Sens. Actuators, B*, 2012, **162**, 292–299.

239 R. Kumar, R. Kumar, N. Kushwaha and J. Mittal, *IEEE Sens. J.*, 2016, **16**, 4691–4695.

240 S. Balamurugan, A. Rajalakshmi and D. Balamurugan, *J. Alloys Compd.*, 2015, **650**, 863–870.

241 Y. Wang, B. Liu, D. Cai, H. Li, Y. Liu, D. Wang, L. Wang, Q. Li and T. Wang, *Sens. Actuators, B*, 2014, **201**, 351–359.

242 N. S. Ramgir, P. K. Sharma, N. Datta, M. Kaur, A. K. Debnath, D. K. Aswal and S. K. Gupta, *Sens. Actuators, B*, 2013, **186**, 718–726.

243 Q. A. Drmosh, Z. H. Yamani, A. K. Mohamedkhair, A. H. Y. Hendi, M. K. Hossain and A. Ibrahim, *Mater. Lett.*, 2018, **214**, 283–286.

244 H. Fu, C. Hou, F. Gu, D. Han and Z. Wang, *Sens. Actuators, B*, 2017, **243**, 516–524.

245 D. Naberezhnyi, M. Rumyantseva, D. Filatova, M. Batuk, J. Hadermann, A. Baranchikov, N. Khmelevsky, A. Aksenenko, E. Konstantinova and A. Gaskov, *Nanomaterials*, 2018, **8**, 801.

246 A. N. A. Anasthasiya, R. K. Kampara, P. K. Rai and B. G. Jeyaprakash, *Appl. Surf. Sci.*, 2018, **449**, 244–249.

247 Z. Zhu, C.-T. Kao and R.-J. Wu, *Appl. Surf. Sci.*, 2014, **320**, 348–355.

248 S. Yan, Z. Li, H. Li, Z. Wu, J. Wang, W. Shen and Y. Q. Fu, *J. Mater. Sci.*, 2018, **53**, 16331–16344.

249 S. C. Wang and M. O. Shaikh, *Sensors*, 2015, **15**, 14286–14297.

250 Q. A. Drmosh, Z. H. Yamani, A. K. Mohamedkhair, A. H. Y. Hendi and A. Ibrahim, *Vacuum*, 2018, **156**, 68–77.

251 L. Chandra, P. K. Sahu, R. Dwivedi and V. N. Mishra, *Mater. Res. Express*, 2017, **4**, 125017.

252 O. Lupan, V. Postica, F. Labat, I. Ciofini, T. Pauporté and R. Adelung, *Sens. Actuators, B*, 2018, **254**, 1259–1270.

253 J. M. Lee, J.-e. Park, S. Kim, S. Kim, E. Lee, S.-J. Kim and W. Lee, *Int. J. Hydrogen Energy*, 2010, **35**, 12568–12573.

254 K. Vijayalakshmi, A. Renitta and A. Monamary, *J. Mater. Sci.: Mater. Electron.*, 2018, **29**, 21023–21032.

255 X. Wei, X. Yang, T. Wu, S. Wu, W. Li, X. Wang and Z. Chen, *Int. J. Hydrogen Energy*, 2017, **42**, 24580–24586.

256 W. Lu, D. Ding, Q. Xue, Y. Du, Y. Xiong, J. Zhang, X. Pan and W. Xing, *Sens. Actuators, B*, 2018, **254**, 393–401.

257 Z. S. Hosseini, A. Mortezaali, A. Iraji zad and S. Fardindoost, *J. Alloys Compd.*, 2015, **628**, 222–229.

258 F.-C. Chung, Z. Zhu, P.-Y. Luo, R.-J. Wu and W. Li, *Sens. Actuators, B*, 2014, **199**, 314–319.

259 Z. Zhu, J.-L. Chang and R.-J. Wu, *Sens. Actuators, B*, 2015, **214**, 56–62.

260 H. Wu, H. Huang, J. Zhou, D. Hong, M. Ikram, A. U. Rehman, L. Li and K. Shi, *Sci. Rep.*, 2017, **7**, 14688.

261 J. Liang, J. Liu, W. Li and M. Hu, *Mater. Res. Bull.*, 2016, **84**, 332–339.

262 J. Liang, W. Li, J. Liu and M. Hu, *Mater. Lett.*, 2016, **184**, 92–95.

263 S. Park, H. Kim, C. Jin and C. Lee, *J. Korean Phys. Soc.*, 2012, **60**, 1560–1564.

264 T.-R. Rashid, D.-T. Phan and G.-S. Chung, *Sens. Actuators, B*, 2014, **193**, 869–876.

265 S. Ren, G. Fan, S. Qu and Q. Wang, *J. Appl. Phys.*, 2011, **110**, 084312.

266 Z. Wang, Z. Li, T. Jiang, X. Xu and C. Wang, *ACS Appl. Mater. Interfaces*, 2013, **5**, 2013–2021.

267 W. P. Chen, Y. Xiong, Y. S. Li, P. Cui, S. S. Guo, W. Chen, Z. L. Tang, Z. Yan and Z. Zhang, *Int. J. Hydrogen Energy*, 2016, **41**, 3307–3312.

268 B. Liu, D. Cai, Y. Liu, D. Wang, L. Wang, Y. Wang, H. Li, Q. Li and T. Wang, *Sens. Actuators, B*, 2014, **193**, 28–34.

269 P. Li, Z. Xiong, S. Zhu, M. Wang, Y. Hu, H. Gu, Y. Wang and W. Chen, *Int. J. Hydrogen Energy*, 2017, **42**, 30186–30192.

270 B. Huang, Y. Wang, Q. Hu, X. Mu, Y. Zhang, J. Bai, Q. Wang, Y. Sheng, Z. Zhang and E. Xie, *J. Mater. Chem. C*, 2018, **6**, 10935–10943.

271 M. Chitra, K. Uthayarani, N. Rajasekaran, N. Neelakandeswari, E. K. Girija and D. P. Padiyan, *Surf. Rev. Lett.*, 2016, **23**, 1550094.

272 L. Yang, L. Li, Y. Yang, G. Zhang, L. Gong, L. Jing, H. Fu and K. Shi, *Mater. Res. Bull.*, 2013, **48**, 3657–3665.

273 S. Jain, A. Patrike, S. S. Badadhe, M. Bhardwaj and S. Ogale, *ACS Omega*, 2018, **3**, 1977–1982.

274 N. Singh, C. Yan and P. S. Lee, *Sens. Actuators, B*, 2010, **150**, 19–24.

275 H. Ahn, Y. Wang, S. Hyun Jee, M. Park, Y. S. Yoon and D.-J. Kim, *Chem. Phys. Lett.*, 2011, **511**, 331–335.

276 M. R. Modaberi, R. Rooydell, S. Brahma, A. A. Akande, B. W. Mwakikunga and C.-P. Liu, *Sens. Actuators, B*, 2018, **273**, 1278–1290.

277 C. Stella, D. Prabhakar, M. Prabhu, N. Soundararajan and K. Ramachandran, *J. Mater. Sci.: Mater. Electron.*, 2015, **27**, 1636–1644.

278 Z. Li, A. A. Haidry, T. Wang and Z. J. Yao, *Appl. Phys. Lett.*, 2017, **111**, 032104.

279 A. Renitta and K. Vijayalakshmi, *Catal. Commun.*, 2016, **73**, 58–62.

280 K. Karthick, D. Srinivasan and J. B. Christopher, *J. Mater. Sci.: Mater. Electron.*, 2017, **28**, 11979–11986.

281 J. Ma, J. Liu, H. Zhang, P. Ai, N. Gong, Y. Wu and D. Yu, *Sens. Actuators, B*, 2015, **216**, 72–79.

282 X. Zou, H. Fan, Y. Tian, M. Zhang and X. Yan, *Dalton Trans.*, 2015, **44**, 7811–7821.

283 A. J. Kulandaisamy, J. R. Reddy, P. Srinivasan, K. J. Babu, G. K. Mani, P. Shankar and J. B. B. Rayappan, *J. Alloys Compd.*, 2016, **688**, 422–429.

284 K. Khun Khun, A. Mahajan and R. K. Bedi, *Chem. Phys. Lett.*, 2010, **492**, 119–122.

285 J. M. Wu, *Nanotechnology*, 2010, **21**, 235501.

286 T. Pauporte, O. Lupan, V. Postica, M. Hoppe, L. Chow and R. Adelung, *Phys. Status Solidi A*, 2018, **215**, 1700824.

287 R. Jaisutti, M. Lee, J. Kim, S. Choi, T. J. Ha, J. Kim, H. Kim, S. K. Park and Y. H. Kim, *ACS Appl. Mater. Interfaces*, 2017, **9**, 8796–8804.

288 K. Vijayalakshmi and K. Karthick, *Int. J. Hydrogen Energy*, 2014, **39**, 7165–7172.

289 H. Liu, D. Ding, C. Ning and Z. Li, *Nanotechnology*, 2012, **23**, 015502.

290 M. Kaur, S. Bhattacharya, M. Roy, S. K. Deshpande, P. Sharma, S. K. Gupta and J. V. Yakhmi, *Appl. Phys. A: Mater. Sci. Process.*, 2007, **87**, 91–96.

291 A. Chaparadza and S. B. Rananavare, *Nanotechnology*, 2008, **19**, 245501.

292 H. Tang, M. Yan, H. Zhang, S. Li, X. Ma, M. Wang and D. Yang, *Sens. Actuators, B*, 2006, **114**, 910–915.

293 P. M. Calaque, C. J. Vergara, L. I. Ballesteros and A. Somintac, *AIP Conf. Proc.*, 2017, **1808**, 020013.

294 T.-t. Li, R.-r. Zheng, H. Yu, L. Xia, Y. Yang and X.-t. Dong, *Solid State Ionics*, 2018, **325**, 17–23.

295 M. Bao, Y. Chen, F. Li, J. Ma, T. Lv, Y. Tang, L. Chen, Z. Xu and T. Wang, *Nanoscale*, 2014, **6**, 4063–4066.

296 G. Cui, P. Zhang, L. Chen, X. Wang, J. Li, C. Shi and D. Wang, *Sci. Rep.*, 2017, **7**, 43887.

297 C. Jiang, S. Xu, G. Zhang, L. Li, Y. Yang and K. Shi, *CrystEngComm*, 2013, **15**, 2482.

298 D. R. Patil, L. A. Patil and P. P. Patil, *Sens. Actuators, B*, 2007, **126**, 368–374.

299 S. Bhuvaneshwari, S. Papachan and N. Gopalakrishnan, *AIP Conf. Proc.*, 2017, **1832**, 050126.

300 J. Zhang, D. Zeng, Q. Zhu, J. Wu, Q. Huang, W. Zhang and C. Xie, *Phys. Chem. Chem. Phys.*, 2016, **18**, 5386–5396.

301 H. Wu, K. Kan, L. Wang, G. Zhang, Y. Yang, H. Li, L. Jing, P. Shen, L. Li and K. Shi, *CrystEngComm*, 2014, **16**, 9116–9124.

302 R. Lu, W. Zhou, K. Shi, Y. Yang, L. Wang, K. Pan, C. Tian, Z. Ren and H. Fu, *Nanoscale*, 2013, **5**, 8569–8576.

303 X. Yue, T. Hong, Z. Yang and S. Huang, *Chin. Sci. Bull.*, 2012, **58**, 821–826.

304 X. Liu, B. Du, Y. Sun, M. Yu, Y. Yin, W. Tang, C. Chen, L. Sun, B. Yang, W. Cao and M. N. Ashfold, *ACS Appl. Mater. Interfaces*, 2016, **8**, 16379–16385.

305 W. Zang, Y. Nie, D. Zhu, P. Deng, L. Xing and X. Xue, *J. Phys. Chem. C*, 2014, **118**, 9209–9216.

306 L. A. Patil and D. R. Patil, *Sens. Actuators, B*, 2006, **120**, 316–323.

307 A. Mirzaei, G.-J. Sun, J. K. Lee, C. Lee, S. Choi and H. W. Kim, *Ceram. Int.*, 2017, **43**, 5247–5254.

308 S. Park, H. Kheel, G.-J. Sun, H. W. Kim, T. Ko and C. Lee, *Met. Mater. Int.*, 2016, **22**, 730–736.

309 M.-R. Yu, G. Suyambrakasam, R.-J. Wu and M. Chavali, *Mater. Res. Bull.*, 2012, **47**, 1713–1718.

310 J. Liang, R. Yang, K. Zhu and M. Hu, *J. Mater. Sci.: Mater. Electron.*, 2017, **29**, 3780–3789.

311 L. F. da Silva, J. C. M'Peko, A. C. Catto, S. Bernardini, V. R. Mastelaro, K. Aguir, C. Ribeiro and E. Longo, *Sens. Actuators, B*, 2017, **240**, 573–579.

312 D. R. Patil and L. A. Patil, *Sens. Actuators, B*, 2007, **123**, 546–553.

313 D. Zhu, Y. Fu, W. Zang, Y. Zhao, L. Xing and X. Xue, *Mater. Lett.*, 2016, **166**, 288–291.

314 G. Lu, L. E. Ocola and J. Chen, *Nanotechnology*, 2009, **20**, 445502.

315 Y. Wang and S. Gong, *J. Mater. Sci.: Mater. Electron.*, 2015, **26**, 5024–5029.

316 W. Yang, P. Wan, X. Zhou, J. Hu, Y. Guan and L. Feng, *ACS Appl. Mater. Interfaces*, 2014, **6**, 21093–21100.

317 S. Liu, B. Yu, H. Zhang, T. Fei and T. Zhang, *Sens. Actuators, B*, 2014, **202**, 272–278.

318 H. Tai, Z. Yuan, W. Zheng, Z. Ye, C. Liu and X. Du, *Nanoscale Res. Lett.*, 2016, **11**, 130.

319 Y. Yang, L. Sun, X. Dong, H. Yu, T. Wang, J. Wang, R. Wang, W. Yu and G. Liu, *RSC Adv.*, 2016, **6**, 37085–37092.

320 R. Ghosh, A. K. Nayak, S. Santra, D. Pradhan and P. K. Guha, *RSC Adv.*, 2015, **5**, 50165–50173.

321 S. Liu, Z. Wang, Y. Zhang, J. Li and T. Zhang, *Sens. Actuators, B*, 2016, **228**, 134–143.

322 Z. Wang, Y. Zhang, S. Liu and T. Zhang, *Sens. Actuators, B*, 2016, **222**, 893–903.

323 Z. Wang, T. Zhang, C. Zhao, T. Han, T. Fei, S. Liu and G. Lu, *J. Colloid Interface Sci.*, 2018, **514**, 599–608.

324 M. Shojaee, S. Nasresfahani and M. H. Sheikhi, *Sens. Actuators, B*, 2018, **254**, 457–467.

325 T. Wang, J. Hao, S. Zheng, Q. Sun, D. Zhang and Y. Wang, *Nano Res.*, 2017, **11**, 791–803.

326 J. Zhang, J. Wu, X. Wang, D. Zeng and C. Xie, *Sens. Actuators, B*, 2017, **243**, 1010–1019.

327 P.-G. Su, F.-Y. Chen and C.-H. Wei, *Sens. Actuators, B*, 2018, **254**, 1125–1132.

328 J. Zhang, D. Zeng, S. Zhao, J. Wu, K. Xu, Q. Zhu, G. Zhang and C. Xie, *Phys. Chem. Chem. Phys.*, 2015, **17**, 14903–14911.

329 Z. Wang, Y. Zhang, S. Liu and T. Zhang, *Sens. Actuators, B*, 2016, **222**, 893–903.

330 Z. Wang, T. Zhang, T. Han, T. Fei, S. Liu and G. Lu, *Sens. Actuators, B*, 2018, **266**, 812–822.

331 J. Pan, W. Li, L. Quan, N. Han, S. Bai, R. Luo, Y. Feng, D. Li and A. Chen, *Ind. Eng. Chem. Res.*, 2018, **57**, 10086–10094.

332 X. Liu, J. Sun and X. Zhang, *Sens. Actuators, B*, 2015, **211**, 220–226.

333 N. Chen, X. Li, X. Wang, J. Yu, J. Wang, Z. Tang and S. A. Akbar, *Sens. Actuators, B*, 2013, **188**, 902–908.

334 F. Gu, R. Nie, D. Han and Z. Wang, *Sens. Actuators, B*, 2015, **219**, 94–99.

335 Z. Li, Y. Liu, D. Guo, J. Guo and Y. Su, *Sens. Actuators, B*, 2018, **271**, 306–310.

336 S. Liu, Z. Wang, Y. Zhang, J. Li and T. Zhang, *Sens. Actuators, B*, 2016, **228**, 134–143.

337 X. Jiang, H. Tai, Z. Ye, Z. Yuan, C. Liu, Y. Su and Y. Jiang, *Mater. Lett.*, 2017, **186**, 49–52.

338 D. Zhang, J. Liu and B. Xia, *J. Electron. Mater.*, 2016, **45**, 4324–4330.

339 X. Liu, J. Li, J. Sun and X. Zhang, *RSC Adv.*, 2015, **5**, 73699–73704.

340 Y. Xia, J. Wang, J. L. Xu, X. Li, D. Xie, L. Xiang and S. Komarneni, *ACS Appl. Mater. Interfaces*, 2016, **8**, 35454–35463.

341 T. Wang, J. Hao, S. Zheng, Q. Sun, D. Zhang and Y. Wang, *Nano Res.*, 2018, **11**, 791–803.

342 Y.-l. Dong, X.-f. Zhang, X.-l. Cheng, Y.-m. Xu, S. Gao, H. Zhao and L.-h. Huo, *RSC Adv.*, 2014, **4**, 57493–57500.

343 W. Fang, Y. Yang, H. Yu, X. Dong, R. Wang, T. Wang, J. Wang, Z. Liu, B. Zhao and X. Wang, *New J. Chem.*, 2017, **41**, 7517–7523.

344 Y. Yang, C. Tian, L. Sun, R. Lü, W. Zhou, K. Shi, K. Kan, J. Wang and H. Fu, *J. Mater. Chem. A*, 2013, **1**, 12742.

345 Y. Yang, C. Tian, J. Wang, L. Sun, K. Shi, W. Zhou and H. Fu, *Nanoscale*, 2014, **6**, 7369–7378.

346 G. P. Evans, M. J. Powell, I. D. Johnson, D. P. Howard, D. Bauer, J. A. Darr and I. P. Parkin, *Sens. Actuators, B*, 2018, **255**, 1119–1129.

347 Y. Chen, W. Zhang and Q. Wu, *Sens. Actuators, B*, 2017, **242**, 1216–1226.

348 H. Meng, W. Yang, K. Ding, L. Feng and Y. Guan, *J. Mater. Chem. A*, 2015, **3**, 1174–1181.

349 X. Li, Y. Zhao, X. Wang, J. Wang, A. M. Gaskov and S. A. Akbar, *Sens. Actuators, B*, 2016, **230**, 330–336.

350 P.-G. Su and L.-Y. Yang, *Sens. Actuators, B*, 2016, **223**, 202–208.

351 P.-G. Su, F.-Y. Chen and C.-H. Wei, *Sens. Actuators, B*, 2018, **254**, 1125–1132.

352 G. Singh, A. Choudhary, D. Haranath, A. G. Joshi, N. Singh, S. Singh and R. Pasricha, *Carbon*, 2012, **50**, 385–394.

353 R. Kumar, N. Kushwaha and J. Mittal, *Sens. Actuators, B*, 2017, **244**, 243–251.

354 F. Schutt, V. Postica, R. Adelung and O. Lupan, *ACS Appl. Mater. Interfaces*, 2017, **9**, 23107–23118.

355 A. Yang, X. Tao, R. Wang, S. Lee and C. Surya, *Appl. Phys. Lett.*, 2007, **91**, 133110.

356 D. Zhang, C. Jiang, J. Liu and Y. Cao, *Sens. Actuators, B*, 2017, **247**, 875–882.

357 M. Shojaee, S. Nasresfahani and M. H. Sheikhi, *Sens. Actuators, B*, 2018, **254**, 457–467.

358 N. Du, H. Zhang, X. Ma and D. Yang, *Chem. Commun.*, 2008, 6182–6184.

359 S. Dhall and N. Jaggi, *Sens. Actuators, B*, 2015, **210**, 742–747.

360 D. Zhang, N. Yin, C. Jiang and B. Xia, *J. Mater. Sci.: Mater. Electron.*, 2016, **28**, 2763–2768.

361 D. Kathiravan, B. R. Huang and A. Saravanan, *ACS Appl. Mater. Interfaces*, 2017, **9**, 12064–12072.

362 Y. Peng, L. Zheng, K. Zou and C. Li, *Nanotechnology*, 2017, **28**, 215501.

363 Z. Ye, H. Tai, T. Xie, Z. Yuan, C. Liu and Y. Jiang, *Sens. Actuators, B*, 2016, **223**, 149–156.

364 Z. Bo, M. Yuan, S. Mao, X. Chen, J. Yan and K. Cen, *Sens. Actuators, B*, 2018, **256**, 1011–1020.

365 S. Ghosal and P. Bhattacharyya, *Microelectron. Reliab.*, 2017, **78**, 299–306.

366 D. Acharyya and P. Bhattacharyya, *IEEE Electron Device Lett.*, 2016, **37**, 656–659.

367 S. Nasresfahani, M. H. Sheikhi, M. Tohidi and A. Zarifkar, *IEEE Iranian Conference on Electrical Engineering*, 2016, 1014–1018.

368 D. Zhang, A. Liu, H. Chang and B. Xia, *RSC Adv.*, 2015, **5**, 3016–3022.

369 D. Zhang, Y. e. Sun and Y. Zhang, *J. Mater. Sci.: Mater. Electron.*, 2015, **26**, 7445–7451.

370 S. G. Chatterjee, S. Dey, D. Samanta, S. Santra, S. Chatterjee, P. K. Guha and A. K. Chakraborty, *J. Mater. Sci.: Mater. Electron.*, 2018, **29**, 20162–20171.

371 J. Hu, C. Zou, Y. Su, M. Li, X. Ye, B. Cai, E. S.-W. Kong, Z. Yang and Y. Zhang, *Sens. Actuators, B*, 2018, **270**, 119–129.

372 D. Ding, Q. Xue, W. Lu, Y. Xiong, J. Zhang, X. Pan and B. Tao, *Sens. Actuators, B*, 2018, **259**, 289–298.

373 B.-Y. Wei, M.-C. Hsu, P.-G. Su, H.-M. Lin, R.-J. Wu and H.-J. Lai, *Sens. Actuators, B*, 2004, **101**, 81–89.

374 G. Lu, L. E. Ocola and J. Chen, *Adv. Mater.*, 2009, **21**, 2487–2491.

375 R. Leghrib, A. Felten, J. J. Pireaux and E. Llobet, *Thin Solid Films*, 2011, **520**, 966–970.

376 X. Luo, H. Giessen, Y. Zhou, G. Xie, T. Xie, T. Kang and Y. Jiang, *Proc. SPIE*, 2014, **9285**, 928509.

377 A. Sharma, M. Tomar and V. Gupta, *J. Mater. Chem.*, 2012, **22**, 23608.

378 M. Asad and M. H. Sheikhi, *Sens. Actuators, B*, 2016, **231**, 474–483.

379 H. Liu, W. Zhang, H. Yu, L. Gao, Z. Song, S. Xu, M. Li, Y. Wang, H. Song and J. Tang, *ACS Appl. Mater. Interfaces*, 2016, **8**, 840–846.

380 K. Anothainart, M. Burgmair, A. Karthigeyan, M. Zimmer and I. Eisele, *Sens. Actuators, B*, 2003, **93**, 580–584.

381 L. Meng, Q. Xu, Z. Sun, G. Li, S. Bai, Z. Wang and Y. Qin, *Mater. Lett.*, 2018, **212**, 296–298.

382 P. Wang, Y. Fu, B. Yu, Y. Zhao, L. Xing and X. Xue, *J. Mater. Chem. A*, 2015, **3**, 3529–3535.

383 L. Peng, Q. Zhao, D. Wang, J. Zhai, P. Wang, S. Pang and T. Xie, *Sens. Actuators, B*, 2009, **136**, 80–85.

384 J. Cui, L. Shi, T. Xie, D. Wang and Y. Lin, *Sens. Actuators, B*, 2016, **227**, 220–226.

385 L. Vogel, R. Wagner, R. Moos and D. Schoenauer-Kamin, *Funct. Mater. Lett.*, 2018, **11**, 1850087.

386 N. D. Chinh, N. D. Quang, H. Lee, T. Thi Hien, N. M. Hieu, D. Kim, C. Kim and D. Kim, *Sci. Rep.*, 2016, **6**, 35066.

387 D. Klaus, D. Klawinski, S. Amrehn, M. Tiemann and T. Wagner, *Sens. Actuators, B*, 2015, **217**, 181–185.

388 X. Li, X. Li, J. Wang and S. Lin, *Sens. Actuators, B*, 2015, **219**, 158–163.

389 T. Xie, N. Sullivan, K. Steffens, B. Wen, G. Liu, R. Debnath, A. Davydov, R. Gomez and A. Motayed, *J. Alloys Compd.*, 2015, **653**, 255–259.

390 J. D. Prades, R. Jimenez-Diaz, F. Hernandez-Ramirez, S. Barth, A. Cirera, A. Romano-Rodriguez, S. Mathur and J. R. Morante, *Sens. Actuators, B*, 2009, **140**, 337–341.

391 Y. Xiong, W. Lu, D. Ding, L. Zhu, X. Li, C. Ling and Q. Xue, *ACS Sens.*, 2017, **2**, 679–686.

392 H. Chen, Y. Liu, C. Xie, J. Wu, D. Zeng and Y. Liao, *Ceram. Int.*, 2012, **38**, 503–509.

393 R. Gao, Z. Ying, W. Sheng and P. Zheng, *Mater. Lett.*, 2018, **229**, 210–212.

394 J. Sun, J. Xu, Y. Yu, P. Sun, F. Liu and G. Lu, *Sens. Actuators, B*, 2012, **169**, 291–296.

395 G. Lu, J. Xu, J. Sun, Y. Yu, Y. Zhang and F. Liu, *Sens. Actuators, B*, 2012, **162**, 82–88.

396 J. Cui, D. Wang, T. Xie and Y. Lin, *Sens. Actuators, B*, 2013, **186**, 165–171.

397 X. Li, N. Chen, S. Lin, J. Wang and J. Zhang, *Sens. Actuators, B*, 2015, **209**, 729–734.

398 X. Geng, C. Zhang, Y. Luo, H. Liao and M. Debliquy, *Ceram. Int.*, 2017, **43**, 5990–5998.

399 X. Geng, C. Zhang, Y. Luo and M. Debliquy, *Appl. Surf. Sci.*, 2017, **401**, 248–255.

400 T. Wang, Q. Yu, S. Zhang, X. Kou, P. Sun and G. Lu, *Nanoscale*, 2018, **10**, 4841–4851.

401 K. Zhang, M. Peng, W. Wu, J. Guo, G. Gao, Y. Liu, J. Kou, R. Wen, Y. Lei, A. Yu, Y. Zhang, J. Zhai and Z. L. Wang, *Mater. Horiz.*, 2017, **4**, 274–280.

402 W. L. Ong, C. Zhang and G. W. Ho, *Nanoscale*, 2011, **3**, 4206–4214.

403 R. Li, K. Jiang, S. Chen, Z. Lou, T. Huang, D. Chen and G. Shen, *RSC Adv.*, 2017, **7**, 52503–52509.

404 T. M. Perfecto, C. A. Zito, T. Mazon and D. P. Volanti, *J. Mater. Chem. C*, 2018, **6**, 2822–2829.

405 X. Geng, C. Zhang, Y. Luo and M. Debliquy, *J. Taiwan Inst. Chem. Eng.*, 2017, **75**, 280–286.

406 C. Hua, Y. Shang, Y. Wang, J. Xu, Y. Zhang, X. Li and A. Cao, *Appl. Surf. Sci.*, 2017, **405**, 405–411.

407 S. Knobelspies, B. Bierer, A. Daus, A. Takabayashi, G. A. Salvatore, G. Cantarella, A. Ortiz Perez, J. Wollenstein, S. Palzer and G. Troster, *Sensors*, 2018, **18**, 358.

408 S. J. Choi, H. J. Choi, W. T. Koo, D. Huh, H. Lee and I. D. Kim, *ACS Appl. Mater. Interfaces*, 2017, **9**, 40593–40603.

409 S. M. Mohammad, Z. Hassan, R. A. Talib, N. M. Ahmed, M. A. Al-Azawi, N. M. Abd-Alghafour, C. W. Chin and N. H. Al-Hardan, *J. Mater. Sci.: Mater. Electron.*, 2016, **27**, 9461–9469.

410 S. Li, P. Lin, L. Zhao, C. Wang, D. Liu, F. Liu, P. Sun, X. Liang, F. Liu, X. Yan, Y. Gao and G. Lu, *Sens. Actuators, B*, 2018, **259**, 505–513.

411 D. K. Subbiah, G. K. Mani, K. J. Babu, A. Das and J. B. B. Rayappan, *J. Clean. Prod.*, 2018, **194**, 372–382.

412 S. Li, Y. Diao, Z. Yang, J. He, J. Wang, C. Liu, F. Liu, H. Lu, X. Yan, P. Sun and G. Lu, *Sens. Actuators, B*, 2018, **276**, 526–533.

413 H.-Y. Li, C.-S. Lee, D. H. Kim and J.-H. Lee, *ACS Appl. Mater. Interfaces*, 2018, **10**, 27858–27867.

414 D. K. Bandgar, S. T. Navale, Y. H. Navale, S. M. Ingole, F. J. Stadler, N. Ramgir, D. K. Aswal, S. K. Gupta, R. S. Mane and V. B. Patil, *Mater. Chem. Phys.*, 2017, **189**, 191–197.

415 C. Liu, H. Tai, P. Zhang, Z. Yuan, X. Du, G. Xie and Y. Jiang, *Sens. Actuators, B*, 2018, **261**, 587–597.

416 U. Yaqoob, D.-T. Phan, A. S. M. I. Uddin and G.-S. Chung, *Sens. Actuators, B*, 2015, **221**, 760–768.

417 U. Yaqoob, A. S. M. I. Uddin and G.-S. Chung, *Sens. Actuators, B*, 2016, **224**, 738–746.

418 K. K. Sadasivuni, D. Ponnamma, H.-U. Ko, H. C. Kim, L. Zhai and J. Kim, *Sens. Actuators, B*, 2016, **233**, 633–638.

419 V. Annapureddy, Y. Kim, G.-T. Hwang, H. W. Jang, S.-D. Kim, J.-J. Choi, B. Cho and J. Ryu, *Adv. Mater. Interfaces*, 2018, **5**, 1700811.

420 A. S. M. I. Uddin and G.-S. Chung, *J. Electroceram.*, 2018, **40**, 42–49.

421 X. Luo, K. You, Y. Hu, S. Yang, X. Pan, Z. Wang, W. Chen and H. Gu, *Int. J. Hydrogen Energy*, 2017, **42**, 8399–8405.

422 Z. Pang, Z. Yang, Y. Chen, J. Zhang, Q. Wang, F. Huang and Q. Wei, *Colloid. Surface. A*, 2016, **494**, 248–255.

423 A. Bagal, E. C. Dandley, J. Zhao, X. A. Zhang, C. J. Oldham, G. N. Parsons and C.-H. Chang, *Mater. Horiz.*, 2015, **2**, 486–494.

424 A. Sanaeifar, H. ZakiDizaji, A. Jafari and M. d. l. Guardia, *Trac-Trend. Anal. Chem.*, 2017, **97**, 257–271.

425 Y. Zhang, J. Zhao, T. Du, Z. Zhu, J. Zhang and Q. Liu, *Sci. Rep.*, 2017, **7**, 1960.

426 A. B. Far, F. Flitti, B. Guo and A. Bermak, *IEEE Sens. J.*, 2009, **9**, 713–722.

427 F. Flitti, A. Far, B. Guo and A. Bermak, *J. Sensors*, 2008, **2008**, 1–6.